

Crystal Structures and Thermoelectric  
Properties of Type-I Clathrate  $\text{Ba}_8\text{Al}_{16-x}\text{Ga}_x\text{Ge}_{30}$

Widya Rika Puspita

Doctor of Philosophy

Department of Materials Structure Science  
School of High Energy Accelerator Science  
SOKENDAI (The Graduate University for  
Advanced Studies)

**THESIS**

**Crystal Structures and Thermoelectric  
Properties of Type-I Clathrate  $\text{Ba}_8\text{Al}_{16-x}\text{Ga}_x\text{Ge}_{30}$**



Widya Rika Puspita

**DOCTOR OF PHILOSOPHY**

Department of Materials Structure Science

School of High Energy Accelerator Science

SOKENDAI (The Graduate University for Advanced Studies)

2018



Supervisor

Prof. Takashi Kamiyama

Reviewer

Prof. Toshiya Otomo

Prof. Shinichi Itoh

Assc. Prof. Masao Yonemura

Assc. Prof. Kazutaka Ikeda

Dr. Hiroyuki Takeya

Dr. Yoshihisa Ishikawa

Day of Submission

7<sup>th</sup> of June 2018



## Abstract

The demand for energy across the world is continuing to grow. This issue is driving the urgency for improving the energy efficiency. Thermoelectric materials which can directly convert waste heat into electricity have been considered as an effective solution. The performance of thermoelectric materials is characterized in the term of dimensionless figure of merit  $ZT$ , defined as  $ZT = S^2\sigma/\kappa$ , where  $\kappa$ ,  $\sigma$ ,  $S$ , and  $T$  represent thermal conductivity, electrical conductivity, Seebeck coefficient, and temperature, respectively. Based on the definition, a good performance of thermoelectric materials can be achieved by increasing the electrical properties while the thermal properties should be suppressed.

Clathrates have gained much attention as the potential candidate for thermoelectric materials due to their unique structure and properties. Type I clathrates (space group:  $Pm\bar{3}n$ ) with general formula  $G_8A_yB_{46-y}$  ( $G = \text{Ba, Sr, Eu}$ ;  $A = \text{Al, Ga, In}$ ;  $B = \text{Si, Ge, Sn}$ ) are the cage-type structure materials where the A and B play roles as host atoms forming two different types of cages, oversized tetrakaidecahedron and small dodecahedron cages, which enclosed the G guest metal atom.

The clathrates investigations have been mainly focused on the guest atom which provides a route to control the thermal conductivity for the purpose of enhancing the thermoelectric performance. Another approach to improve the thermoelectric performance is “cross-substitution” of the host atoms, which aims at tuning the electrical properties. However, the study of  $\text{Ba}_8\text{Al}_{16}\text{Ge}_{30}$  reported that a small change in the host structure also affect the thermal conductivity. By host substitution, controlling both electronic and thermal properties are possible.

The objectives of this study are to investigate the effect of Al substitution by Ga to the Ba guest atom feature and the effect to the thermoelectric properties in type I clathrate  $\text{Ba}_8\text{Al}_{16-x}\text{Ga}_x\text{Ge}_{30}$ .

# Contents

<b>Introduction.....</b>	<b>1</b>
<b>1.1 Thermoelectric .....</b>	<b>1</b>
1.1.1 Thermoelectric Phenomena.....	1
1.1.2 Thermoelectric efficiency .....	5
1.1.3 State-of-the-art Thermoelectric Materials .....	10
<b>1.2 Clathrates.....</b>	<b>11</b>
1.2.1 Phonon Glass Electron Crystal (PGEC).....	11
1.2.2 Crystal Structure of Type-I Clathrate .....	11
1.2.3 Zintl Concept.....	13
1.2.4 Rattling Guest Atom .....	14
1.2.5 Thermoelectric Properties of Clathrates .....	16
<b>1.3 Research Aim and Objectives .....</b>	<b>18</b>
1.3.1 Aim .....	18
1.3.2 Objectives.....	18
<b>Experimental Methods .....</b>	<b>19</b>
<b>2.1 Sample Synthesis.....</b>	<b>19</b>
2.1.1 Arc Melting Furnace .....	19
2.1.2 Spark Plasma Sintering .....	21
<b>2.2 X-ray Diffraction.....</b>	<b>23</b>
<b>2.3 Impurity Checking by XRD .....</b>	<b>25</b>
<b>Structural Analysis of <math>Ba_8Al_{16-x}Ga_xGe_{30}</math> .....</b>	<b>27</b>
<b>3.1 Neutron Powder Diffraction .....</b>	<b>27</b>
<b>3.2 Results and Discussion.....</b>	<b>30</b>
3.2.1 Results of $Ba_8Al_{16}Ge_{30}$ ( $Ga = 0$ ).....	30
3.2.2 Results of $Ba_8Al_{14}Ga_2Ge_{30}$ ( $Ga = 2$ ).....	33
3.2.3 Results of $Ba_8Al_{12}Ga_4Ge_{30}$ ( $Ga = 4$ ).....	36
3.2.4 Results of $Ba_8Al_{10}Ga_6Ge_{30}$ ( $Ga = 6$ ).....	39
3.2.5 Results of $Ba_8Al_8Ga_8Ge_{30}$ ( $Ga = 8$ ).....	41
3.2.6 Discussion .....	44
<b>Maximum Entropy Method .....</b>	<b>50</b>
<b>4.1 Maximum Entropy Method (MEM) .....</b>	<b>50</b>
<b>4.2 Results and Discussion.....</b>	<b>52</b>
4.2.1 Results of $Ba_8Al_{16}Ge_{30}$ ( $Ga = 0$ ).....	53
4.2.2 Results of $Ba_8Al_8Ga_8Ge_{30}$ ( $Ga = 8$ ).....	55
<b>Thermoelectric Properties.....</b>	<b>57</b>
<b>5.1 Seebeck Coefficient .....</b>	<b>57</b>

<b>5.2 Electrical Conductivity .....</b>	<b>58</b>
<b>5.3 Thermal Conductivity .....</b>	<b>59</b>
<b>5.4 Experimental Details of Transport Measurement.....</b>	<b>62</b>
5.4.1 Low-Temperature Measurement.....	62
5.4.2 High-Temperature Measurement .....	65
<b>5.5 Results and Discussion .....</b>	<b>70</b>
5.5.1 Low-Temperature .....	70
5.5.2 High-Temperature.....	73
<b>Conclusion .....</b>	<b>76</b>
<b>List of Figures .....</b>	<b>77</b>
<b>List of Tables.....</b>	<b>82</b>
<b>Bibliography.....</b>	<b>83</b>
<b>Acknowledgement.....</b>	<b>94</b>



# Chapter 1

## Introduction

### 1.1 Thermoelectric

#### 1.1.1 Thermoelectric Phenomena

In 1821 Thomas Johann Seebeck discovered a phenomenon in which a compass needle was deflected when subjected to different temperatures in a closed circuit formed of two different metal [1]. The deflected needle was caused by the electric current flowing around the closed circuit (see Figure 1.1(a)). The temperature difference drives the mobility of charge carriers, which migrate from the higher temperature side to the lower one. Thus, the Seebeck effect describes the conversion of heat into electricity [2].

The Seebeck effect can be demonstrated with an open circuit by connecting two different metal wires, known as thermocouple, and the other ends of the wires are connected to the voltmeter or galvanometer (Figure 1.1(b)). If heat is applied at the junction between the two different metals, electrons are enabled to pass from the material with the lower electron energy into that with higher electron energy. A small voltage which is also called as thermoelectric electromotive force (*emf*) is produced at the ends of thermocouple [3].

The magnitude of this effect can be expressed in terms of the Seebeck voltage  $V$  which found to be proportional to the temperature difference [4]

$$\Delta V_s = S_{AB} \Delta T \quad (1.1)$$

where the Seebeck coefficient  $S_{AB}$  is defined as the temperature dependent property of between the metals A and B and it is expressed in V/K or more often in  $\mu\text{V/K}$  units.

The sign of  $S_{AB}$  is positive if the electrical current is induced to flow in a clockwise direction from A to B.

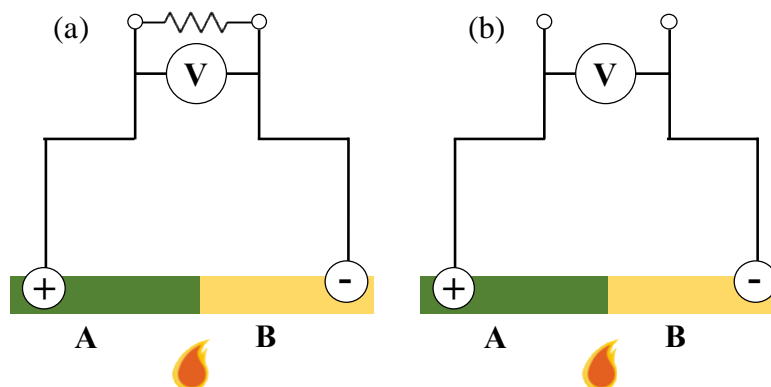


Figure 1. 1 Schematic of Seebeck effect in (a) close circuit and (b) open circuit made of two different metal A and B.

The reverse phenomenon of the Seebeck effect was later reported by Jean Peltier in 1834 [5], called Peltier effect. Peltier observed that when the current flows across the junction, heat will be absorbed at one junction and released to the environment at another junction (Figure 1.2). As a result, the junction which absorbs the heat will be cooled off and the other will be heated up. In 1838, Friedrich Emil Lenz demonstrated the nature of this effect by placing a drop of water on the junction of bismuth and antimony wires [6]. A freezing water was observed when electrical current passed and melting the ice by reversing the current flow direction. Thus, the Peltier effect describes the conversion of electricity into heat transfer.

The Peltier heat  $\Delta Q_P$  is proportional to the magnitude ( $I$ ) and duration ( $\Delta t$ ) of current applied [4],

$$\Delta Q_P = \Pi_{AB}(T)I\Delta t \quad (1.2)$$

where the Peltier coefficient  $\Pi_{AB}$  is the ratio of  $I$  to  $\Delta Q_P$  and it is expressed in V units or usually in mV. The sign is positive if the electrical current induces a cooling effect at hot junction when flowing from A to B.

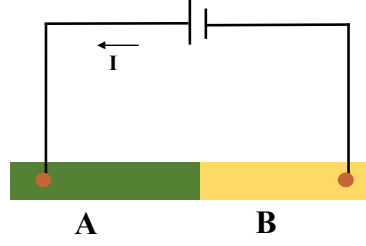


Figure 1. 2 Schematic of Peltier effect in a close circuit made of two different metal A and B.

Two decades later, William Thomson (who later become Lord Kelvin) established the relationship between Seebeck and Peltier coefficient using the theory of thermodynamics, assuming it to be a reversible system [7]. This reversible system is also known as Thomson effect. When current  $I$  passes through a homogeneous conductor in a temperature gradient during a time  $\Delta t$ , the reversible change of heat  $\Delta Q_T$  exists, given by the expression [2]

$$\Delta Q_T = I\Delta t \int_{T_C}^{T_H} \tau(T) dT \quad (1.3)$$

where  $\tau(T)$  is the Thomson coefficient and it is expressed in V/K units.  $T_H$  and  $T_C$  are the temperature at the hot side and the cold side, respectively. The sign of the Thomson coefficient is positive if the system absorbs heat when the current flows to the higher temperature region.

Based on the first law of thermodynamic, the electrical energy is equal to the thermal energy passing through the circuit, expressed by [2]

$$q\Delta V_s = \Delta Q = \Delta Q_P^{T_H} + \Delta Q_P^{T_C} + \Delta Q_P^A + \Delta Q_P^B \quad (1.4)$$

with  $q = I\Delta t$ . By expressing Eq (1.1) in the differential form  $dV_s = S_{AB}\Delta T$ , and using the Eqs. (1.2) and (1.3)

$$\int_{T_C}^{T_H} S_{AB}(T) dT = \Pi_{AB}(T_H) + \Pi_{BA}(T_C) + \int_{T_C}^{T_H} \tau_A(T)dT - \int_{T_C}^{T_H} \tau_B(T)dT$$

$$\int_{T_C}^{T_H} S_{AB}(T) dT = \Delta\Pi_{AB}(T_H) + \int_{T_C}^{T_H} [\tau_A(T) - \tau_B(T)]dT \quad (1.5)$$

where  $\Pi_{BA}(T_C) = -\Pi_{AB}(T_C)$ . By assuming the metals are short enough, the equation above re-expressed as

$$S_{AB}(T)dT = d\Pi_{AB}(T_H) + [\tau_A(T) - \tau_B(T)]dT \quad (1.6)$$

From the second law of thermodynamics which state that the entropy change vanishes in reversible process, the equation is given by

$$\int \frac{\Delta Q}{T} = \frac{\Pi_{AB}(T_H)}{T_H} - \frac{\Pi_{AB}(T_C)}{T_C} + \int_{T_C}^{T_H} \frac{\tau_A(T) - \tau_B(T)}{T} dT \equiv 0 \quad (1.7)$$

The Eq. (1.7) can be expressed in the differential form

$$d\left(\frac{\Pi_{AB}}{T}\right) + \frac{\tau_A - \tau_B}{T} dT = 0 \quad (1.8)$$

Using the Eqs. (1.6) and (1.8) to obtain

$$\Pi_{AB} = S_{AB}T \quad (1.9)$$

this equation describes that the Peltier and Seebeck coefficient are proportional to each other and have the same sign. Then, by differentiating and relating the above equation to the Eq. (1.6), one gets

$$\tau_B - \tau_A = T \frac{dS_{AB}}{dT} \quad (1.10)$$

thus, the equation shows that the Thomson effect is generated by the induced Seebeck coefficient with the presence of temperature gradient. The Eqs. (1.9) and (1.10) are the so-called the first and second *Kelvin relation*, respectively.

### 1.1.2 Thermoelectric efficiency

The thermoelectric effect can be applied to build a thermoelectric generator (TEG) and thermoelectric cooler (TEC) device based on the Seebeck and Peltier effect, respectively. There are many advantages offered by the thermoelectric devices compared to other energy technologies. Those are the relatively small in weight and size, the absence of moving parts and electrical noise during operation, environmentally friendly, high reliability, precise temperature control, and the ability to be applied in zero gravity environment. However, this technology has low conversion efficiency rate and high cost.

Generally, the thermoelectric devices consist of a large number of thermocouples in which each thermocouple consists of a positive (p) and negative (n) leg (thermoelement). Each thermocouple is connected to a conductor that is assumed to have zero electrical and thermal resistance. The length of p-type leg  $L_p$  and n-type leg  $L_n$  and the cross-section area of  $A_p$  and  $A_n$  are different from each other. The schematic of thermoelectric devices, TEG and TEC, is depicted in the figure below.

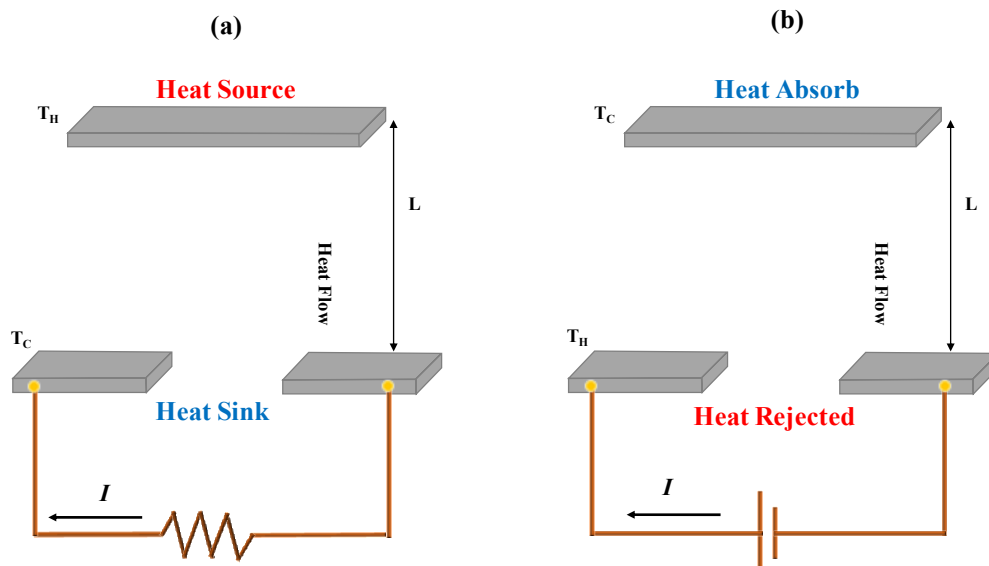


Figure 1. 3 Schematic of (a) thermoelectric generator (TEG) and (b) thermoelectric cooler (TEC).

The thermoelectric efficiency was firstly investigated by Edmund Altenkirch in the early 1900s [8, 9]. Altenkirch introduced the term of *figure of merit*  $ZT$  in order to characterize the desirable properties of thermoelectric materials. The good thermoelectric materials should possess high Seebeck coefficient ( $S$ ) to maximize the

conversion of heat into electricity or vice versa, high electrical conductivity ( $\sigma$ ) to minimize Joule heating, low thermal conductivity ( $\kappa$ ) to retain heat at the junction, and can be written as

$$ZT = \frac{S^2\sigma}{\kappa} = \frac{S^2\sigma}{\kappa_e + \kappa_l} \quad (1.11)$$

where  $T$  is the absolute temperature,  $\sigma$  is equal to the inverse of electrical resistivity ( $\rho$ ), and  $ZT$  is a dimensionless parameter. Thermal conductivity is total contribution of charge carriers (electronic thermal conductivity,  $\kappa_e$ ) and phonons (lattice thermal conductivity,  $\kappa_l$ ).

In 1949, Ioffe developed a comprehensive theory of thermoelectric efficiency [6]. Consider the TEG illustrated in Figure 1.3a. The efficiency of the TEG is given by

$$\eta = \frac{W}{\dot{Q}_H} \quad (1.12)$$

where  $W$  is the energy supplied to the external load and  $\dot{Q}_H$  is the heat energy absorbed from heat source at the junction. The  $W$  is given by the subtracting result of electrical power from Seebeck effect lost by Joule heating because of the internal resistance and written as [2]

$$W = I\Delta V_s - I^2r \quad (1.13)$$

with the internal resistance  $r = \frac{\rho_n L_n}{A_n} + \frac{\rho_p L_p}{A_p}$  and  $I = \frac{\Delta V_s}{r+R}$ . By substituting the  $I$  to the Eq. (1.13), one obtains

$$W = \frac{R(\Delta V_s)^2}{(r+R)^2} \quad (1.14)$$

The  $\dot{Q}_H$  is given by the total of heat energy absorbed at the hot junction by the p- and n-type legs, which is a contribution from Peltier heat flow  $(S_p - S_n) TI$  and heat conduction to the sink  $\kappa_p A_p \left(\frac{dT}{dx}\right)_{L_p}$  and  $\kappa_n A_n \left(\frac{dT}{dx}\right)_{L_n}$ , where  $\kappa$  is the thermal conductivity and  $\left(\frac{dT}{dx}\right)$  is temperature gradient. Thus, the  $\dot{Q}_H$  is expressed as follow

$$\dot{Q}_H = \kappa_p A_p \left( \frac{dT}{dx} \right)_{L_p} + \kappa_n A_n \left( \frac{dT}{dx} \right)_{L_n} + (S_p - S_n) T I \quad (1.15)$$

The heat generation rate along each leg in the contribution of joule heating is

$$-\kappa_p A_p \frac{d^2 T}{dx^2} = \frac{I^2 \rho_p}{A_p} \quad (1.16)$$

$$-\kappa_n A_n \frac{d^2 T}{dx^2} = \frac{I^2 \rho_n}{A_n} \quad (1.17)$$

where  $\rho$  is the electrical resistivity. With  $x = 0$  at the heat sink ( $T_C$ ) and  $x = L_n$  or  $L_p$  at the heat source ( $T_H$ ), the Eqs. (1.16) and (1.17) can be solved to find

$$\kappa_p A_p \frac{d^2 T}{dx^2} = -\frac{I^2 \rho_p (x - L_p/2)}{A_p} + \frac{\kappa_p A_p (T_H - T_C)}{L_p} \quad (1.18)$$

$$\kappa_n A_n \frac{d^2 T}{dx^2} = -\frac{I^2 \rho_n (x - L_n/2)}{A_n} + \frac{\kappa_n A_n (T_H - T_C)}{L_n} \quad (1.19)$$

Making use of Eqs. (1.18), (1.19) and (1.15) to obtain the heat flow rate at  $x = 0$ .

$$\begin{aligned} \dot{Q}_H = & \left( -\frac{I^2 \rho_p L_p}{2A_p} + \frac{\kappa_p A_p (T_H - T_C)}{L_p} \right) + \left( -\frac{I^2 \rho_n L_n}{2A_n} + \frac{\kappa_n A_n (T_H - T_C)}{L_n} \right) \\ & + (S_p - S_n) T_H I \end{aligned} \quad (1.20)$$

The equation above can be simplified to

$$\dot{Q}_H = (S_p - S_n) T_H I + K(T_H - T_C) - \frac{I^2 r}{2} \quad (1.21)$$

where the internal thermal conductance  $K = \frac{\kappa_p A_p}{L_p} + \frac{\kappa_n A_n}{L_n}$ . The equation above shows

that half of Joule heating  $\left( \frac{I^2 r}{2} \right)$  passes to the sink and the other half to the source.

Combining the Eqs. (1.13) and (1.21) to obtain

$$\eta = \frac{W}{\dot{Q}_H} = \frac{I\Delta V_s - I^2 r}{I \frac{\Delta V_s}{\Delta T} T_H + K\Delta T - \frac{I^2 r}{2}} \quad (1.22)$$

The Eq. (1.22) can be rewritten as follow

$$\eta = \left(\frac{\Delta T}{T_H}\right) \frac{m}{1 + m + \frac{(1+m)^2}{ZT_H} - \frac{\Delta T}{2T_H}} \quad (1.23)$$

where  $m = R/r$  is the ratio between the external and internal resistance and the figure of merit  $Z$  is expressed in the form

$$Z = \frac{(S_p - S_n)^2}{Kr} \quad (1.24)$$

The value of  $Kr$  should be minimized for the optimization of  $Z$ , which occurs when

$$\frac{L_n A_p}{L_p A_n} = \sqrt{\frac{\rho_p \kappa_n}{\rho_n \kappa_p}} \quad (1.25)$$

Thus, the figure of merit  $Z$  becomes

$$Z = \frac{(S_p - S_n)^2}{(\sqrt{\rho_n \kappa_n} + \sqrt{\rho_p \kappa_p})^2} \quad (1.26)$$

In practice, the figure of merit is investigated separately for each leg. Therefore, the Eq. (1.26) reduces to

$$Z = \frac{S^2 \sigma}{\kappa} \quad (1.27)$$

where  $S^2 \sigma$  is referred to as the power factor and it is expressed in  $\text{W/m.K}^2$  or more often in  $\mu\text{W/cm.K}^2$  units.

The efficiency reaches its maximum value when the ratio between the external resistance and internal resistance is given by [3]

$$m = \frac{R}{r} = (\sqrt{1 + ZT_H}) \quad (1.28)$$

Thus, the maximum efficiency of TEG from the Eq. (1.23) is expressed as follow [10]

$$\eta_{max} = \frac{(\Delta T)(\sqrt{1 + ZT_H} - 1)}{T_H(\sqrt{1 + ZT_H}) + T_C} \quad (1.29)$$

In Figure 1. 4, the maximum efficiency is plotted against the heat source temperature for various  $ZT$  values with  $T_C = 300$  K. When the  $ZT = 1$  with  $T_H = 400$  K ( $\Delta T = 100$  K), the maximum efficiency is only 5%. To increase the maximum efficiency percentage,  $ZT$  or the temperature gradient should be increased. In order to compete with that of traditional power generators which can reach 40% of the Carnot efficiency, a  $ZT$  value above 3 would be necessary [11, 12].

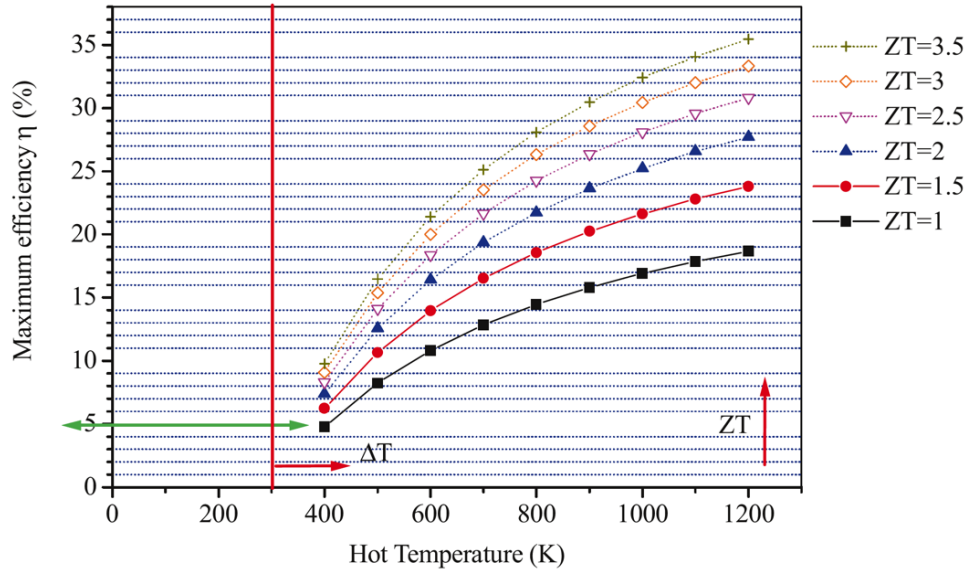


Figure 1. 4 Maximum efficiency for TEG [10].

### 1.1.3 State-of-the-art Thermoelectric Materials

Figure 1.5 shows the  $ZT$  values of state-of-the-art thermoelectric materials against the applied temperature for the n-type. The most used material for room temperature (300-500 K) application are  $\text{Bi}_2\text{Te}_3$ -based alloys which were first discovered in the 1954 [13]. Up to now, this  $\text{Bi}_2\text{Te}_3$  family has remained as the best commercial with reported  $ZT$  of 1.2 at 357 K [14]. For medium-temperature (500-900 K), the most known material is from PbTe family which have been studied since 1961 [15]. Alloying of PbTe with  $\text{AgSbTe}_2$  (LAST) have led to improve  $ZT$  up to 2.2 at 800 K [16]. Some new families for medium-temperature application have been identified in recent years, including skutterudites [17], clathrates [18], and  $\text{Mg}_2(\text{Si}, \text{Sn}, \text{Ge})$  [19, 20]. For high-temperature (>900 K), SiGe alloys are the typically used [21].  $\text{La}_3\text{Te}_4$  [22] and ZrNiSn-based Half-Heusler (HH) alloys [23] also have been reported to have  $ZT > 1$  at high temperature.

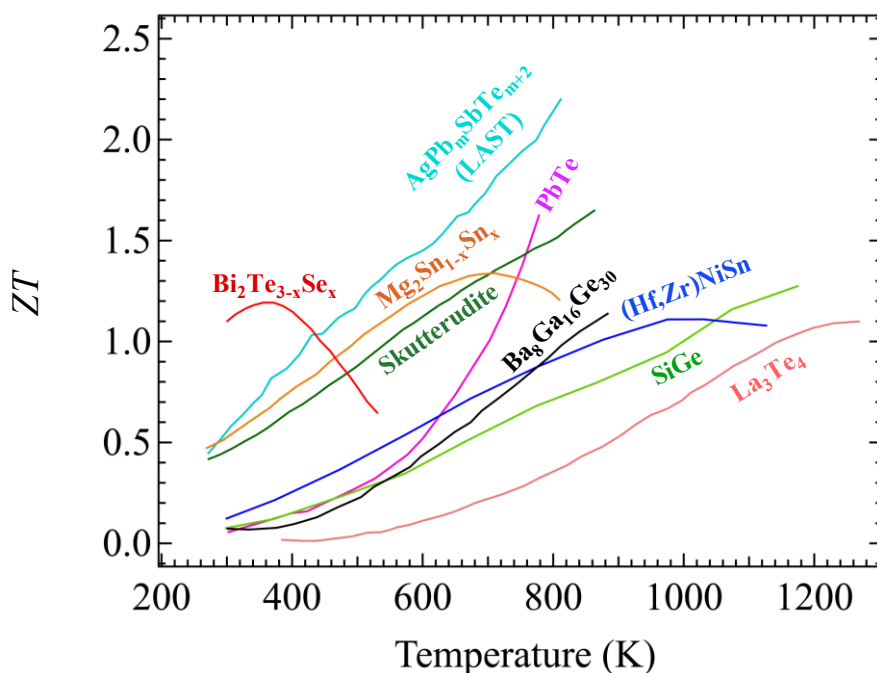


Figure 1. 5 Summary of best  $ZT$  values for some typical classes of n-type thermoelectric materials as a function of temperature [13-23].

## 1.2 Clathrates

### 1.2.1 Phonon Glass Electron Crystal (PGEC)

Clathrates have been studied for more than 200 years since the hydrate clathrate was revealed [24]. Later, thermoelectric properties of Si and Ge based clathrates was reported by Cros *et al.* in 1970 [25]. Clathrates started to attract much attention as the potential candidate for thermoelectric materials since the concept of phonon glass-electron crystal (PGEC) introduced by Slack [26] in 1995. Based on the PGEC concept, the ideal thermoelectric materials would behave as glass-like materials (low thermal conductivity) and at the same time also behave as crystalline materials (high resistivity and electrical conductivity). Slack proposed that the PGEC materials could be obtained from the cage-type structure materials, which is caused by the rattling of the trapped atom at the center of the cage. Clathrates, crystalline materials possessing guest-host structure, exhibit a low thermal conductivity, thus makes clathrates fulfill the requirements of PGEC concept [27].

The majority of studies have concerned on the type-I clathrate of Si- [28, 29], Ge- [30-32], and Sn- [33] based because of the favorable electronic and thermal properties: The most studied material is  $\text{Ba}_8\text{Ga}_{16}\text{Ge}_{30}$  [18, 27, 30, 34-36]. This compound has been reported as the highest thermoelectric figure of merit for non-doped clathrate with  $ZT \approx 1.35$  at 900 K [18].

### 1.2.2 Crystal Structure of Type-I Clathrate

Type-I clathrate has cubic structure belonging to space group  $Pm\bar{3}n$  with general formula  $\text{G}_8\text{A}_y\text{B}_{46-y}$  ( $\text{G} = \text{Ba}, \text{Sr}, \text{Eu}$ ;  $\text{A} = \text{Al}, \text{Ga}, \text{In}, \text{Transition Metal}$ ;  $\text{B} = \text{Si}, \text{Ge}, \text{Sn}$ ). The unit cell consists of two types of cages, six oversized tetrakaidecahedron and two small dodecahedron cages, formed by the A and B host atoms which enclose G guest metal atom, see Figure 1.6. The host atoms are located at three different Wyckoff sites:  $6c$ ,  $16i$ , and  $24k$ . The guest atoms are denoted as  $2a$  and  $6d$  for the dodecahedron and tetrakaidecahedron cages, respectively [37, 38]. The dodecahedron cage consists of 12 pentagon faces while tetrakaidekahedron have 2 more additional of hexagon faces.

The dodecahedron cage has five-fold symmetry, thus a combination with a less symmetrical polyhedron made up of hexagonal faces is one of the ways to form a periodic structure. The tetrakaidecahedra are connected to each other by sharing their hexagonal and pentagonal faces, while the dodecahedra are surrounded by tetrakaidecahedra, isolated from each other [39, 40].

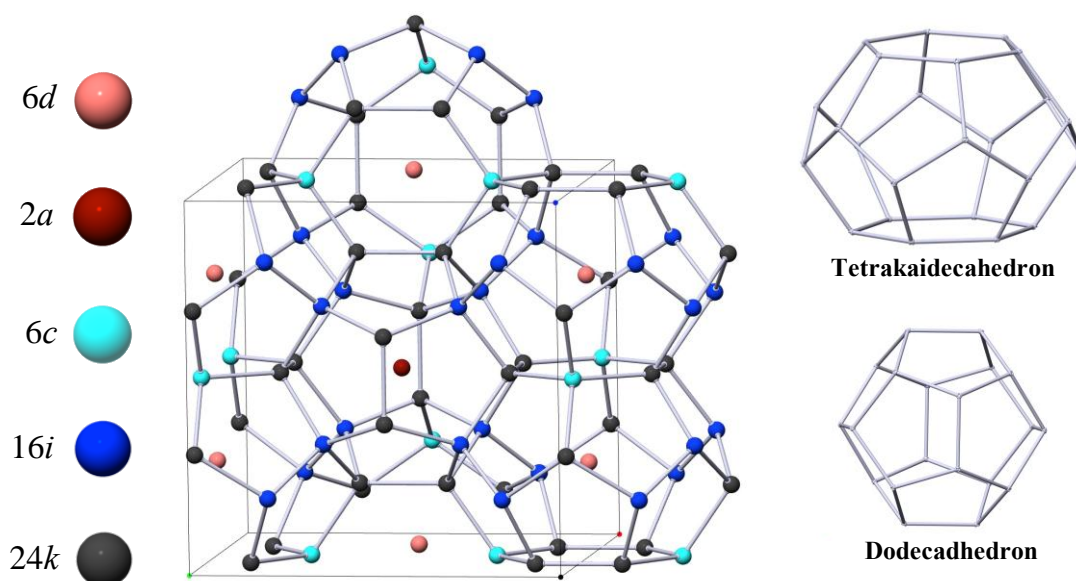


Figure 1.6 Crystal structure of the type-I clathrate. The guest atoms are shown as pink and dark red atoms at 6d (G2) and 2a (G1) position, respectively. The light blue, dark blue, and black atoms are the host structure atoms (A/B) at 6c, 16i, and 24k position, respectively.

The atom occupying 24k site is tetrahedrally coordinated by three atoms of 16i and one atom of 24k site (see Figure 1.7). The atom in the 16i site is tetrahedrally coordinated by two atoms of 24k, one atom of 16i, and one atom of 6c site. Whereas, the atom occupying the 6c site is tetrahedrally coordinated by four atoms of 24k site, isolated from others atom of 6c site [40].

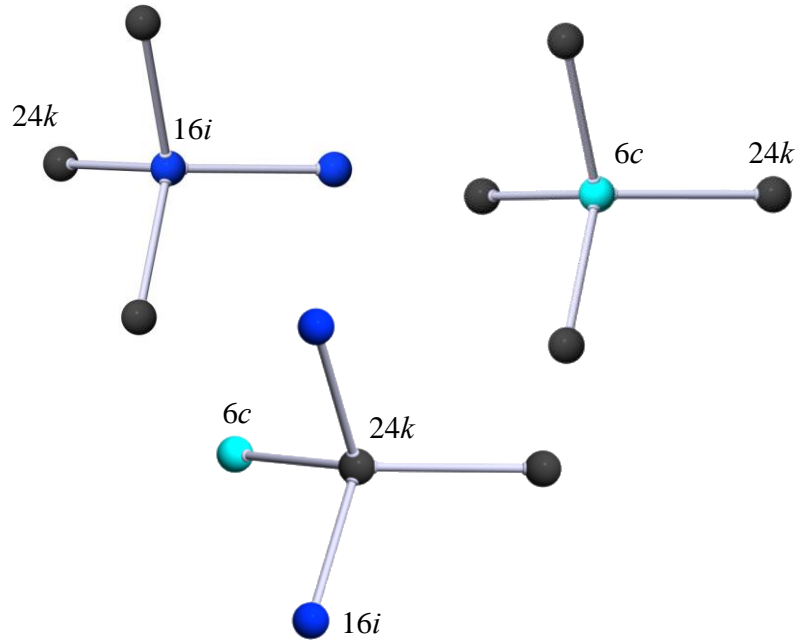


Figure 1. 7 Atomic Coordination in the type-I clathrate

### 1.2.3 Zintl Concept

The Zintl concept can be used to explain the bonding situation and stoichiometry of type-I clathrate. In the Zintl concept, it is assumed that both ionic and covalent bonding are present in the compound. The electropositive cations donate their electron to electronegative anions in order to complete the valence requirement (octet rule) [41, 42]. In the case of clathrates, guest atoms are assumed to be ionic and donate their electron to the host atoms and build a covalently bonded cage structure. Whereas, the guest atoms are weakly ionically bonded to the cage structure [43]. In general, the equation for clathrate with general formula  $G_8A_yB_{46-y}$  can be written as follows [37]

$$184e^- = 8G^{g^+} + yA^{a^+} + (46 - y)B^{b^+} \quad (1.30)$$

where  $G^{g^+}$ ,  $A^{a^+}$ , and  $B^{b^+}$  are the valence electrons number of G guest atom, A, and B host atoms, respectively. There are 46 atoms in the cage structure, thus 184 electrons are required to form tetrahedral bonds between all host atoms as each host atom is

four-coordinated. For compound  $\text{Ba}_8\text{Ga}_{16}\text{Ge}_{30}$ , each Ba donates 2 electrons to the host atoms, becoming  $\text{Ba}^{2+}$ . Since there are eight Ba atoms, the number of transferred electrons is 16. The Ga and Ge possess three and four valence electrons, respectively, giving 48 electrons from Ga and 120 electrons from Ge. For a total, 184 electrons are available.

### 1.2.4 Rattling Guest Atom

Rattling phenomena have been observed in several classes of cage compounds, such as skutterudite [44, 45],  $\text{Al}_{10}\text{V}$  [46], and clathrate [39, 30]. In general, rattling of guest atoms is an unusual vibrational behavior which caused by the oversized room available provided by the host cage. The oversized space drives the guest atoms to have weak restoration forces with the cage structure, thus reduces the phonon energies and leads the guest atom to vibrate in a localized mode [47]. The coupling of rattling with heat-carrying phonon increase the scattering probability causing to suppress the thermal conductivity [48, 49]. For type-I clathrate, this characteristic of guest atom was identified in the guest atom of tetrakaidekahedron cage, occupying the  $6d$  site, G(2) [27].

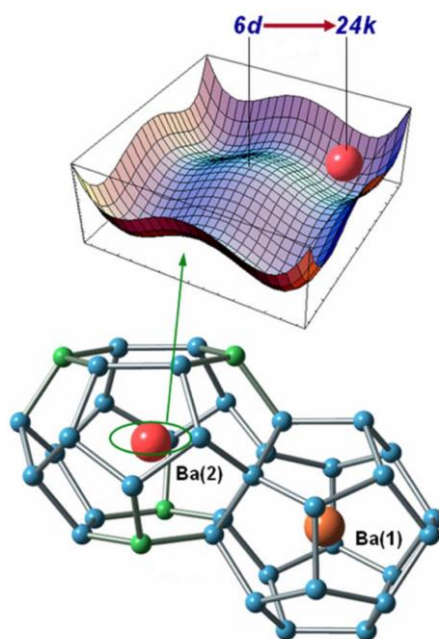


Figure 1. 8 Schematic illustration of the anharmonic potential for guest atom in tetrakaidecahedron cage, with 24k off-center position [54].

The weak restoration force of guest atoms leads to deform the single-well potential to multiple-well potential, the center is no longer position of the minimum energy potential. The multiple-well potential of guest atoms are schematically illustrated in Figure 1.8. The energy potential can be approached by simple model  $V = Ax^2 + Bx^4$ , where the first and second are harmonic and anharmonic term, respectively [54, 55].

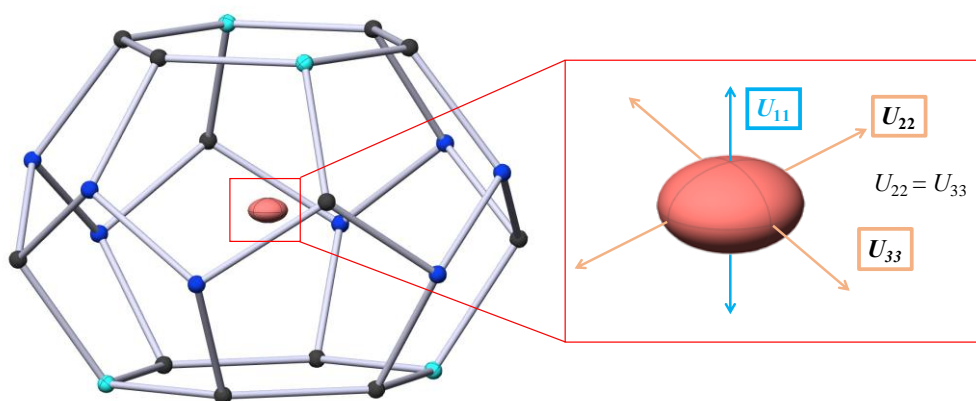


Figure 1. 9 Anisotropic condition for guest atom in tetrakaidecahedron cage.

In the structural analysis, the unusual vibration of guest atoms can be identified from the large atomic displacement parameters [50, 54, 56], so-called “disorder guest atom”. For example, the refinement result of Sr(2) atom in  $\text{Sr}_8\text{Ga}_{16}\text{Ge}_{30}$  show very large isotropic ADP at room temperature. For anisotropic condition, a large ADP of guest atom is shown in the direction parallel to the hexagonal faces (see Figure 1.9). In agreement to the different Fourier map showing the distribution of nuclear density in off-center position, a four-site disorder model was proposed to explain these features [56].

The disorder of Ba(2) guest atoms in n- and p-type  $\text{Ba}_8\text{Ga}_{16}\text{Ge}_{30}$  have revealed by x-ray and neutron diffraction studies. The Ba(2) atoms are positioned off-center, 24k or 24j sites (see Figure 1.8)[35]. The Ba(2) guest atoms in  $\text{Ba}_8\text{Ga}_{16}\text{Sn}_{30}$  also occupy off-center 24k site with displacement of 0.43 Å, see Figure [54]. In the study of

$\text{Ba}_8\text{Al}_{16}\text{Ge}_{30}$  the static disorders  $d_{0K}$  at 0 K were obtained with 0.101(3), 0.191(1), and 0.238(1) for sample grown by Czochralski, shake and bake, and flux, respectively [53]. The disorder feature of guest atoms is significantly affected by synthesis methods.

## 1.2.5 Thermoelectric Properties of Clathrates

Majority work on clathrates has focused on guest atom believed to be responsible for the low thermal conductivity which necessary to obtain high  $ZT$  thermoelectric materials [27, 30, 34]. The thermal conductivity can be reduced by lowering the lattice contribution  $\kappa_l$ . The summary of lattice thermal conductivity below 300 K is shown by Figure 1.10.  $\text{Sr}_8\text{Ga}_{16}\text{Ge}_{30}$  and  $\text{Eu}_8\text{Ga}_{16}\text{Ge}_{30}$  have lattice thermal conductivities which resemble the behavior of amorphous  $\text{SiO}_2$  [30, 48, 50-53], while others have the characteristic of defect-free crystalline materials which dominated by the Umklapp scattering (the linear decreasing  $1/T$  line).

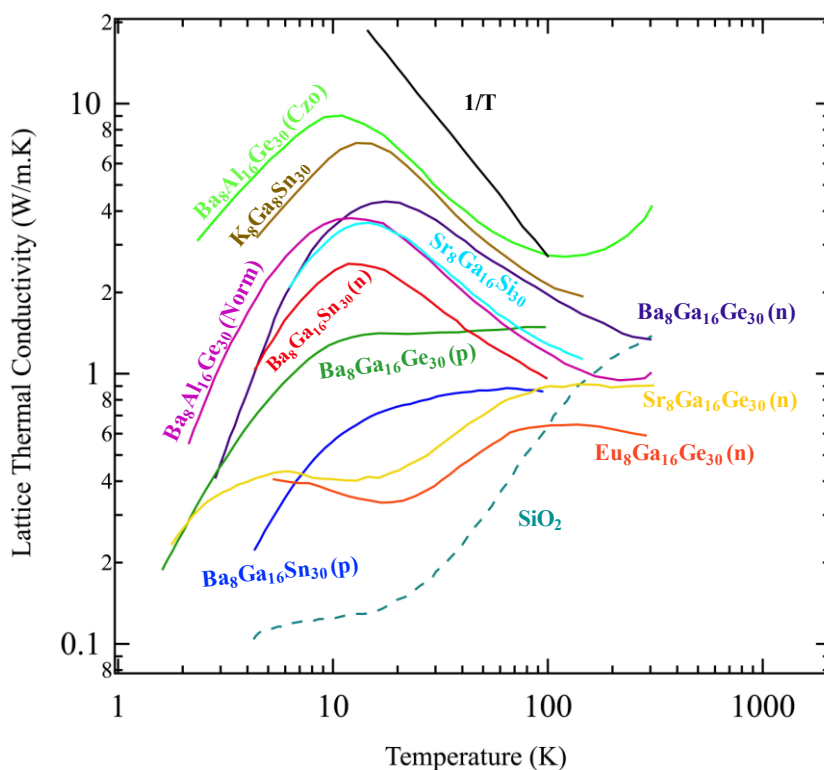


Figure 1. 10 Summary of lattice thermal conductivity data [30, 48, 50-53] below 300 K with  $n$  and  $p$  denote the  $n$ - and  $p$ -type of clathrates, respectively. While norm corresponds to the solid-state synthesis and Czo denotes the Czochralski synthesis method. The dash line is the data of  $\text{SiO}_2$  glass and the black

line indicates the inverse temperature dependence characteristic in which Umklapp scattering is dominant.

The glass-like lattice thermal conductivity has three characteristic temperature regions [57]: (1)  $\kappa_l(T) \propto T^{2-\delta}$  below 1 K, which generated by the interaction between tunneling states and excited acoustic phonons, (2)  $\kappa_l(T) = \text{constant}$ , in the range of 5 to 10 K, which originated from the flattening of acoustic phonon branches through the hybridization with guest atom phonon (3)  $\kappa_l(T)$  shows  $T$ -linear rise above the plateau region, which caused by hopping of the local modes assisted by acoustic phonons for carrying heat.

The electronic properties of clathrates are often discussed in terms of power factor,  $S^2\sigma$ . In order to enhance  $ZT$  values, it is necessary to maximize the power factor. The power factor depends on the charge carrier mobility, charge carrier concentration, and also the effective mass. The charge carrier concentration should be low in order to get large Seebeck coefficient, on the contrary, the low charge carrier leads to the low electrical conductivity. The high effective mass maximizes the Seebeck coefficient but affects to reduce the charge carrier mobility resulting in lowering the electrical conductivity. However, lowering electrical conductivity means reducing the electrical contribution of thermal transport properties  $\kappa_{el}$ , which is good to improve  $ZT$  [58, 59]. An optimum value of those properties must be found to achieve a large power factor.

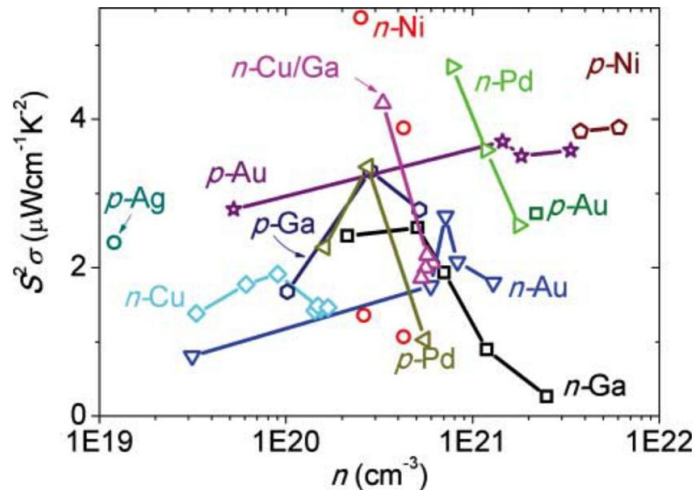


Figure 1. 11 Summary of power factor data as function of charge carrier concentration for several  $Ba_8TM_xA_yGe_{46-x-y}$  systems, where  $TM = \text{group 11 and 12 elements}$ ,  $A = \text{Al, Ga, In}$  [37].

For clathrate compounds, those features can be tuned by cross-substitution of cage elements [60]. Figure 1. 11 show the summary of thermopower as a function of charge carrier concentration for several  $\text{Ba}_8\text{TM}_x\text{A}_y\text{Ge}_{46-x-y}$  systems, where TM = group 11 and 12 elements., A = Al, Ga, In. The figure reveals the enhancement power factor for quaternary system  $\text{Ba}_8\text{Ga}_x\text{Pt}_y\text{Ge}_{46-x-y}$  [61] and ternary system  $\text{Ba}_8\text{Au}_x\text{Ge}_{46-x}$  [62] compared to  $\text{Ba}_8\text{Ga}_{16}\text{Ge}_{30}$  [35]. The mobility of  $\text{Ba}_8\text{Cu}_x\text{Ga}_y\text{Ge}_{46-x-y}$  is twice larger than the one of  $\text{Ba}_8\text{Cu}_x\text{Ge}_{46-x}$ , despite the fact that the  $\text{Ba}_8\text{Cu}_x\text{Ga}_y\text{Ge}_{46-x-y}$  system also has higher carrier concentration. In  $\text{Ba}_8\text{Al}_{16}\text{Ge}_{30}$  investigated by Christensen *et al.* [53], the subtle change in the host structure was found to affect the lattice thermal conductivity. Therefore, the cross-substitution brings the possibility to tune the electrical properties and thermal properties at once.

## 1.3 Research Aim and Objectives

### 1.3.1 Aim

To investigate the structure-properties relation on the thermoelectric clathrate  $\text{Ba}_8\text{Al}_{16-x}\text{Ga}_x\text{Ge}_{30}$  ( $x = 0, 2, 4, 6, \text{ and } 8$ ).

### 1.3.2 Objectives

The objectives of this study are: a) to analyze the effect of Ga substitution for Al to the Ba2 guest atom feature of  $\text{Ba}_8\text{Al}_{16-x}\text{Ga}_x\text{Ge}_{30}$  from the neutron powder diffraction data and MEM analysis; b) to clarify the effect of Ga substitution for Al to the thermoelectric properties in wide range temperature.

# Chapter 2

## Experimental Methods

### 2.1 Sample Synthesis

The high purity of Ba (99%), Al (99.99%), Ga (99.99%), and Ge (99.999%) metal was used to prepare the samples. The raw materials were cut using nipper under argon environment of glovebox to get the desired amount of sample. The cyclohexane was used to remove the oil from the barium surface because the barium was stored in oil. Before weighing the Ba, the surface of Ba should be removed. To protect from the reaction with air environment, the raw materials were placed into a single desiccator when bringing out of glovebox (Figure 2.2(b)).

#### 2.1.1 Arc Melting Furnace

The polycrystalline samples of  $\text{Ba}_8\text{Al}_{16-x}\text{Ga}_x\text{Ge}_{30}$  ( $x = 2, 4, 6, \text{ and } 8$ ) were prepared by melting the raw materials in arc melting furnace under argon environment. The electric arc is struck between the electrode connected to the copper stinger and the metallic charge [63]. The heat is transferred to metallic charge by conduction. The sample were placed in the cup of copper heart plate inside the furnace chamber (Figure 2.2(a)) and were melted four to five times accompanying by turning over the sample after each melt. The purpose of turning over the sample is to ensure the sample homogeneity. The applied current was slowly increased in the range of 60 to 150 A. The cooling system is located surrounding the sample chamber, under the copper hearth, roof of chamber, and stinger. Thus, the sample was quickly cooled and solidified to a button shape after melting as shown in Figure 2.2(c). Figure 2.1. shows the illustration of the art melting furnace. For x-ray and neutron diffraction, the ingots were ground

into a fine powder except for the high temperature measurement because it is prohibited to measure powder sample at high temperature at J-PARC Facility.

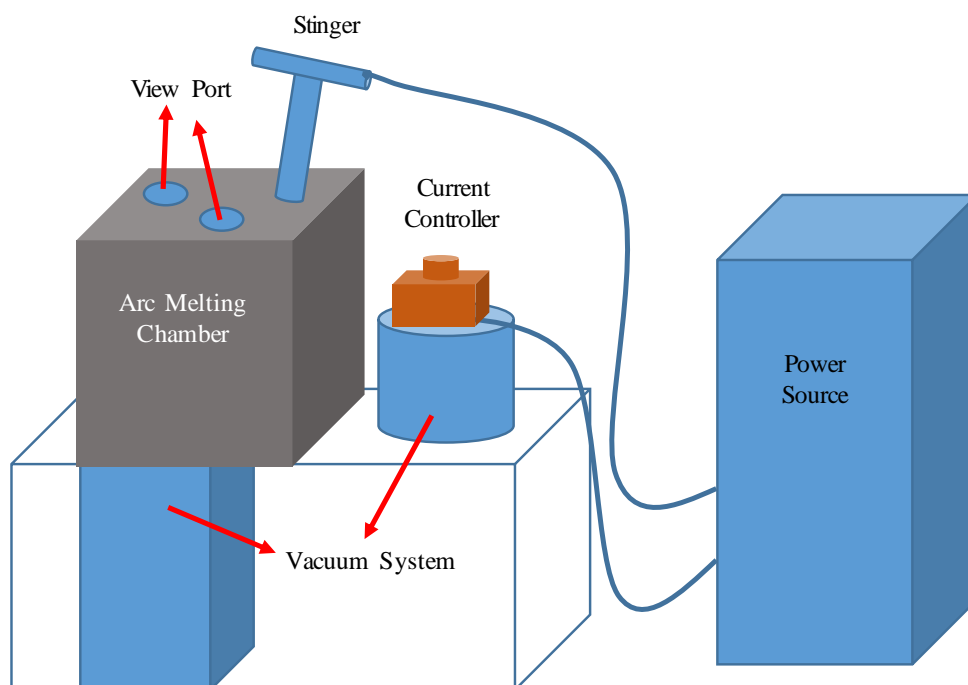


Figure 2. 1 The illustration of arc melting furnace.

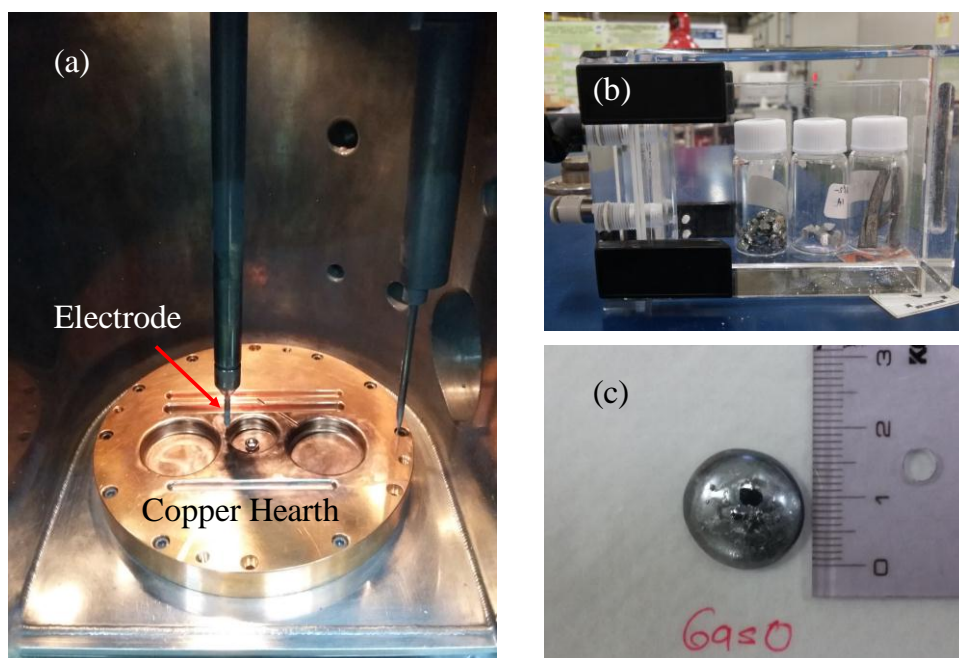


Figure 2. 2 (a) Inside the sample chamber which consists of copper hearth and electrode. (b) raw materials brought by the single desiccator. (c) The button shape of ingot as a result of arc melting process.

## 2.1.2 Spark Plasma Sintering

Spark Plasma Sintering (SPS) is a sintering method using the spark plasma created by a pulse direct current (DC) accompanied by applying a uniaxial mechanical pressure [65, 66]. The sintering itself is a heating treatment subjected to the compact powder material to become a compact solid piece by applying the heat below the melting point and pressure. The existence of plasma could not be detected so far. This method offers several advantages over conventional sintering method, including: (a) rapid sintering process because of large spark pulse current (up to 10 kA); (b) high thermal efficiency, as a result of the direct heating of graphite dies and no insulator or other heating element; (c) uniform heating condition, resulting a high-quality compact sintered powder without considerable grain growth [64, 66, 67].

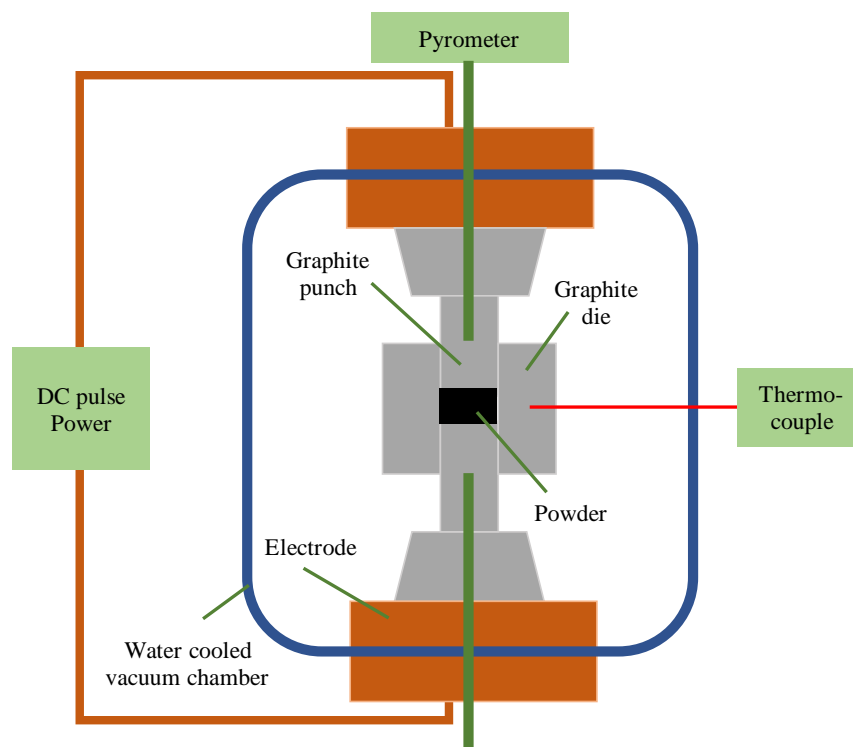
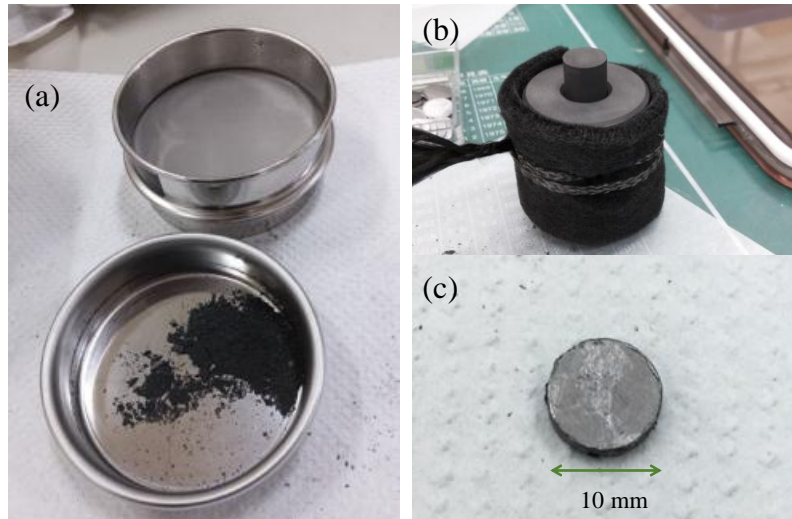


Figure 2. 3 Schematic diagram of SPS apparatus

The SPS were performed using a Sinterland, model Labox™ 110MC apparatus. The unit is capable of producing a DC up to 1200 A at a maximum voltage 12 V and a load up to 10 kN. A schematic diagram of the SPS apparatus is shown in Figure 2.3. Before doing the experiment, the melted ingots of arc melting were ground into a fine

powder and filtrated by dry-sieving with screen of 45  $\mu\text{m}$  (Figure 2.4(a)). The fine powder of  $\text{Ba}_8\text{Al}_{16-x}\text{Ga}_x\text{Ge}_{30}$  was loaded into the 10.4 mm in inner diameter of graphite die with the 10 mm in diameter of graphite punches. One piece and two pieces of thin graphite foil were placed surrounding the inner hole of die and in between the sample and punches, respectively. The purpose of placing graphite foils is to avoid the reaction between sample and die. Then, the graphite die was wrapped by graphite felt for the purpose of keeping the temperature homogeneity (Figure 2.4(b)). After applying a load of 5.5 kN (corresponding to pressure of the 70 MPa [68]), sample was heated to the temperature range of 800 – 900 K for 3 minutes at a heating rate approximately 100°C/min. The experiments were performed in argon atmosphere.



*Figure 2. 4 (a) Dry-sieving with screen of 45  $\mu\text{m}$ ; (b) The graphite die wrapping by graphite felt graphite felt to keep the temperature homogeneity; (c) The sintered sample covered by graphite foils.*

The high pulse DC passing through the graphite die and sample generate Joule heating which promotes densification. The spark appearing in the gap between particles of material contributes to the rapid heating [69]. After the sintering, the sample was allowed to cool. Then, the sintered sample covered by graphite foils (Figure 2. 4(c)) was removed by polishing machine.

## 2.2 X-ray Diffraction

Diffraction occurs when electromagnetic radiation is scattered by periodic array of objects, producing constructive interference at specific angles. The diffraction pattern can be observed only when the magnitude of radiation wavelength is in the same order as the repetitive distance between the scattering objects [70, 71]. The range of X-ray wavelength has the same range as the shortest interatomic distance of crystals, on the order of angstroms. Thus, the diffraction effect will be seen when the crystals are subjected to X-ray beam. Electron and neutron beams also fulfill the diffraction condition. Unlike X-rays interacting with the electron cloud surrounding the atom, electrons interact with the electron potential (positively-charged core of the atom), while neutrons interact with the nuclei or unpaired electron spin. The distribution of nuclei or unpaired electron spins, electrons, and electronic potentials are similar in the same crystal, which is established by the structure of material [70-72]. Therefore, these three diffractions provide complementary information of the atomic arrangement in a material. The details explanation of neutron diffraction is given on the next section.

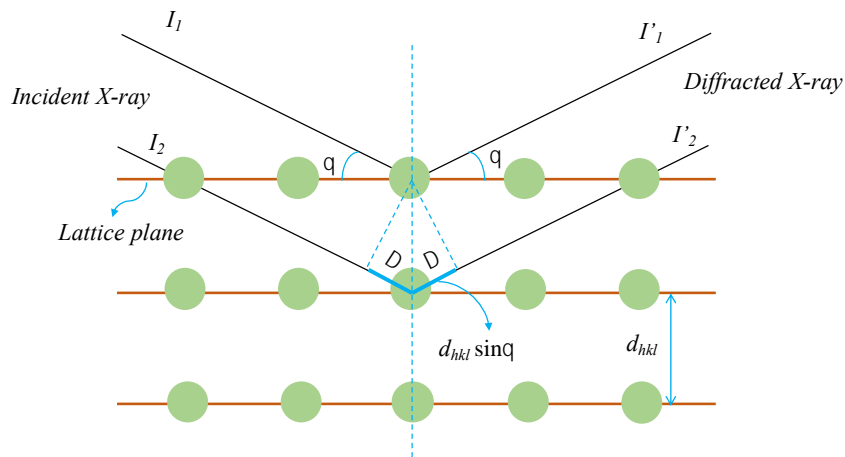


Figure 2. 5 Geometrical illustration of Bragg's Law. The green solid circles denote the lattice points. The diffraction maximum appears when the path difference  $2\Delta$ , which is equal to  $2d_{hkl}\sin\theta$ , add to a multiple of the incident wavelength.

Diffraction from crystalline sample can be explained using the Bragg's Law [73], which is geometrically illustrated in Figure 2.5. This law relates the wavelength  $\lambda$  to the angle  $\theta$  formed by the incident and diffracted X-ray with the lattice plane ( $hkl$ ) and the inter-plane distance  $d_{hkl}$ . The set of lattice planes is denoted by Miller indices

( $hkl$ ) where  $h$ ,  $k$ , and  $l$  are the reciprocal of the fractional intercepts on an axis. For constructive interference between incident  $I_1$  and  $I_2$ , the path difference between  $I_1$  and  $I_2$  has to be an integral multiple  $n$  of  $\lambda$ , given by the following equation [71]

$$\lambda = 2d_{hkl}\sin\theta \quad (2.1)$$

where  $n$  is an integer indicating the order of the diffraction peak. The whole range of d-spacings are measured at fixed wavelength by scanning in angle  $\theta$ .

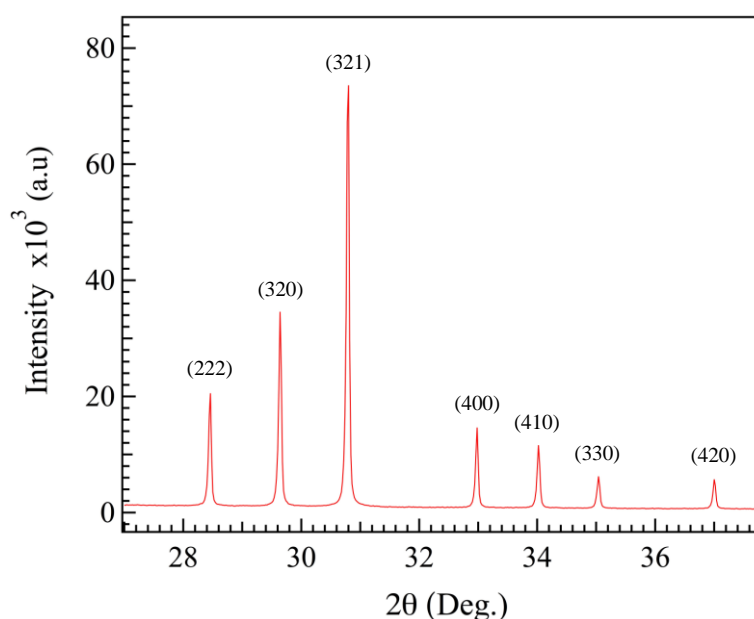


Figure 2. 6 X-ray diffraction pattern of  $Ba_8Al_{16}Ge_{30}$ . The peaks are indexed according to the  $Pm\bar{3}n$  space.

We have used a Rigaku smartlab X-ray diffractometer (Cu  $K\alpha$  radiation) at room temperature for checking the sample quality before doing further experiment using neutron diffraction. The ingots were ground into a fine powder and measured for approximately one hour. A typical of X-ray diffraction pattern for  $Ba_8Al_{16-x}Ga_xGe_{30}$  with space group  $Pm\bar{3}n$  is presented in Figure 2.6.

### 2.3 Impurity Checking by XRD

X-ray diffraction (XRD) patterns of the five  $\text{Ba}_8\text{Al}_{16-x}\text{Ga}_x\text{Ge}_{30}$  (BAGG) are shown at Figure 2. 7. Impurity peaks are observed for the samples with  $x = 0, 2, 4,$  and  $6$ . They contain excesses of raw materials (Ge and Al) and  $\text{Al}_2\text{BaO}_4$ . The weight percentages of five phases are given in Table 2. 1. The ratio of type-I clathrate increases with increasing the Ga concentration and vice versa for oxide phase.

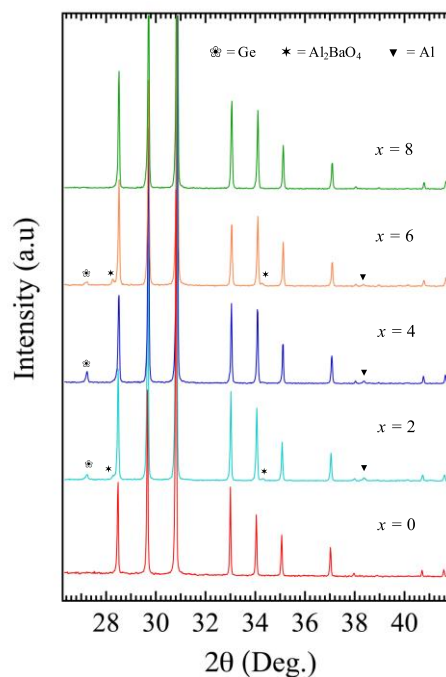


Figure 2. 7 XRD pattern of the  $\text{Ba}_8\text{Al}_{16-x}\text{Ga}_x\text{Ge}_{30}$  (BAGG) samples with the labeled peaks of the impurity peaks. The flowers, stars, and pointing down triangles are Ge,  $\text{Al}_2\text{BaO}_4$ , and Al peaks, respectively.

There is no type-VIII clathrate phase observed for all samples as found in other quaternary clathrate systems which use the same combination of Al and Ga host atoms,  $\text{Sr}_8\text{Al}_x\text{Ga}_{16-x}\text{Ge}_{30}$  [82] and  $\text{Sr}_8\text{Al}_x\text{Ga}_{16-x}\text{Si}_{30}$  [83]. Type-VIII clathrate belonging to the space group  $I\bar{4}3m$  has the same chemical formula  $\text{G}_8\text{A}_y\text{B}_{46-y}$  as the type I clathrate [40].

Table 2. 1 The weight percentages of the four phases in sample  $Ba_8Al_{16-x}Ga_xGe_{30}$

Sample	Type I Clathrate (%)	Ge (%)	Al (%)	$Al_2BaO_4$ (%)
$x = 0$	100.00	0	0	0
$x = 2$	96.365	1.095	1.164	1.376
$x = 4$	96.995	1.720	0	1.285
$x = 6$	97.039	0.823	1.497	0.641
$x = 8$	100.00	0	0	0

# Chapter 3

## Structural Analysis of $\text{Ba}_8\text{Al}_{16-x}\text{Ga}_x\text{Ge}_{30}$

### 3.1 Neutron Powder Diffraction

Neutron intrinsic properties can be utilized as a powerful probe to study the structure and dynamic of materials. As the neutron has no charge, it is able to penetrate the bulk materials. Neutron is scattered by the nuclei via strong nuclear forces, in a range of 5 magnitude order smaller than its wavelength. The wavelength of neutron is comparable to the atomic sizes and interplanar distance (from 0.1 Å to 100 Å), allowing the diffraction to be occurred when the material is subjected by neutron [74-76]. Neutron diffraction can provide precise data of structural details, for example data on the mean square displacement of atoms around the average position, called atomic displacement parameters (ADPs) and precise occupancy information. In principle, neutron diffraction is similar to X-ray diffraction, satisfying the Bragg's Law. However, due to the weak interaction of neutron with matter, a large amount of sample is needed [76-78].

Neutron powder diffraction measurements were conducted using time-of-flight diffractometer, Super High-Resolution Powder Diffractometer (SuperHRPD), at BL08 beamline of Material and Life Science Experimental Facility (MLF), Japan Proton Accelerator Research Complex (J-PARC) [79]. This facility uses the time-of-flight (TOF) technique to optimize the use of the white neutron beams produced by the pulsed neutron source, where the accelerated protons are injected into liquid mercury target at a repetition rates of 25 Hz [80]. The instrument resolution ( $\Delta d/d$ ) reaches  $\sim 0.03\%$  at  $2\theta = 172^\circ$ . The instrument illustration is shown in the Figure 3.1.

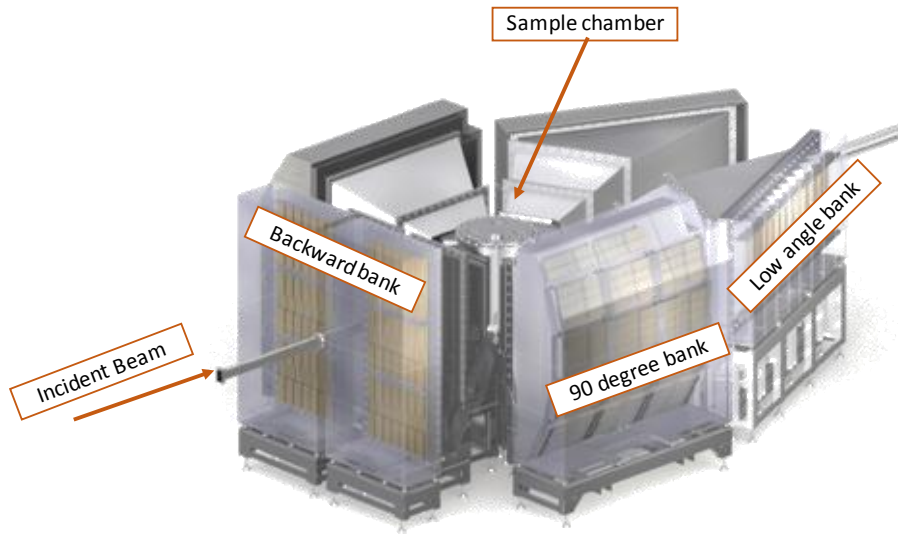


Figure 3. 1 Illustration of Super High-Resolution Powder Diffractometer (SuperHRPD) with resolution of  $\Delta d/d=0.03\%$  [26].

For the TOF technique, the neutron wavelength  $\lambda$  can be obtained using the de Broglie equation by knowing the flight path  $L$  and measuring the coming time  $t$  of neutron at detector, called time-of-flight (TOF), expressed as follow [78, 81]

$$\lambda = \frac{ht}{mL} \quad (3. 1)$$

where  $h$  and  $m$  are the planck constant ( $6.62 \times 10^{-34}$  Js) and neutron mass ( $1.675 \times 10^{-27}$  kg), respectively. By combining the Eqs. (2.1) and (2.2), one yields

$$t = 252.777 (L 2d \sin\theta) \quad (3. 2)$$

Contrary to the X-ray diffraction, the scattering angle  $2\theta$  is chosen (fixed) by scanning in wavelength during the range of d-spacings measurement.

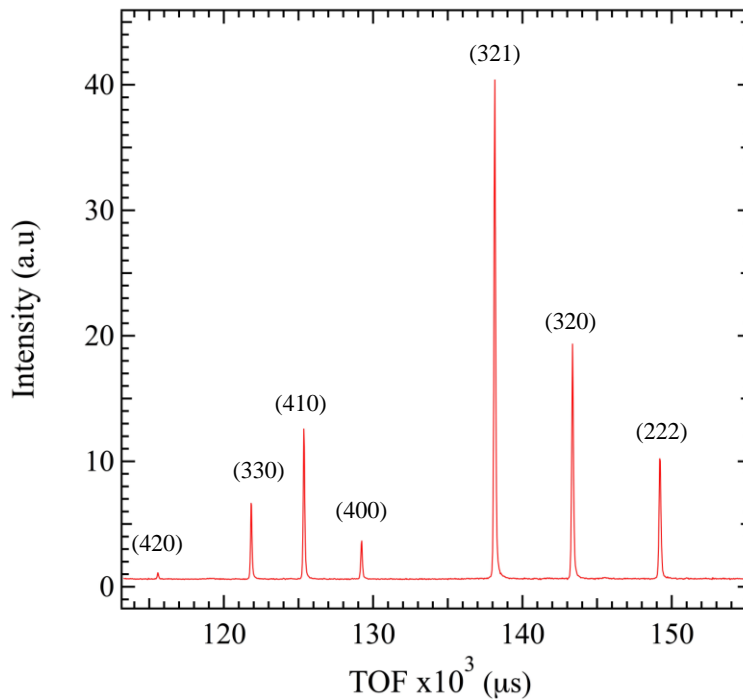


Figure 3. 2 X-ray diffraction pattern of  $Ba_8Al_{16}Ge_{30}$ . The peak indexing is based on the  $Pm-3n$  space group.

A top-loading typed cryostat and a vanadium furnace were used to collect data from 10 to 300 K and 400 to 900 K, respectively. The samples were encapsulated in a vanadium sample holder with 6 mm in diameter and 40 mm in height for low temperature measurement. Only samples with Ga = 0 and Ga = 8 are measured at high temperature. Since high temperature measurement is prohibited for powder sample at the facility, the melted ingot of sample with Ga = 0 and Ga = 8 were only crushed to several pieces in order to put them into the 10 mm vanadium sample holder. For each temperature point, the measurement was carried out for approximately 10 hours with average beam power of 150 kW to ensure a good data quality. The other two compositions were only scanned at low temperature. A typical of neutron diffraction pattern for  $Ba_8Al_{16-x}Ga_xGe_{30}$  is presented in Figure 3.2.

## 3.2 Neutron Powder Diffraction Results

The experimental data were analyzed by a combination of the Rietveld method using *Z-Rietveld* software [84] and Maximum Entropy Method (MEM) using *Z-MEM* software [85]. The nuclear density map of the structure, result of MEM calculation, was visualized using *Z-3D* software [86]. The refinements of neutron data were carried out with two models for the guest atom, *6d* and *24k* model, as shown in Fig. 3.1. These two models correspond to the position of the Ba2 guest atom. The position of the Ba2 guest atom is assumed to be located at the center of the cage in *6d* model, while off-centered position with partial occupancy, in *24k* model. Isotropic and anisotropic displacement parameters were used to refine Ba2 guest atom in the *24k* model and *6d* model, respectively. The host atoms are constrained to be fully occupied and the same atomic displacement parameter for all three different sites. The selected crystallographic information of BAGG are summarized in Table 3.1.

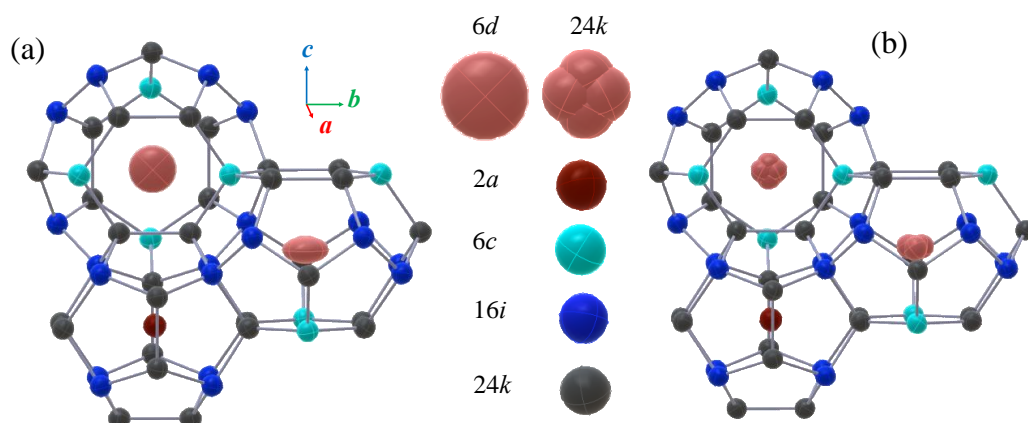


Figure 3. 3 (a) The *6d* model) and (b)*24k* model using for the refinement of neutron diffraction data.

### 3.2.1 Results of $\text{Ba}_8\text{Al}_{16}\text{Ge}_{30}$ ( $\text{Ga} = 0$ )

Clathrate compound  $\text{Ba}_8\text{Al}_{16}\text{Ge}_{30}$  were measured from 10 to 900 K. The collected diffraction data are shown in Figure 3. 4. The Bragg reflection peaks of  $\text{Ba}_8\text{Al}_{16}\text{Ge}_{30}$  are shifted to the higher  $d$  spacing at elevated temperature indicating the increasing of lattice unit. The representative result of Rietveld refinements of  $\text{Ba}_8\text{Al}_{16}\text{Ge}_{30}$  is displayed in Figure 3.5.

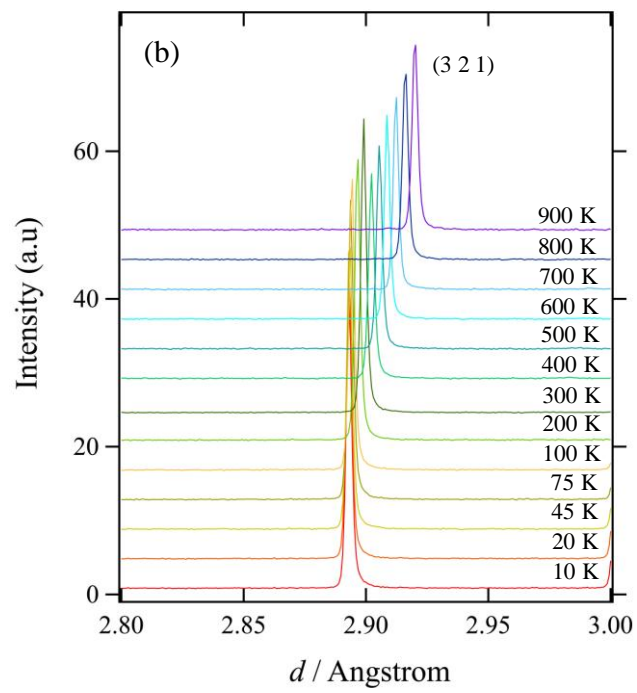
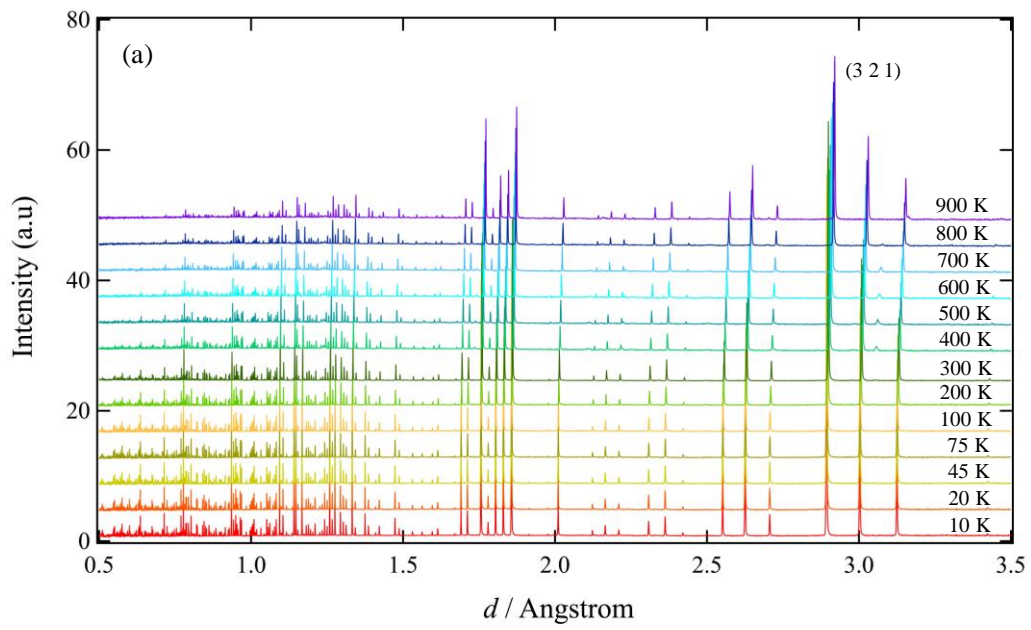


Figure 3. 4 (a) Neutron diffraction patterns as function of  $d$  spacing at various temperature (b) Bragg peak positions shifted to the higher  $d$  spacing as temperature increases.

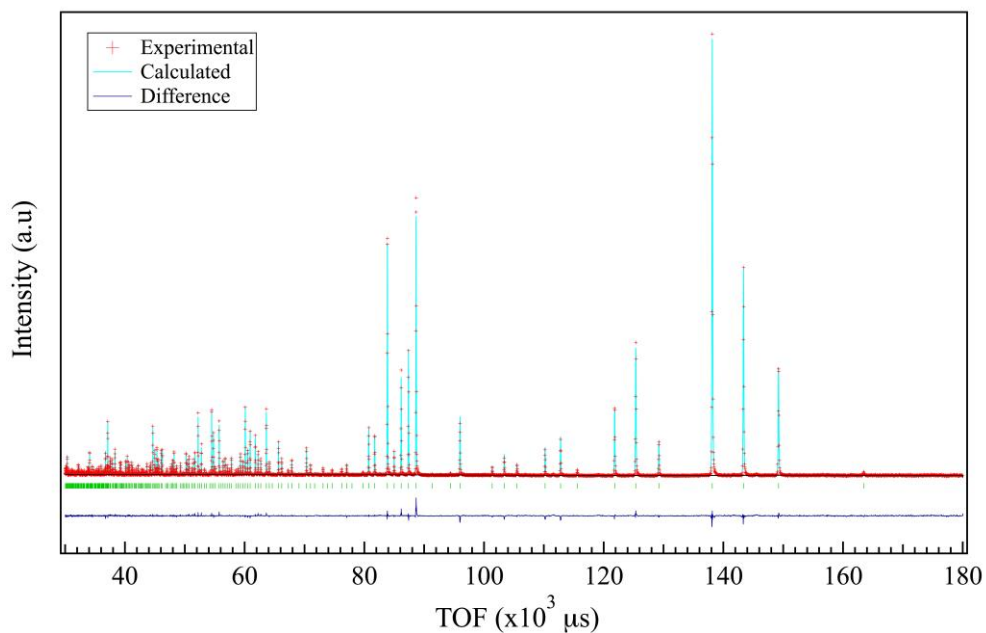


Figure 3. 5 Rietveld refinement result for neutron diffraction data of  $Ba_8Al_{16}Ge_{30}$  at 300 K refined using the 6d model. Red cross (+ symbols) and light blue line correspond to the observed and calculated intensity, respectively. The dark blue line denotes the difference between calculated and observed intensities. The short vertical green line indicates the Bragg reflection positions.

Results of refinement are shown in Table 3.1 and Table 3.2 for the site occupancies factors of host atoms and the crystallographic information for the selected temperature points, respectively. As shown by Table 3.1, the 6c position is the site preference for Al atoms while Ge atoms dominantly occupied the 16i and 24k sites.

Table 3. 1 The site occupancies factors of host atoms

$Ba_8Al_{16}Ge_{30}$	Al (%)	Ge (%)
6c	67.2(5)	32.8
16i	32.0(5)	68
24k	28.5(5)	71.5

Table 3. 2 Crystallographic information of  $Ba_8Al_{16}Ge_{30}$  at the selected temperature points. The atomic coordinates in the refinements: Ba1 2a (0,0,0), Ba2 6d (1/4,1/2,0) or 24k (x,1/2,z), Al1/Ge1 6c (1/4,0,1/2), Al2/Ge2 16i (x, x, x), and Al3/Ge3 24k (0,y,z).

RT	10 K		300 K		600 K	
unit cell (Å)	10.825420(6)		10.848101(5)		10.883973(7)	
model	6d	24k	6d	24k	6d	24k
$U_{iso}$ (Ba1) (Å <sup>2</sup> )	0.0021(4)	0.0025(4)	0.0072(5)	0.0099(4)	0.0127(9)	0.0140(9)
$U_{iso}$ (Ba2) (Å <sup>2</sup> )	0.0160(3)	0.0035(9)	0.0346(5)	0.0150(8)	0.0450(8)	0.0217(19)
x (Ba2)	0.25	0.2455(8)	0.25	0.2472(8)	0.25	0.2552(14)
z (Ba2)	0	0.0168(5)	0	0.0213(4)	0	0.0231(7)
$U_{11}$ (Ba2) (Å <sup>2</sup> )	0.0067(7)		0.0168(7)		0.0251(15)	
$U_{22}$ (Ba2) (Å <sup>2</sup> )	0.0212(5)		0.0444(6)		0.0566(12)	
$U_{iso}$ (host) (Å <sup>2</sup> )	0.00257(7)	0.00251(7)	0.00773(6)	0.00875(8)	0.01366(14)	0.01343(14)
x (Ge2)	0.18448(3)	0.18452(3)	0.18434(3)	0.18443(3)	0.18444(5)	0.18444(5)
y (Ge3)	0.30854(4)	0.30852(4)	0.30820(4)	0.30831(4)	0.30828(6)	0.30828(6)
z (Ge3)	0.11670(4)	0.11662(4)	0.11691(4)	0.11689(4)	0.11774(7)	0.11774(7)
$\chi^2$	1.405	1.402	1.537	1.532	1.886	1.887
$R_{wp}, R_F$ (%)	4.13, 4.91	4.12, 4.86	3.86, 6.66	3.85, 6.52	3.27, 8.51	3.27, 8.46

### 3.2.2 Results of $Ba_8Al_{14}Ga_2Ge_{30}$ (Ga = 2)

Clathrate compound  $Ba_8Al_{14}Ga_2Ge_{30}$  were measured from 10 to 300 K. The collected diffraction data are shown in Figure 3. 6. The Bragg reflection peaks of  $Ba_8Al_{14}Ga_2Ge_{30}$  are shifted to the higher  $d$  spacing at elevated temperature indicating the increasing of lattice unit. The representative result of Rietveld refinements of  $Ba_8Al_{14}Ga_2Ge_{30}$  is displayed in Figure 3.7. The impurities peaks of Ge and Al are observed as revealed previously by XRD.

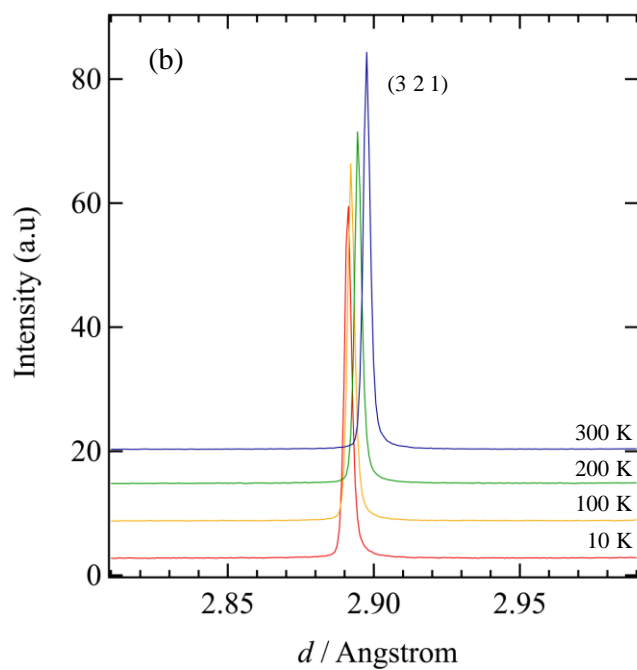
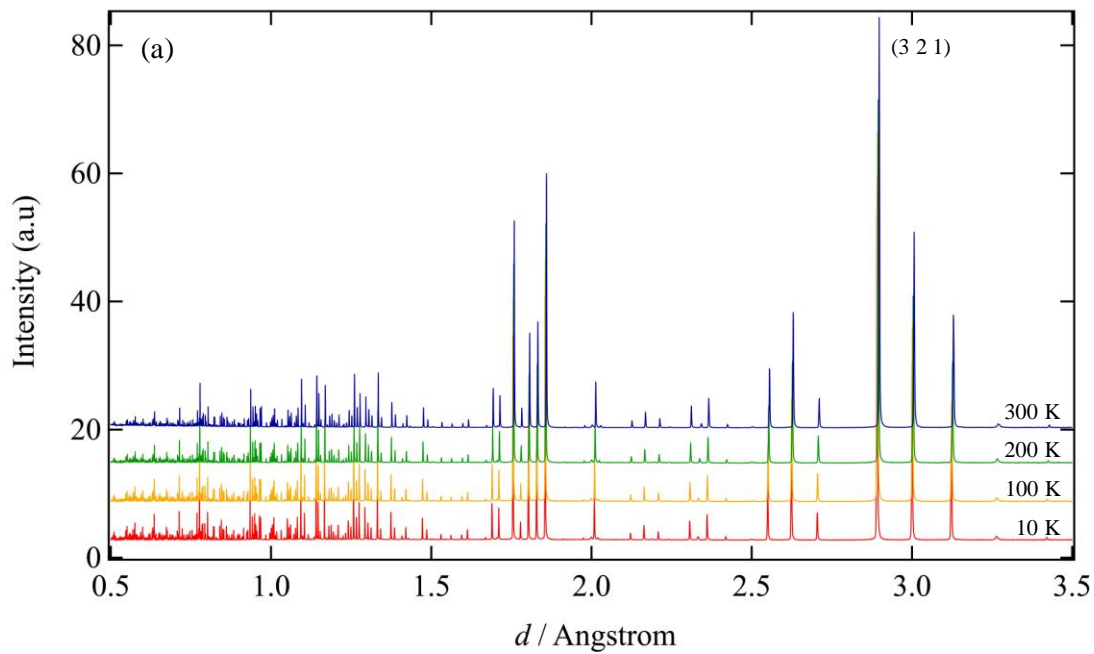


Figure 3. 6 (a) Neutron diffraction patterns as function of  $d$  spacing at various temperature (b) 321 reflection of  $Ba_8Al_{14}Ga_2Ge_{30}$  shifted to the higher  $d$  spacing as temperature increases.

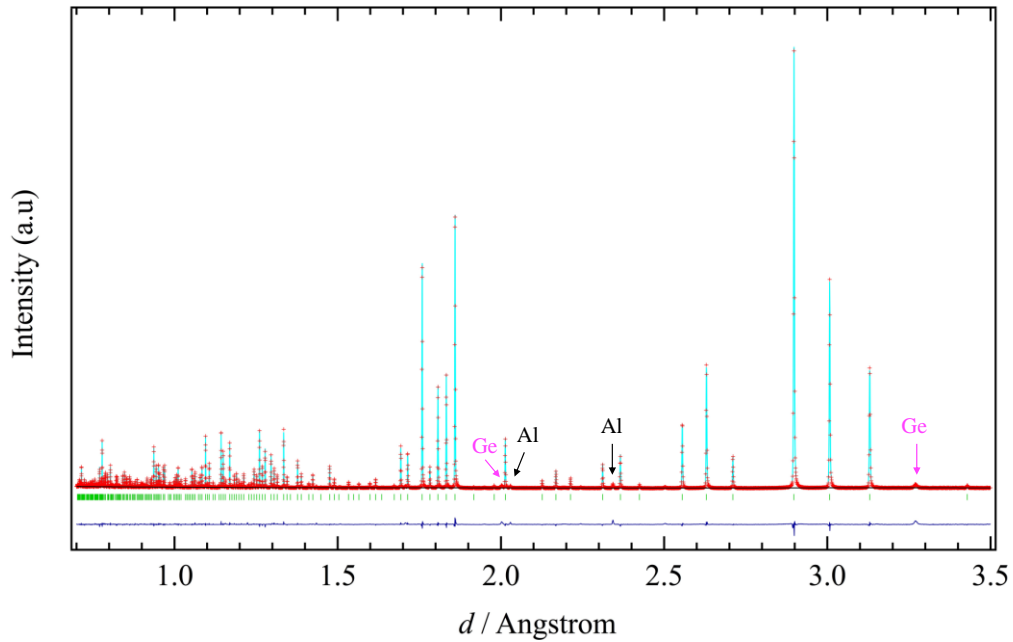


Figure 3. 7 Rietveld refinement result for neutron diffraction data of  $Ba_8Al_{14}Ga_2Ge_{30}$  at 300 K refined using the 6d model. Red cross (+ symbols) and light blue line correspond to the observed and calculated intensity, respectively. The dark blue line denotes the difference between calculated and observed intensities. The short vertical green line indicates the Bragg reflection positions. The black and pink arrows denote the impurities peaks of Al and Ge, respectively.

Results of refinement are shown in Table 3.3 and Table 3.4 for the site occupancies factors of host atoms and the crystallographic information for the selected temperature points, respectively. As shown by Table 3.3, the 6c position is the site preference for Al atoms while Ge atoms dominantly occupied the 16i and 24k sites. While Ga atoms occupied mostly at 24k site.

Table 3. 3 The site occupancies factors of host atoms for  $Ba_8Al_{14}Ga_2Ge_{30}$  sample

$Ba_8Al_{16}Ge_{30}$	Al (%)	Ga (%)	Ge (%)
6c	65.1(2)	1.6(2)	33.3(2)
16i	28.66(10)	2.86(5)	68.48(5)
24k	22.95(7)	6.01(7)	71.04(7)

Table 3. 4 Crystallographic information of  $Ba_8Al_{14}Ga_2Ge_{30}$  at the selected temperature points. The atomic coordinates in the refinements: Ba1 2a (0,0,0), Ba2 6d (1/4,1/2,0) or 24k (x,1/2,z), Al1/Ge1 6c (1/4,0,1/2), Al2/Ge2 16i (x, x, x), and Al3/Ge3 24k (0,y,z).

RT	10 K		300 K	
unit cell (Å)	10.818513(3)		10.842604(4)	
model	6d	24k	6d	24k
$U_{iso}$ (Ba1) (Å <sup>2</sup> )	0.0005(3)	0.0013(3)	0.0078(3)	0.0092(4)
$U_{iso}$ (Ba2) (Å <sup>2</sup> )	0.0155(2)	0.0040(5)	0.0346(3)	0.0153(6)
x (Ba2)	0.25	0.2483(7)	0.25	0.2483(7)
z (Ba2)	0	0.0167(3)	0	0.0216(3)
$U_{11}$ (Ba2) (Å <sup>2</sup> )	0.0052(4)		0.0167(6)	
$U_{22}$ (Ba2) (Å <sup>2</sup> )	0.0215(3)		0.0453(5)	
$U_{iso}$ (host) (Å <sup>2</sup> )	0.00202(5)	0.00195(5)	0.00853(6)	0.00839(6)
x (Ge2)	0.18439(2)	0.18444(2)	0.18444(2)	0.18450(2)
y (Ge3)	0.30849(2)	0.30847(2)	0.30834(3)	0.30835(3)
z (Ge3)	0.11679(2)	0.11671(2)	0.11692(3)	0.11682(3)
$\chi^2$	3.26	3.25	2.84	2.83
$R_{wp}, R_F$ (%)	4.127, 3.14	4.120, 3.12	3.814, 4.15	3.804, 4.07

### 3.2.3 Results of $Ba_8Al_{12}Ga_4Ge_{30}$ (Ga = 4)

Clathrate compound  $Ba_8Al_{12}Ga_4Ge_{30}$  were measured from 10 to 300 K. The collected diffraction data are shown in Figure 3. 8. The Bragg reflection peaks of  $Ba_8Al_{12}Ga_4Ge_{30}$  are shifted to the higher  $d$  spacing at elevated temperature indicating the increasing of lattice unit. The representative result of Rietveld refinements of  $Ba_8Al_{14}Ga_2Ge_{30}$  is displayed in Figure 3.9. The impurities peaks of Ge and Al are observed as revealed previously by XRD.

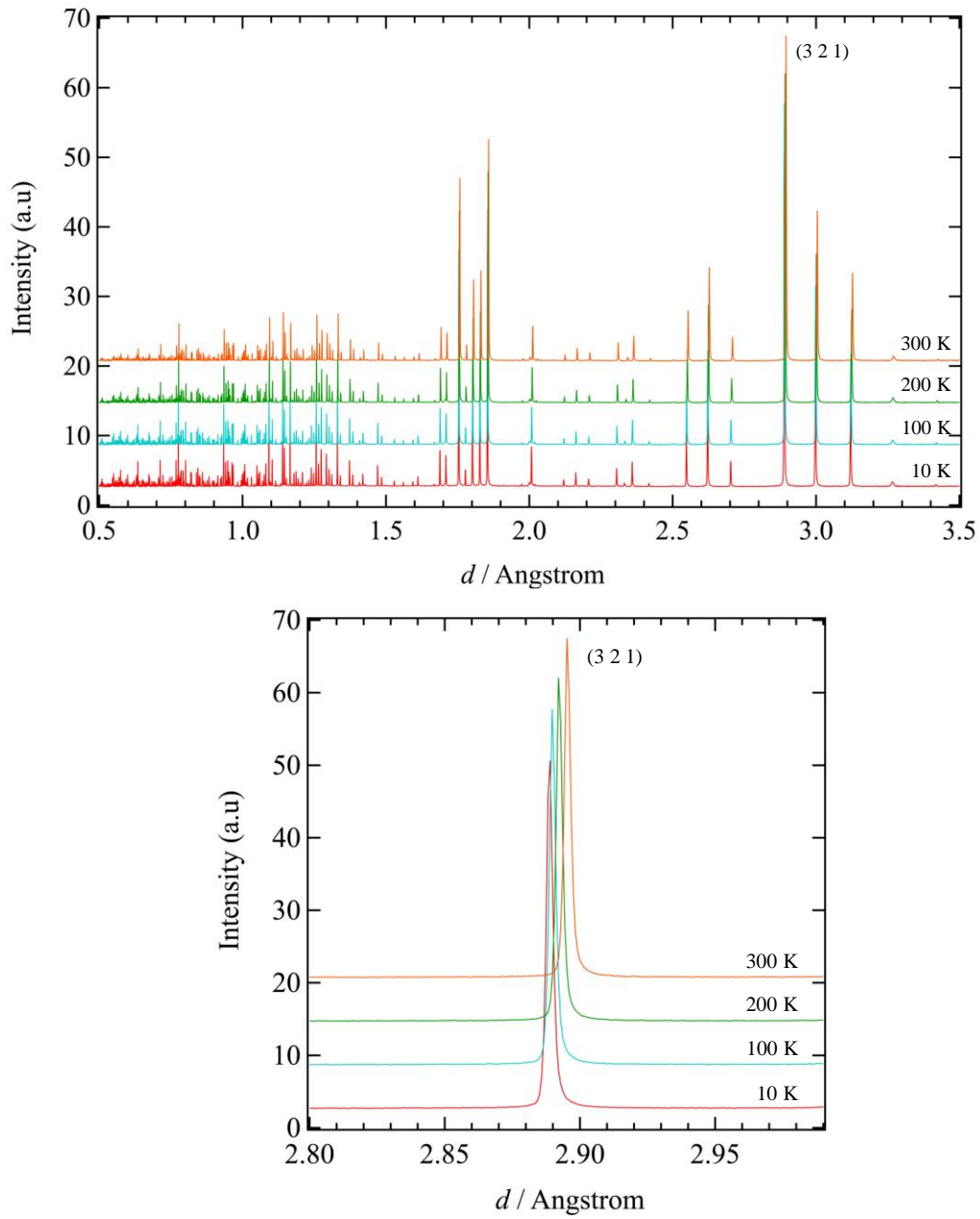


Figure 3. 8 (a) Neutron diffraction patterns as function of  $d$  spacing at various temperature (b) 321 reflection of  $Ba_8Al_{12}Ga_4Ge_{30}$  shifted to the higher  $d$  spacing as temperature increases.

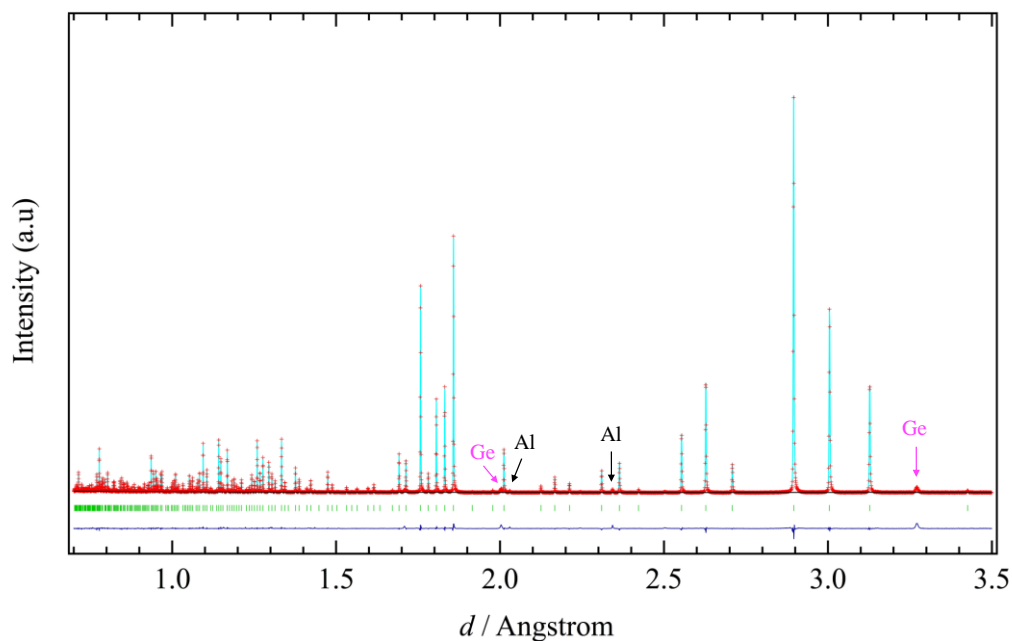


Figure 3. 9 Rietveld refinement result for neutron diffraction data of  $Ba_8Al_{12}Ga_4Ge_{30}$  at 300 K refined using the 6d model. Red cross (+ symbols) and light blue line correspond to the observed and calculated intensity, respectively. The dark blue line denotes the difference between calculated and observed intensities. The short vertical green line indicates the Bragg reflection positions. The black and pink arrows denote the impurities peaks of Al and Ge, respectively.

Results of refinement are shown in Table 3.5 and Table 3.6 for the site occupancies factors of host atoms and the crystallographic information for the selected temperature points, respectively. As shown by Table 3.5, the 6c position is the site preference for Al atoms while Ge atoms dominantly occupied the 16i and 24k sites. While Ga atoms occupied mostly at 24k site.

Table 3. 5 The site occupancies factors of host atoms for  $Ba_8Al_{12}Ga_4Ge_{30}$  sample

$Ba_8Al_{16}Ge_{30}$	Al (%)	Ga (%)	Ge (%)
6c	62.39(21)	5.65(12)	31.95(9)
16i	24.74(11)	6.89(6)	68.37(5)
24k	17.91(7)	10.66(4)	71.43(3)

Table 3. 6 Crystallographic information of  $Ba_8Al_{12}Ga_4Ge_{30}$  at the selected temperature points. The atomic coordinates in the refinements: Ba1 2a (0,0,0), Ba2 6d (1/4,1/2,0) or 24k (x,1/2,z), Al1/Ge1 6c (1/4,0,1/2), Al2/Ge2 16i (x, x, x), and Al3/Ge3 24k (0,y,z).

RT	10 K		300 K	
unit cell (Å)	10.809651(4)		10.834352(4)	
model	6d	24k	6d	24k
$U_{iso}$ (Ba1) (Å <sup>2</sup> )	0.0017(3)	0.0023(3)	0.0088(4)	0.0100(4)
$U_{iso}$ (Ba2) (Å <sup>2</sup> )	0.0136(2)	0.0038(5)	0.0324(3)	0.0142(8)
x (Ba2)	0.25	0.2494(9)	0.25	0.2467(8)
z (Ba2)	0	0.0157(3)	0	0.0207(3)
$U_{11}$ (Ba2) (Å <sup>2</sup> )	0.0048(5)		0.0169(7)	
$U_{22}$ (Ba2) (Å <sup>2</sup> )	0.0187(3)		0.0415(5)	
$U_{iso}$ (host) (Å <sup>2</sup> )	0.00165(5)	0.00159(5)	0.00814(7)	0.00803(7)
x (Ge2)	0.18440(2)	0.18444(2)	0.18444(3)	0.18450(3)
y (Ge3)	0.30821(3)	0.30819(3)	0.30821(3)	0.30822(3)
z (Ge3)	0.11691(3)	0.11685(3)	0.11712(3)	0.11703(3)
$\chi^2$	3.452	3.450	2.922	2.911
$R_{wp}, R_F$ (%)	4.466, 3.87	4.461, 3.81	4.100, 4.74	4.091, 4.69

### 3.2.4 Results of $Ba_8Al_{10}Ga_6Ge_{30}$ (Ga = 6)

Clathrate compound  $Ba_8Al_{10}Ga_6Ge_{30}$  were measured only at 300 K. The collected diffraction data was refined by Rietveld method and the refinement result are shown in Figure 3. 10. The impurities peaks of Ge and Al are observed as revealed previously by XRD.

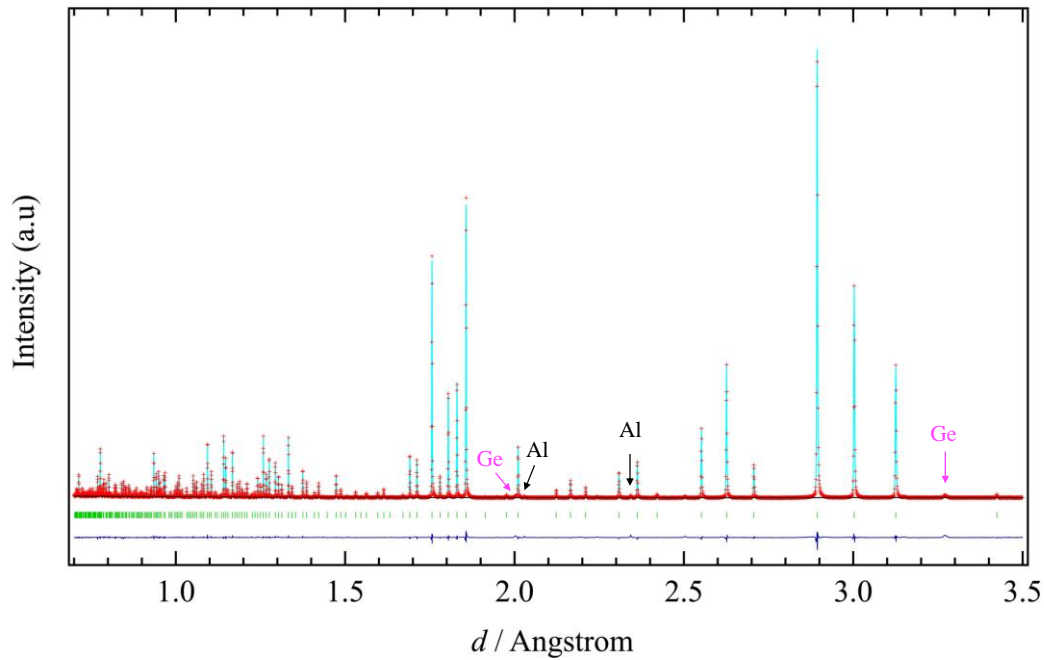


Figure 3. 10 Rietveld refinement result for neutron diffraction data of  $Ba_8Al_{10}Ga_6Ge_{30}$  at 300 K refined using the 6d model. Red cross (+ symbols) and light blue line correspond to the observed and calculated intensity, respectively. The dark blue line denotes the difference between calculated and observed intensities. The short vertical green line indicates the Bragg reflection positions. The black and pink arrows denote the impurities peaks of Al and Ge, respectively.

Results of refinement are shown in Table 3.7 and Table 3.8 for the site occupancies factors of host atoms and the crystallographic information for the selected temperature points, respectively. As shown by Table 3.7, the 6c position is the site preference for Al atoms while Ge atoms dominantly occupied the 16i and 24k sites. While Ga atoms occupied mostly at 6c site.

Table 3. 7 The site occupancies factors of host atoms for  $Ba_8Al_{10}Ga_6Ge_{30}$  sample

$Ba_8Al_{10}Ga_6Ge_{30}$	Al (%)	Ga (%)	Ge (%)
6c	54.22(21)	17.67(12)	28.11(9)
16i	19.86(10)	10.70(6)	69.44(5)
24k	14.87(7)	13.45(4)	71.67(3)

Table 3. 8 Crystallographic information of  $Ba_8Al_{12}Ga_4Ge_{30}$  at 300 K. The atomic coordinates in the refinements: Ba1 2a (0,0,0), Ba2 6d (1/4,1/2,0) or 24k (x,1/2,z), Al1/Ge1 6c (1/4,0,1/2), Al2/Ge2 16i (x, x, x), and Al3/Ge3 24k (0,y,z).

RT	300 K	
unit cell (Å)	10.827042(4)	
model	6d	24k
$U_{iso}$ (Ba1) (Å <sup>2</sup> )	0.0078(3)	0.0089(4)
$U_{iso}$ (Ba2) (Å <sup>2</sup> )	0.0348(3)	0.0161(7)
x (Ba2)	0.25	0.2475(7)
z (Ba2)	0	0.0211(3)
$U_{11}$ (Ba2) (Å <sup>2</sup> )	0.0174(6)	
$U_{22}$ (Ba2) (Å <sup>2</sup> )	0.0449(5)	
$U_{iso}$ (host) (Å <sup>2</sup> )	0.00762(6)	0.00748(5)
x (Ge2)	0.18445(2)	0.18449(2)
y (Ge3)	0.30816(3)	0.30817(3)
z (Ge3)	0.11722(3)	0.11715(3)
$\chi^2$	2.71	2.70
$R_{wp}, R_F$ (%)	5.41, 2.88	5.40, 2.83

### 3.2.5 Results of $Ba_8Al_8Ga_8Ge_{30}$ (Ga = 8)

Clathrate compound  $Ba_8Al_8Ga_8Ge_{30}$  were measured from 10 to 900 K. The collected diffraction data are shown in Figure 3. 11. The Bragg reflection peaks of  $Ba_8Al_8Ga_8Ge_{30}$  are shifted to the higher  $d$  spacing at elevated temperature indicating the increasing of lattice unit. The representative result of Rietveld refinements of  $Ba_8Al_8Ga_8Ge_{30}$  is displayed in Figure 3.12.

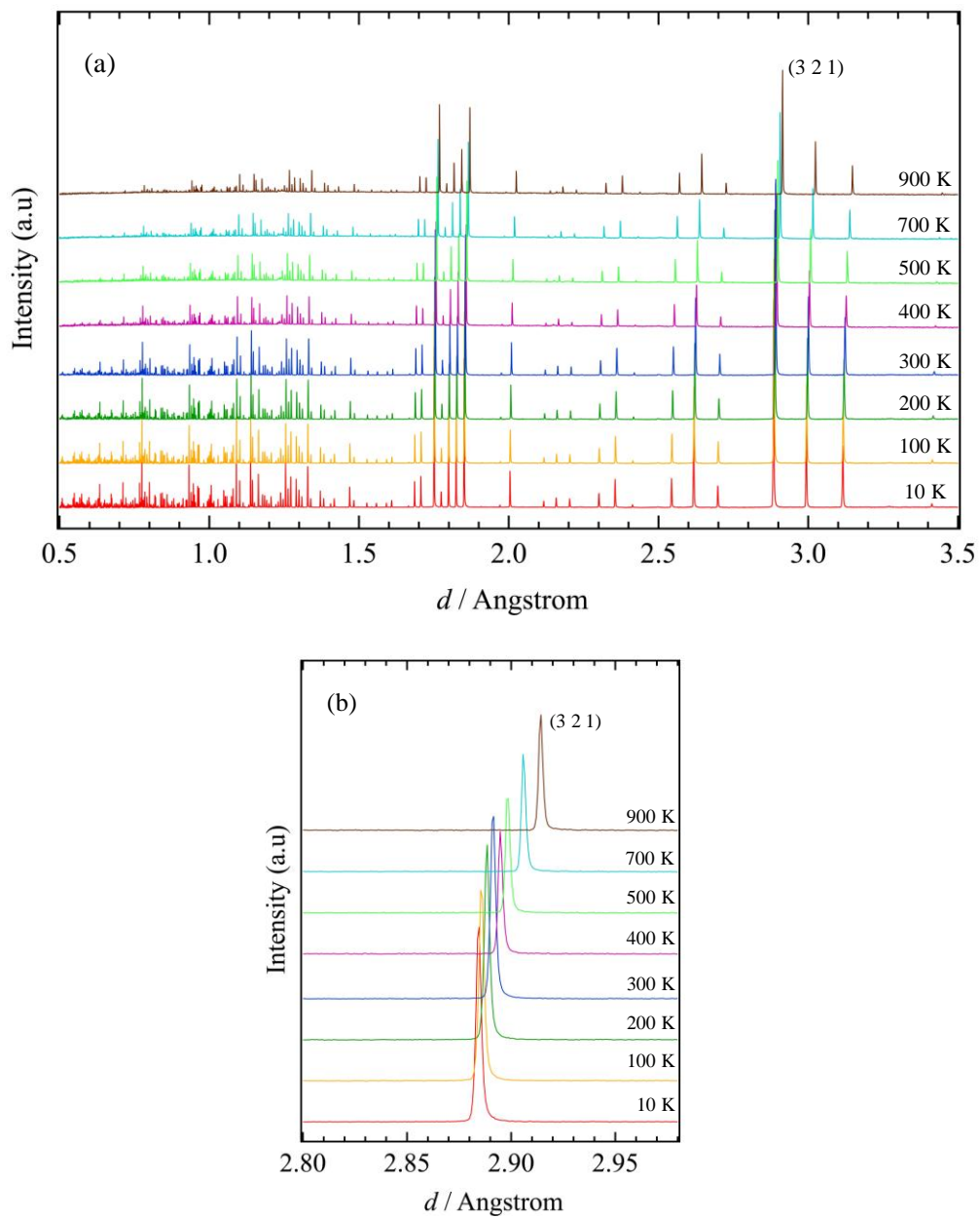


Figure 3. 11 (a) Neutron diffraction patterns as function of  $d$  spacing at various temperature (b) Bragg peak positions shifted to the higher  $d$  spacing as temperature increases.

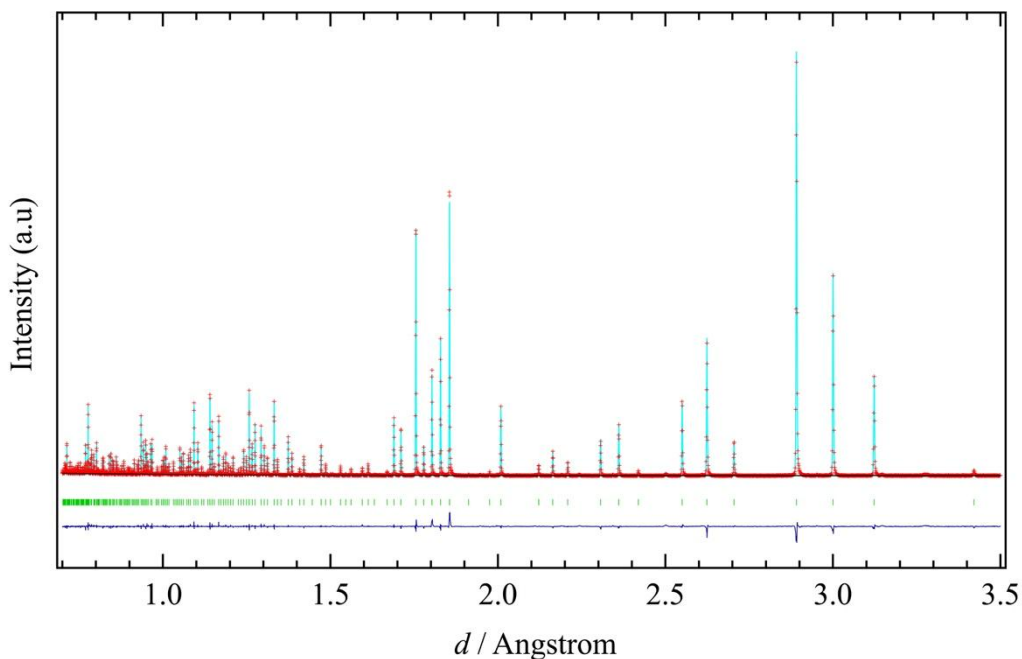


Figure 3. 12 Rietveld refinement result for neutron diffraction data of  $Ba_8Al_8Ga_8Ge_{30}$  at 300 K refined using the 6d model. Red cross (+ symbols) and light blue line correspond to the observed and calculated intensity, respectively. The dark blue line denotes the difference between calculated and observed intensities. The short vertical green line indicates the Bragg reflection positions.

Results of refinement are shown in Table 3.9 and Table 3.10 for the site occupancies factors of host atoms and the crystallographic information for the selected temperature points, respectively. As shown by Table 3.9, the 6c position is the site preference for Al atoms while Ge atoms dominantly occupied the 16i and 24k sites. While Ga atoms occupied mostly at 6c site and similar percentage of distribution at 16i and 24k.

Table 3. 9 The site occupancies factors of host atoms for  $Ba_8Al_8Ga_8Ge_{30}$  sample

$Ba_8Al_{16}Ge_{30}$	Al (%)	Ga (%)	Ge (%)
6c	50.65(23)	18.88(13)	30.47(10)
16i	12.73(12)	17.10(6)	70.17(5)
24k	12.52(8)	17.22(4)	70.27(3)

Table 3. 10 Crystallographic information of  $Ba_8Al_8Ga_8Ge_{30}$  at the selected temperature points. The atomic coordinates in the refinements: Ba1 2a (0,0,0), Ba2 6d (1/4,1/2,0) or 24k (x,1/2,z), Al1/Ge1 6c (1/4,0,1/2), Al2/Ge2 16i (x, x, x), and Al3/Ge3 24k (0,y,z).

RT	10 K		300 K		500 K	
unit cell (Å)	10.792671(4)		10.818767(4)		10.845068(7)	
model	6d	24k	6d	24k	6d	24k
$U_{iso}$ (Ba1) (Å <sup>2</sup> )	0.0004(3)	0.0012(3)	0.0094(4)	0.0101(4)	0.0119(9)	0.0125(9)
$U_{iso}$ (Ba2) (Å <sup>2</sup> )	0.0172(3)	0.0054(7)	0.0347(3)	0.0181(10)	0.0529(9)	0.035(3)
x (Ba2)	0.25	0.2473(8)	0.25	0.2439(7)	0.25	0.256(2)
z (Ba2)	0	0.0171(4)	0	0.0191(4)	0	0.0196(12)
$U_{11}$ (Ba2) (Å <sup>2</sup> )	0.0068(5)		0.0239(7)		0.0399(18)	
$U_{22}$ (Ba2) (Å <sup>2</sup> )	0.0232(4)		0.0408(5)		0.0600(13)	
$U_{iso}$ (host) (Å <sup>2</sup> )	0.00388(6)	0.00407(5)	0.00906(6)	0.00901(6)	0.01288(12)	0.01280(12)
x (Ge2)	0.18470(2)	0.18473(2)	0.18447(2)	0.18450(2)	0.18502(5)	0.18505(5)
y (Ge3)	0.30735(3)	0.30733(3)	0.30836(3)	0.30835(3)	0.30758(7)	0.30762(7)
z (Ge3)	0.11774(3)	0.11765(3)	0.11742(3)	0.11736(3)	0.11755(7)	0.11753(7)
$\chi^2$	4.08	4.10	2.68	2.68	2.22	2.23
$R_{wp}$ , $R_F$ (%)	5.38, 5.01	5.39, 5.13	6.59, 3.38	6.58, 3.32	2.90, 11.6	2.90, 10.11

### 3.2.6 Discussion

The substitution of aluminum with gallium which has bigger ionic radii was expected to enlarge the lattice size of BAGG. However, Table 3.11 and Figure 3.13a show that the unit cell size of BAGG become smaller by increasing the Ga concentration. The unit cell of  $Ba_8Al_{16}Ge_{30}$  agrees with the result of Christensen et al. [53] for sample grown by stoichiometric mixing, which is larger than  $Ba_8Ga_{16}Ge_{30}$  system about 0.05 to 0.08 Å [35]. While, sample with  $x = 8$  has unit cell size approaching the unit cell of  $Ba_8Ga_{16}Ge_{30}$  [35]. Table 3.11 also reveals that the atomic displacement parameters of Ba2 at different concentration of Ga show a similar feature.

Table 3. 11 Selected crystallographic information for  $Ba_8Al_{16}Ga_xGe_{30}$  obtained from Rietveld refinement of neutron powder diffraction data. The atomic coordinates in the refinements: Ba1 2a (0,0,0), Ba2 6d (1/4,1/2,0) or 24k (x,1/2,z), Al1/Ge1 6c (1/4,0,1/2), Al2/Ge2 16i (x, x, x), and Al3/Ge3 24k (0,y,z).

RT	$x = 0$		$x = 2$		$x = 4$		$x = 6$		$x = 8$	
unit cell (Å)	10.848101(5)		10.842484(4)		10.834031(4)		10.827042(4)		10.818767(4)	
model	6d	24k								
$U_{iso}$ (Ba1) (Å <sup>2</sup> )	0.0072(5)	0.0099(4)	0.0087(3)	0.0100(3)	0.0081(4)	0.0094(4)	0.0078(3)	0.0089(4)	0.0094(4)	0.0101(4)
$U_{iso}$ (Ba2) (Å <sup>2</sup> )	0.0346(5)	0.0150(8)	0.0355(3)	0.0154(6)	0.0336(3)	0.0136(6)	0.0348(3)	0.0161(7)	0.0347(3)	0.0181(10)
$x$ (Ba2)	0.25	0.2472(8)	0.25	0.2478(6)	0.25	0.2481(7)	0.25	0.2475(7)	0.25	0.2439(7)
$z$ (Ba2)	0	0.0213(4)	0	0.0218(3)	0	0.0218(3)	0	0.0211(3)	0	0.0191(4)
$U_{11}$ (Ba2) (Å <sup>2</sup> )	0.0168(7)		0.0165(5)		0.0148(6)		0.0174(6)		0.0239(7)	
$U_{22}$ (Ba2) (Å <sup>2</sup> )	0.0444(6)		0.0465(4)		0.0445(5)		0.0449(5)		0.0408(5)	
$U_{iso}$ (host) (Å <sup>2</sup> )	0.00773(6)	0.00875(8)	0.00818(5)	0.00794(5)	0.00767(5)	0.00754(5)	0.00762(6)	0.00748(5)	0.00906(6)	0.00901(6)
$x$ (Ge2)	0.18434(3)	0.18443(3)	0.18442(2)	0.18447(2)	0.18447(2)	0.18452(2)	0.18445(2)	0.18449(2)	0.18447(2)	0.18450(2)
$y$ (Ge3)	0.30820(4)	0.30831(4)	0.30830(3)	0.30832(3)	0.30816(3)	0.30818(3)	0.30816(3)	0.30817(3)	0.30836(3)	0.30835(3)
$z$ (Ge3)	0.11691(4)	0.11689(4)	0.11693(3)	0.11684(3)	0.11706(3)	0.11697(3)	0.11722(3)	0.11715(3)	0.11742(3)	0.11736(3)
$\chi^2$	1.538	1.532	3.72	3.71	3.99	3.97	2.71	2.70	2.68	2.68
$R_{wp}$ , $R_F$ (%)	3.86, 6.66	3.85, 6.52	6.26, 3.37	6.26, 3.30	6.84, 3.54	6.82, 3.42	5.41, 2.88	5.40, 2.83	6.59, 3.38	6.58, 3.32

The site occupancies highly depend on the synthesis conditions [53]. However, the similarity of the site occupancies has been observed for the different synthesis methods. Table 3.12 shows the comparison of site occupancies of aluminum to the reference for  $Ba_8Al_{16}Ge_{30}$  sample. The site occupancies of the present study have the similarity to the single crystal  $Ba_8Al_{16}Ge_{30}$  grown by stoichiometric mixing; 67 % of the 6*c* site is occupied by aluminum, while around 70 % of the 16*i* and 24*k* sites by germanium.

Table 3. 12 Site occupancies of aluminum for  $Ba_8Al_{16}Ge_{30}$

$Ba_8Al_{16}Ge_{30}$	Polycrystalline	Single Crystal	Single Crystal
	Arc melting (Present study)	Stoichiometric [53]	Czochralski [53]
6 <i>c</i> (Al)%	67.2(5)	67(1)	96(1)
16 <i>i</i> (Al)%	32.0(5)	31(1)	43(1)
24 <i>k</i> (Al)%	28.5(5)	27(1)	9(1)
6 <i>c</i> + 24 <i>k</i> (Al)%	95.7(7)	94(1)	105(1)
16 <i>i</i> + 24 <i>k</i> (Al)%	60.5(7)	58(1)	52(1)
Al atoms	15.992(9)	15.5(2)	14.8(2)
Ge atoms	30.008(9)	30.5(2)	31.2(2)

Figure 3.13 shows *x* dependences of lattice constant, Ga, Al, and Ge occupancy based on the Rietveld refinement of neutron data. Aluminum occupancies at three distinct sites decrease with increasing the Ga concentration which is dominantly occupied the 6*c* site. There are two kinds of Ga site preferences. For 6*c* site, the Ga occupancies at *x* = 2 and 4 are small while at *x* = 6 and 8, they are as large as 18%, shown in Figure. For 16*i* and 24*k*, the Ga occupancies gradually increase with increasing the Ga content. As for the Ge site preferences, those samples show similar site preferences with the sample  $Ba_8Al_{16}Ge_{30}$  grown by stoichiometric mixing [53]; Ge is occupied approximately 30% at 6*c* site and dominantly occupied the 16*i* and 24*k* site for about 70%.

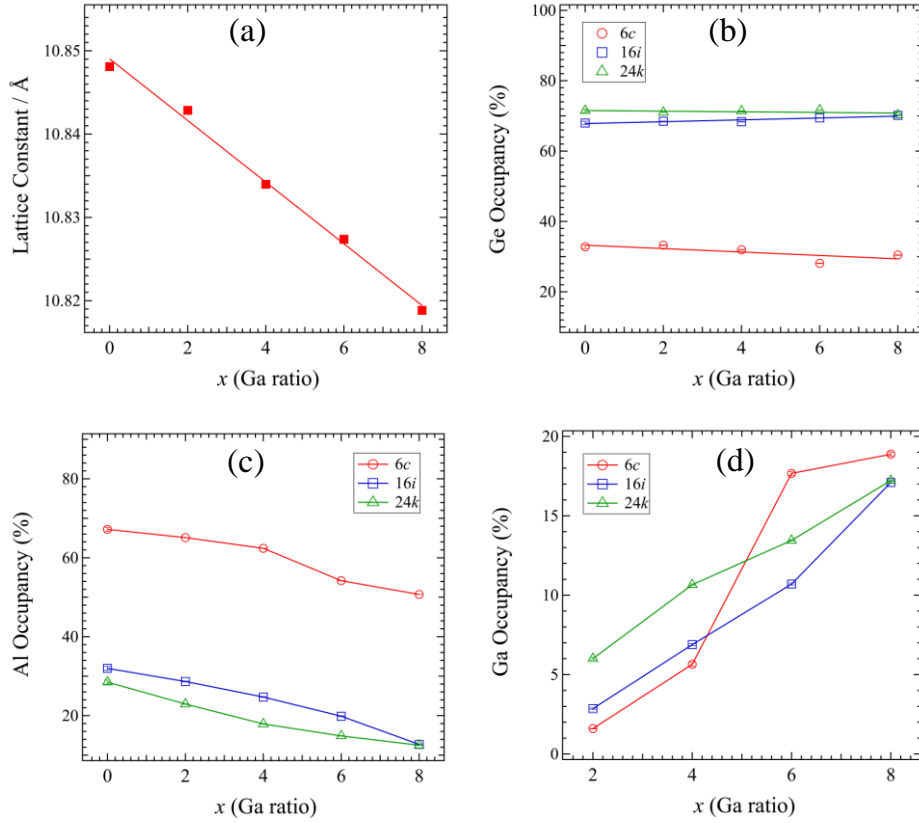


Figure 3.13 The  $x$  dependences of (a) lattice constant, (b), (c), and (d) Ga, Al, and Ge occupancy from Rietveld refinement at room temperature. The red circle, blue square, green triangle pointing up correspond to the  $6c$ ,  $16i$ , and  $24k$  site, respectively.

Initially, the host atoms were assumed to be distributed randomly toward the three different sites of host atoms. Then, Christensen *et al.* [37] deduced a guideline for site occupancies, which is analogue to the Loewenstein rule [87]. This guideline is based on the fact direct bonding between trivalent elements, *e.g.* Al and Ga, are energetically unfavorable [88]. The guideline consists of five rules: 1)  $6c \leq 100\%$ ; 2)  $16i \leq 50\%$ ; 3)  $24k \leq 50\%$ ; 4)  $6c+24k \leq 100\%$ ; and 5)  $16i + 24k \leq 50\%$ . As shown in Table 3.3 and Table 3.4, the five samples are in good agreement with the rule 1 to 4 whereas the rule 5 has a large deviation about 10%. In contrast, for the single crystal grown by the Czochralski method (Table 3.14), the  $6c$  and  $24k$  are almost fully occupied by aluminum and germanium, respectively; the 1st to the 3th rules hold whereas small deviations from the 4th and 5th rules.

Table 3. 13 Site occupancies of Aluminum and Gallium for  $Ba_8Al_{16-x}Ga_xGe_{30}$

	$x = 2$		$x = 4$		$x = 6$		$x = 8$	
	Al	Ga	Al	Ga	Al	Ga	Al	Ga
6c (%)	65.10(19)	1.64(10)	62.39(21)	5.65(12)	54.22(21)	17.67(12)	50.7(2)	18.88(13)
16i (%)	28.66(10)	2.86(5)	24.74(11)	6.89(6)	19.86(10)	10.70(6)	12.73(12)	17.10(6)
24k (%)	22.95(7)	6.01(7)	17.91(7)	10.66(4)	14.87(7)	13.45(4)	12.52(8)	17.22(4)
6c +24k (%)	95.6(3)		96.6(2)		100.2(2)		99.3(2)	
16i +24k (%)	60.48(15)		60.2(1)		58.9(1)		59.5(2)	

The refinement results using the  $6d$  and  $24k$  model for  $Ba_8Al_{16}Ge_{30}$  and  $Ba_8Al_8Ga_8Ge_{30}$  are shown in Figure 3.14. The results reveal an expansion of lattice parameter with increasing the temperature. The expansion for both samples reaches as large as  $0.1 \text{ \AA}$  (Figure 3.14a) from 10 K to 900 K. For the  $6d$  model (Figure 3.14b and 3.14d), the anisotropic displacement parameters (ADPs) was refined for Ba2; large anisotropic values are obtained for  $U_{22} (=U_{33})$ . As a result, a pancake-like shape of Ba2 is obtained (Figure 3.3a). On the contrary, the ADPs of host atoms were refined to be small and Ba1 are found to be almost similar. A similar tendency of Ba2 guest atoms also observed from the refinement result of  $24k$  model (Figure 3.14c and 3.14e). The APDs of  $U_{22}$  and  $U_{33}$  at the highest temperature point are 3.97 times larger than those at 10 K for sample with  $x = 0$ . Slightly different result, 3.84 times larger, is obtained for sample with  $x = 8$ . Whereas, for host atoms and Ba1, the ADPs of both samples are approximately only two times larger. Ba2 guest atoms are observed to be shifted further from the center position by increasing the temperature as can be seen from Figure 3.5f, where the size of the displacements was determined by calculating the half distance of the opposing Ba2 atoms. The off-centered displacement of  $x = 0$  and  $x = 8$  are same for the temperature range 10 to 200 K. However, from room temperature to the highest temperature, the Ba2 guest atoms of  $x = 8$  shift in smaller distance compared to the  $x = 0$ . The lattice size corresponds to the cage size. Thus, we assume that the smaller lattice of  $x = 8$  can be one of the reasons for the smaller shifted value.

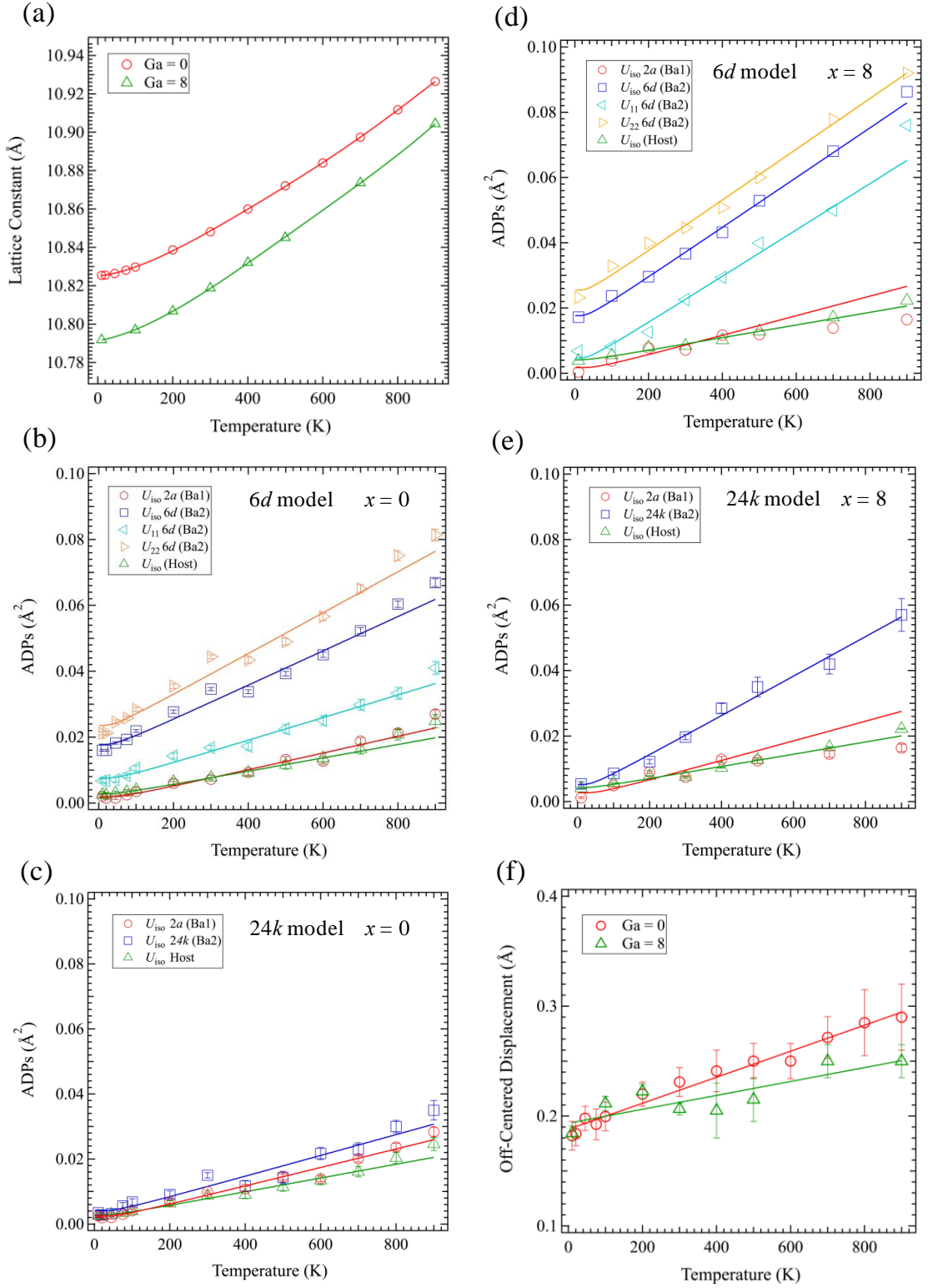


Figure 3. 14 The temperature dependences of (a) lattice constant, (b), (c), (d), (e), atomic displacement parameters (ADPs) from 6d and 24k model, and (f) off-centered displacement parameters for sample with  $x = 0$  and  $x = 8$ .

# Chapter 4

## Maximum Entropy Method

### 4.1 Maximum Entropy Method (MEM)

The maximum entropy method (MEM) has been known as a powerful method for a model-free image reconstruction in many fields of science [89]. MEM was firstly used in the radio-astronomical interferometry by Gull and Danielli in 1978 [90]. In the case of crystallography, MEM is used to determine the electron and nuclear density distribution to study such as the structural disorder and the diffusion pathways in ionic conductor material [91-94]. The diffraction data is commonly analyzed in reciprocal space using the least-squares fitting to a structure factor model which contain the information of atomic thermal motion. Another approach to analyze the thermal motion can be done in direct space by MEM. From X-ray diffraction data, MEM generates the thermally smeared electron density distribution in direct space [95, 96]. From neutron diffraction data, MEM produce the information of direct space nuclear density distribution which corresponds to the point nuclei distribution smeared by the atomic thermal motion [97,98].

The combination of MEM and Rietveld analysis, so-called the REMEDY cycle, was proposed by Takata et al. in 1995, in which the calculated structure factor obtained from Rietveld refinement ( $F_{cal}$ ) being replace by the one that is obtained from MEM calculations ( $F_{MEM}$ ) [99]. The basic principle of MEM is that the optimum image is the one that is consistent with the data and maximum value of the entropy functional  $S$ . For our purpose, the image is the nuclear density  $\rho$  in the unit cell, with number divided pixel in a unit cell  $N_p = N_1 \times N_2 \times N_3$  and the entropy is defined as [100-102]

$$S = - \sum_{i=1}^{N_p} \rho_i \log(\rho_i/\tau_i) \quad (4. 1)$$

Where  $\tau_i$  mean the prior of reference nuclear density distribution.

The constraint maximizing the entropy  $S$  should be selected to obtain the nuclear density distribution. In crystallography, the electron or nuclear density satisfies two conditions [103]:

$$\sum_i \rho_i = 1 \quad (4. 2)$$

$$C_F = \frac{1}{N_F} \sum_{j=1}^{N_F} \left[ \frac{F_{obs}(\mathbf{h}_j) - F_{MEM}(\mathbf{h}_j)}{\sigma(\mathbf{h}_j)} \right]^2 < 1 \quad (4. 3)$$

The Eq. 4.2 corresponds to the conservation of total density distribution during the calculation processes. The equation 4.3, the so-called  $F$ -constraint  $C_F$ , means the calculated structure factors obtained from MEM analysis  $F_{MEM}(\mathbf{h})$  converge to the observed structure factors from the diffraction data  $F_{obs}(\mathbf{h})$  within standard deviation  $\sigma(\mathbf{h})$ .  $N_F$  is the number of observed structure factors. Using the method of undetermined Lagrange multiplier [104]

$$Q(\rho_i) = S(\rho_i) - \lambda_F C_F(\rho_i) \quad (4. 4)$$

where the  $\lambda_F$  is the Lagrange multiplier. Differentiating the Eq. 4.4 with respect to  $\rho_i$  yields

$$\frac{\partial Q}{\partial \rho_i} = \frac{\partial S}{\partial \rho_i} - \lambda_F \frac{\partial C_F}{\partial \rho_i} \quad (4. 5)$$

Combining the Eq. 4.1 for substitution the entropy  $S$  and Eq. 4.5 to obtain

$$\frac{\partial Q}{\partial \rho_i} = -1 - \log\left(\frac{\rho_i}{\tau_i}\right) - \lambda_F \frac{\partial C_F}{\partial \rho_i} = 0 \quad (4. 6)$$

The above equation can be rewritten as follow [103]

$$\rho_i = \tau_i \exp\left(-\lambda_F \frac{\partial C_F}{\partial \rho_i}\right) \quad (4. 7)$$

The structure factors  $F_{MEM}$  and the density distribution  $\rho$  are related by Fourier transformation [103,104]

$$F_{MEM}(\mathbf{h}) = V \sum_{k=1}^N \rho(\mathbf{x}_k) \exp(2\pi i \mathbf{h} \cdot \mathbf{x}_k) \quad (4. 8)$$

where  $V$  is the volume of unit cell. In particular, the structure factors of neutron diffraction data are defined as

$$F_{MEM}(\mathbf{h}) = \sum_{j=1}^N b \exp(2\pi i \mathbf{h} \cdot \mathbf{x}_j) T_j(\mathbf{h}) \quad (4. 9)$$

with  $b$  and  $T_j$  are the atomic scattering length and thermal motion parameter, respectively.

## 4.2 Results and Discussion

Although the  $24k$  model gave slightly lower R-factors than those of  $6d$  model, it is difficult to conclude whether  $24k$  or  $6d$  as the best model only from these refinement results. An additional analysis is necessary to determine the suitable model to explain the disorder phenomena of Ba2 guest atom. Thus, Maximum Entropy Method (MEM) calculations were carried out to investigate the nuclear density distribution of Ba2 atom; neutron diffraction data provides the information about the density distribution of the nuclear scattering amplitudes because the interaction occurred between neutron and nucleus of material during scattering process. The MEM calculation was performed for sample  $\text{Ba}_8\text{Al}_{16}\text{Ge}_{30}$  and  $\text{Ba}_8\text{Al}_8\text{Ga}_8\text{Ge}_{30}$ .

### 4.2.1 Results of $\text{Ba}_8\text{Al}_{16}\text{Ge}_{30}$ ( $\text{Ga} = 0$ )

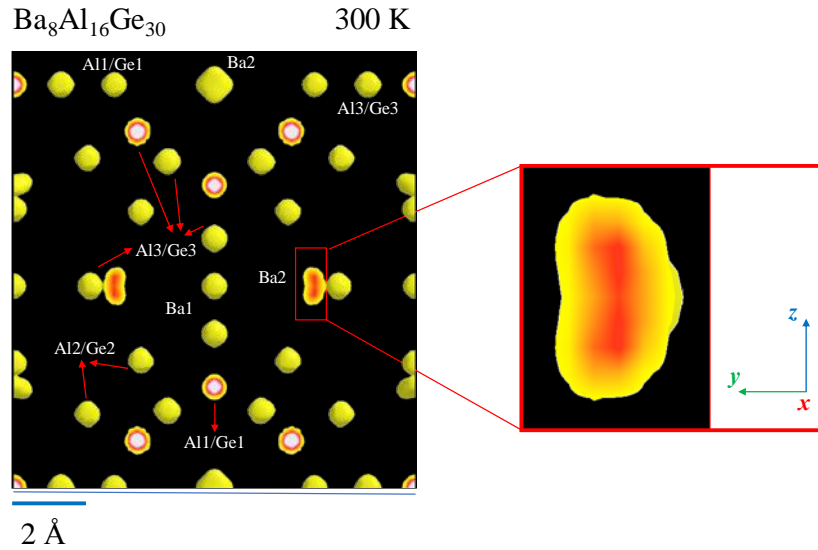


Figure 4.1 Scattering amplitude density distribution of unit cell  $\text{Ba}_8\text{Al}_{16}\text{Ge}_{30}$  obtained from MEM with isosurface level at  $3.0 \text{ fn}/\text{\AA}^3$ . The magnified figure is Ba2 guest atom. The  $x$ ,  $y$ , and  $z$  are defined as the local axis for the magnified Ba2 atom.

Figure 4.1 shows the density distribution map of the nuclear scattering amplitudes in  $\text{Ba}_8\text{Al}_{16}\text{Ge}_{30}$  obtained by MEM calculation for neutron diffraction data measured at 300 K. The MEM results clearly show that the Ba2 guest atom is located at an off center  $24k$  site which agrees better with the  $24k$  model than the  $6d$  model. It is also in good agreement to the difference Fourier summation result of Ba2 for single crystal sample grown by stoichiometric mixing than that grown by the Czochralski method [53]. Since, as shown by Table 3.12, the Czochralski sample has different distribution of site occupancies, the similarity of site occupancies leads to the similarity of guest atom features. This confirms that the host structure correlates to the guest atom distribution, and host structure has a role in controlling the guest atom features.

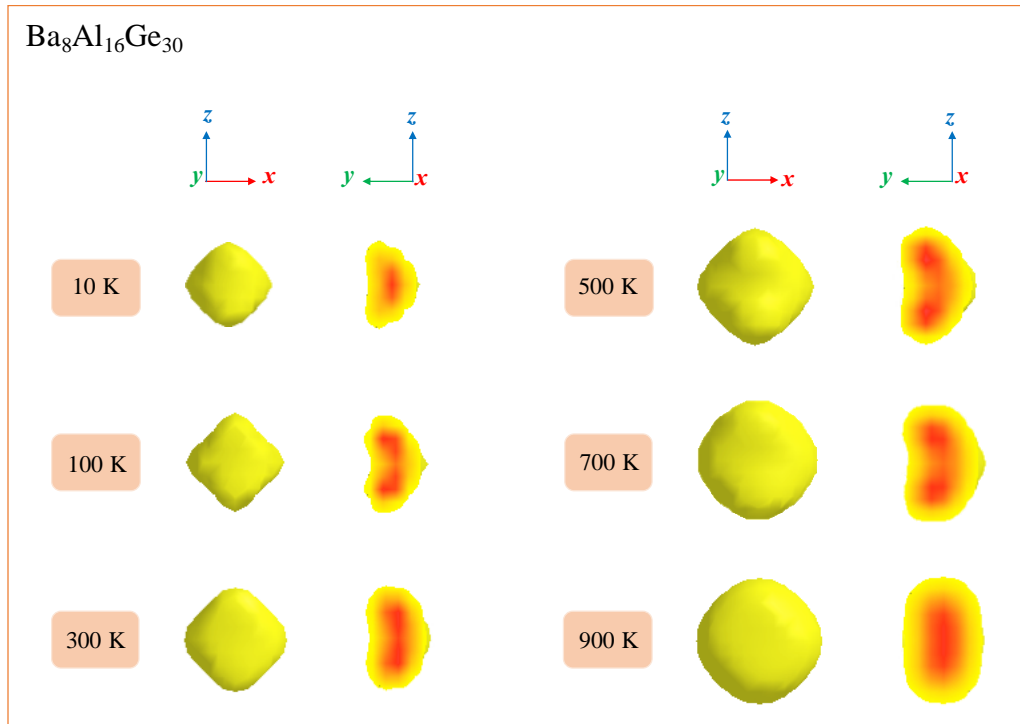


Figure 4. 2 The selected density distribution of Ba2 guest atom  $Ba_8Al_{16}Ge_{30}$ . The  $x$ ,  $y$ , and  $z$  are defined as the local axis for the Ba2 atom. To the right, the density distribution parallel to the  $y$  axis and half-cut parallel to  $x$  axis.

The variation of the Ba2 distribution on increasing temperature is shown in Figure 4.2. Ba2 atoms distribute at the  $24k$  site between 10 to 500 K. At higher temperature, the Ba distribution becomes wider, and at 900 K, it becomes isotropic in the  $xz$  plane. On the other hand, in the  $n$ - and  $p$ -type  $Ba_8Ga_{16}Ge_{30}$ , the Ba2 distribution changes from the  $24j$  to the  $24k$  as the temperature increase from 15 to 300 K [35].

## 4.2.2 Results of $\text{Ba}_8\text{Al}_8\text{Ga}_8\text{Ge}_{30}$ ( $\text{Ga} = 8$ )

The MEM result of  $\text{Ba}_8\text{Al}_8\text{Ga}_8\text{Ge}_{30}$  for neutron diffraction data measured at 300 K, given by Figure 4.3, shows the same behavior of Ba2 guest atoms as observed for  $\text{Ba}_8\text{Al}_{16}\text{Ge}_{30}$ ; the  $24k$  model is in a good agreement with the MEM results of  $\text{Ba}_8\text{Al}_8\text{Ga}_8\text{Ge}_{30}$ . This also revealed that there is no any significant effect of the aluminum substitution by gallium at room temperature. A clear effect of the substitution is observed at higher temperature as shown by the Figure 4.4. It is also revealed by Figure 4.4 that the density distribution size of Ba2 becomes larger as temperature increases. However, the shape of Ba2 density distributions are different from that of  $\text{Ba}_8\text{Al}_{16}\text{Ge}_{30}$  at the temperature range of 500 to 900 K. The position of Ba2 guest atom is remained at the  $24k$  site. Those distributions only grow bigger parallel to the  $y$  direction with increasing temperature, while the  $xz$  planes size are observed to be no different significantly. The role of the difference feature of nuclear density distribution will be further discussed in the Chapter 6.

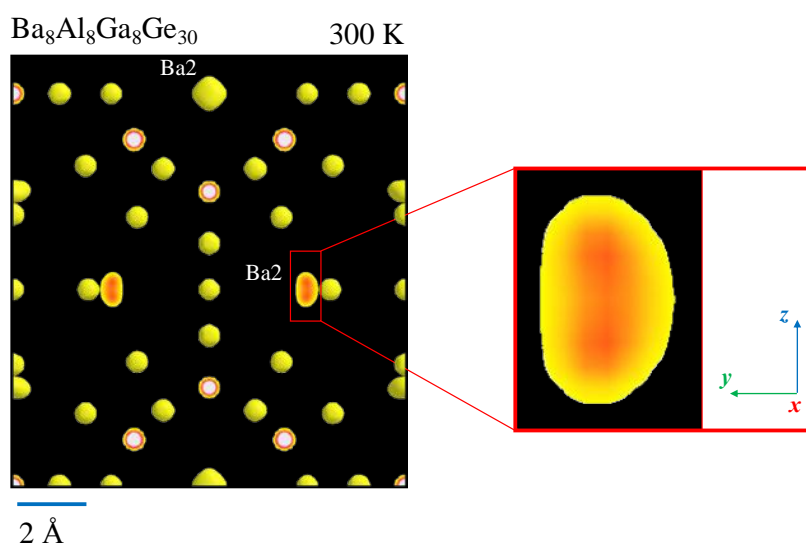


Figure 4. 3 The nuclear density distribution of unit cell  $\text{Ba}_8\text{Al}_8\text{Ga}_8\text{Ge}_{30}$  obtained from MEM with isosurface level at  $4.3 \text{ fm}/\text{\AA}^3$ . The  $x$ ,  $y$ , and  $z$  are defined as the local axis for the magnified Ba2 atom.

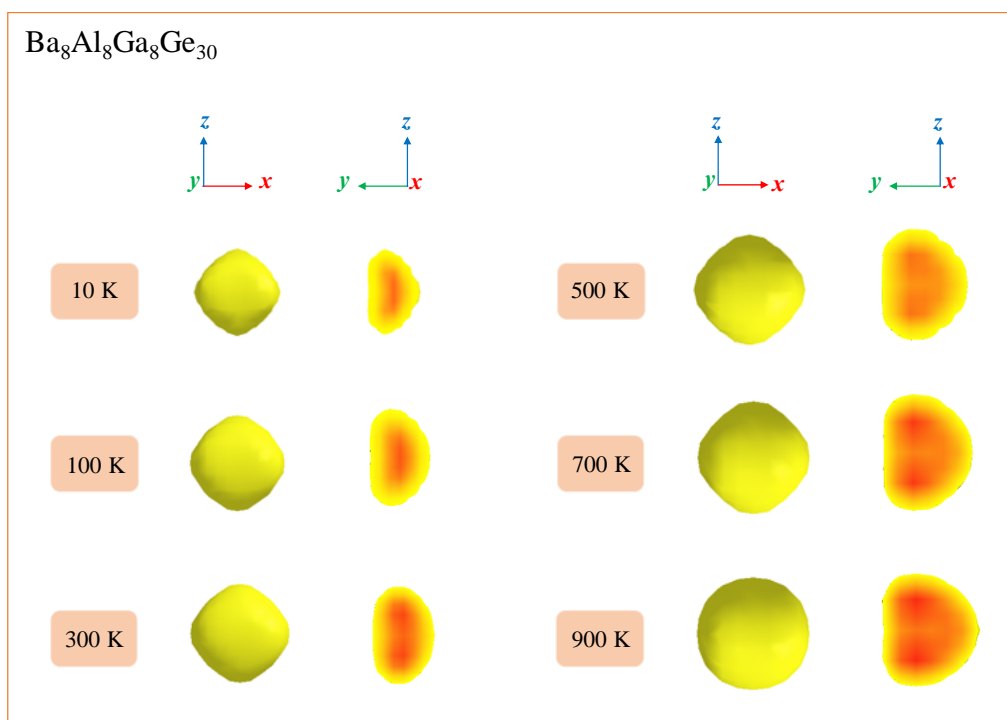


Figure 4. 4 The evolution of Ba2 density distribution  $Ba_8Al_8Ga_8Ge_{30}$ . The  $x$ ,  $y$ , and  $z$  are defined as the local axis for the Ba2 atom. First and the second row are the density distribution parallel to the  $y$  axis and half cut parallel to  $x$  axis, respectively.

# Chapter 5

## Thermoelectric Properties

### 5.1 Seebeck Coefficient

Seebeck coefficient can be defined as the heat per carrier over temperature or entropy per carrier which is expressed in the following equation [107]

$$S = \frac{C_{el}}{q} \quad (5.1)$$

where  $C_{el}$  is the electronic specific heat and  $q$  is the carrier charge. In the case of classical gas, the energy of each electron is  $\frac{3}{2}k_B T$ , where  $k_B$  is the Boltzmann constant ( $1.38 \times 10^{-23}$  J/K). The electronic heat capacity  $C_{el}$  for metals and degenerated semiconductor by free electron model is defined as the derivative of total electronic thermal kinetic energy over temperature,  $\frac{\partial U_{el}}{\partial T}$ . Then, the Seebeck coefficient  $S$  of classical electron gas is approximately  $\frac{k_B}{e} \approx 87 \mu\text{V/K}$ , where  $e$  is the constant number of electron charge. For metals and degenerated semiconductors, only electrons with energy level  $k_B T$  of Fermi energy  $E_F$  can be thermally excited at temperature  $T$  and contribute to Seebeck coefficient. Accordingly, the electronic specific heat can be derived as follows [108]

$$C_{el} = \frac{\partial U_{el}}{\partial T} = \frac{\partial \left( N \frac{T}{T_F} \right) k_B T}{\partial T} = \left( N \frac{T}{T_F} \right) k_B = N \frac{k_B^2 T}{E_F} \quad (5.2)$$

Where  $N$  is the number of electrons and  $T_F$  is the Fermi temperature. With  $E_F = k_B T_F$ , the Seebeck coefficient is given by [109]

$$S \approx \frac{1}{e} \frac{k_B^2 T}{E_F} \approx \left(\frac{k_B}{e}\right) \left(\frac{k_B T}{E_F}\right) \quad (5.3)$$

In metals, the value of Seebeck coefficient is much lower than  $87\mu\text{V/K}$  (on the order of  $1\text{-}10\mu\text{V/K}$ ) and decreases as temperature decreases. In contrast, the Seebeck coefficient of semiconductors is much higher than the  $87\mu\text{V/K}$ . The Seebeck coefficient for metal is described by Mott equation

$$S_D = \frac{\pi^2 k_B^2 T}{3e} \left[ \frac{1}{\sigma(E)} \frac{d\sigma}{dE} \right]_{E=E_F} \quad (5.4)$$

For semiconductor, only electron with energy level across an energy gap  $E_G$  can be thermally excited. Thus, the Seebeck coefficient is approximated by

$$S = \left(\frac{k_B}{e}\right) \left(\frac{E_G}{k_B T}\right) \quad (5.5)$$

The relationship between Seebeck coefficient and carrier concentration  $n$  is given by [58]

$$S = \frac{8\pi^2 k_B^2}{3eh^2} m^* T \left(\frac{\pi}{3n}\right)^{2/3} \quad (5.6)$$

where  $m^*$  is the effective mass of the carrier and  $h$  is the Planck constant. Low carrier concentration results in large Seebeck coefficient. The typical values of Seebeck coefficient to obtain high  $ZT$  are on the order of  $150\text{-}250\mu\text{V/K}$ .

## 5.2 Electrical Conductivity

The electrical resistivity is defined as the constant ratio between the electric field  $\mathbf{E}$  and current density  $\mathbf{j}$ , expressed in the form [2]

$$\mathbf{E} = \rho \mathbf{j} \quad (5.7)$$

The current density is given by  $\mathbf{j} = -|e|n\mathbf{v}$ , where  $\mathbf{v}$  is the average velocity of the electrons. Without electric field  $\mathbf{E}$ , electrons in metal are always moving in random

direction with different energies resulting  $\mathbf{j} = 0$ . By applying the electric field  $\mathbf{E}$ , the average velocity of electron has preferential direction of motion and can be expressed in the form

$$\mathbf{v} = -\frac{|e|\tau}{m^*}\mathbf{E} \quad (5.8)$$

where  $\tau$  is the relaxation time which corresponds to the average collision time of electrons.

$$\mathbf{j} = \frac{e^2 n \tau}{m^*} \mathbf{E} = -\frac{e^2 n \tau}{m^*} \nabla V \quad (5.9)$$

According to the Ohm's law,  $\mathbf{j} = -\sigma \nabla V$ , the electrical conductivity is expressed in the form

$$\sigma = \frac{e^2 n \tau}{m^*} = n e \mu \quad (5.10)$$

where  $\mu$  is the mobility of electrons. The Eqs. 5.6 and 5.10 show the opposite roles of carrier concentration. High concentration of carrier is necessary to obtain high electrical conductivity. However, it will affect to decrease the Seebeck coefficient. Similar behavior for effective mass. Smaller effective will increase the electrical conductivity and at the same time it will reduce the Seebeck coefficient. The typical values of the electrical conductivity for obtaining high  $ZT$  are on the order of  $10^3 (\Omega \cdot \text{cm})^{-1}$ .

### 5.3 Thermal Conductivity

The thermal conductivity is defined as the thermal transfer in materials through the electrons and phonons. Therefore, the total contribution of thermal conductivity arises from the charge carrier motion  $\kappa_e$  and atomic vibration of lattice  $\kappa_l$ . [2, 57]

$$k = \kappa_e + \kappa_l \quad (5.11)$$

The electronic thermal conductivity is expressed in the form

$$\kappa_e = \frac{1}{3} C_{el} v_F l_e = \frac{\pi^2 n k_B^2 T \tau}{3 m^*} \quad (5.12)$$

where  $l_e$  is the mean free path of electrons and  $v_F$  is the Fermi velocity. Using the Eq. 5.10, the above equation can rewrite as

$$\kappa_e = \frac{\pi^2}{3} \left( \frac{k_B^2}{e} \right)^2 \sigma T = L_0 \sigma T \quad (5.13)$$

where  $L_0 = 2.44 \times 10^{-8} \text{ V}^2/\text{K}^2$  is the Lorenz number for free electron model. The electronic thermal conductivity  $\kappa_e$  is related to the electrical conductivity through the so-called Wiedemann-Franz's law (Eq. 5.13). In metals, the charge carriers behave like free electrons. The Lorenz number can vary with carrier concentration. For semiconductors, the Lorenz number converges to  $1.48 \times 10^{-8} \text{ V}^2/\text{K}^2$ . The decreasing of Lorenz number is correlated with an increase in Seebeck coefficient. Accordingly, approximation of Lorenz number related to the Seebeck coefficient is expressed in the form [110]

$$L = 1.5 + \exp\left(-\frac{|S|}{116}\right) \quad (5.14)$$

where  $L$  is in  $10^{-8} \text{ V}^2/\text{K}^2$  and  $S$  is in  $\mu\text{V}/\text{K}$ . The use of this equation instead of the constant number of  $L$  will improve the estimation of lattice thermal conductivity  $\kappa_l$  from experimental results.

Using the classical model by Debye [111], the lattice thermal conductivity is expressed as

$$\kappa_l = \frac{1}{3} C_v v l_l \quad (5.15)$$

where  $C_v$ ,  $v$ ,  $l_l$ , are the specific heat per unit volume, sound velocity of materials, phonon mean free path ( $l = v\tau$ ). Phonon mean free path corresponds to the length of phonons scattered by collision between phonons themselves or by lattices imperfections,

such as dislocations and grain boundaries. For the experimental results, the lattice thermal

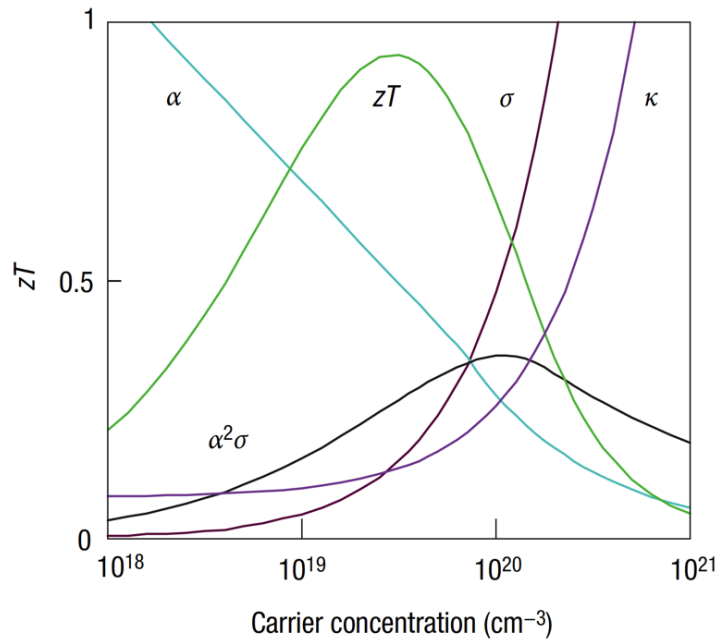


Figure 5. 1 Illustration of the relationship between the thermoelectric properties and carrier concentration [58].

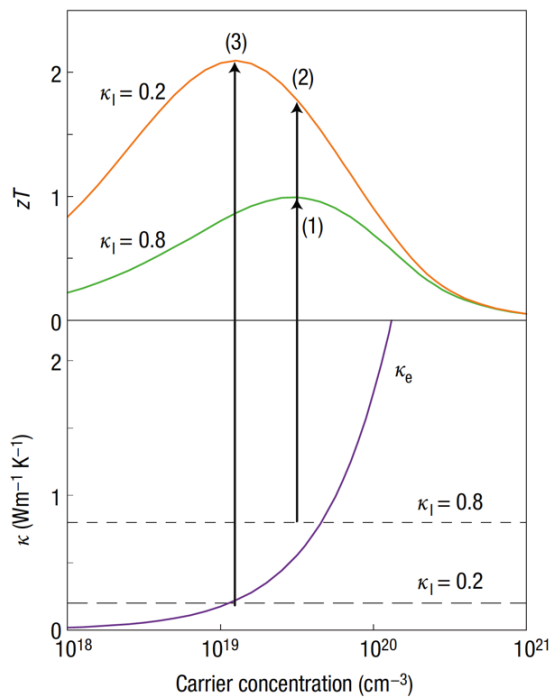


Figure 5. 2 Illustration of the benefit lowering the lattice thermal conductivity to improve Figure of merit zT [58].

conductivity is obtained by subtracting the total thermal conductivity with the electronic contribution [58]. Low lattice thermal conductivity is necessary for the benefit of  $ZT$  as illustrated in Figure 5.2. The relationship between the thermoelectric properties and carrier concentration is illustrated in Figure 5.1.

## 5.4 Experimental Details of Transport Measurement

### 5.4.1 Low-Temperature Measurement

The button shape ingots obtained from arc melting method were cut into rectangular shape using the Wire Electric Discharge Machine (EDM). This machine, as shown in Figure 5.3, uses a high voltage electrical discharge phenomenon to cut metal. The voltage difference between a wire and conductive workpiece generates sparks which use to cut the object [112]. The cutting process is done in the dielectric fluid environment. A good precision in cutting size can be achieved from this machine because of a thin wire of 0.02 mm in diameter is used. The samples were cut approximately 10 – 14 mm in length, 2 – 3 mm in width, and 2 – 3 mm in height, as shown in Figure 5.4.



Figure 5. 3 Wire Electric Discharge Machine (EDM)

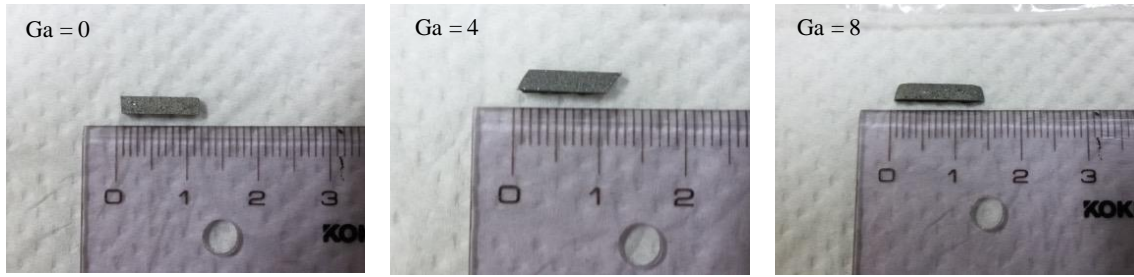


Figure 5. 4 The cutting results using Wire EDM for samples with  $Ga = 0, 4,$  and  $8.$

Measurement of thermoelectric properties at low temperature to room temperature were performed using the Physical Properties Measurement System (PPMS), thermal transport option (TTO), see Figure 5.5. The TTO system measures the thermal conductivity, electrical resistivity, and Seebeck coefficient. Then, based on the measurements data, the Figure of merit also calculated by the program. The arc melting ingots were cut to form rectangular shape and then installed to the TTO puck after attaching the coppers as connector (see Figure 5.6). The samples are approximately 10 – 14 mm in length, 2 – 3 mm in width, and 2 – 3 mm in height. The copper connectors were attached using the silver paste for the purpose of providing a good thermal contact between the coppers and sample.

Thermal conductivity is measured by applying heat from the heater shoe to produce temperature difference  $\Delta T$  at hot thermometer and cold thermometer probes. The heat is transferred to the environment through the heat sink. Thermal conductivity is determined from the following equation [113]

$$\kappa = K \frac{h}{A} \quad (5. 16)$$

where  $K$  is the thermal conductance,  $h$  is the sample length, and  $A$  is the cross section of sample. The Seebeck voltage  $\Delta V$  are measured during the heat pulse, where Seebeck coefficient is obtained from determining the ratio of  $\Delta V$  over  $\Delta T$ ,  $S = \frac{\Delta V}{\Delta T}$ . The electrical resistivity is measured before and after the heat pulse by measuring the current  $I$  flows through the sample and the voltage drop  $V$  across the sample. [113] The electrical resistivity  $\rho$  is given by [114]

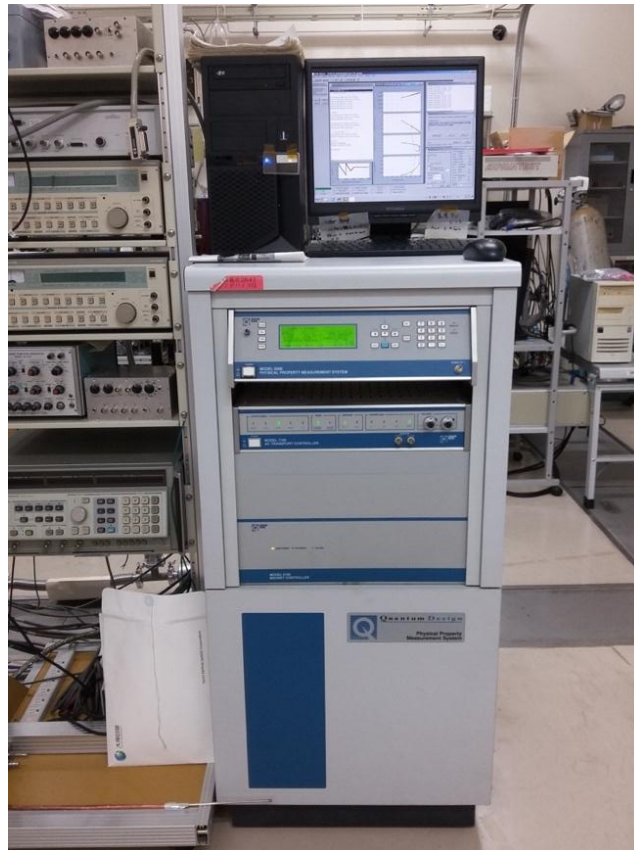
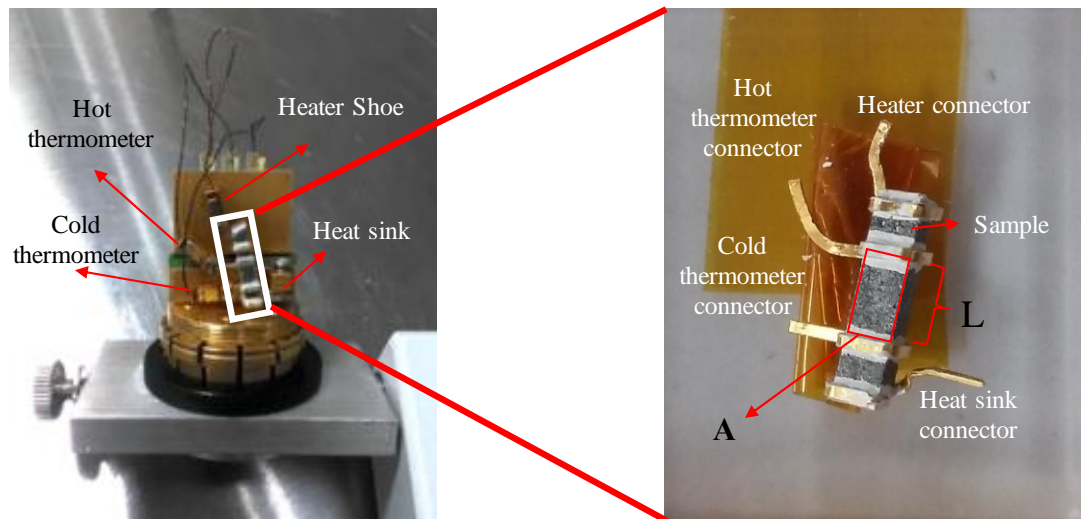


Figure 5. 5 Physical Properties Measurement System (PPMS) instrument



Connector : copper flat

Figure 5. 6 Thermal Transport Option (TTO) puck with a 10.82 mm in length  $Ba_8Al_{16}Ge_{30}$  sample.

$$\rho = \left(\frac{V}{l}\right) \left(\frac{A}{L}\right) = R \left(\frac{A}{L}\right) \quad (5.17)$$

where  $L$  is the distance between probes (See Figure 5.6).

### 5.4.2 High-Temperature Measurement

A strong compact sample is necessary for high temperature measurement. While the ingot obtained from arc melting method is quite brittle. Therefore, an additional heating treatment, SPS, was performed. The SPS method has the ability to produce sample with high density percentage. As can be seen from Table 5.1, the samples densities are higher than 90%. The samples densities were determined using the density determination kit of METTLER TOLEDO balance, as shown below.



Figure 5. 7 The density determination kit of METTLER TOLEDO balance. [116]

The samples were weighed on the air environment and then in the water. The density  $\rho$  can be determined using the following equation [115]

$$\rho = \frac{W_a}{W_a W_l} (\rho_0 - \rho_l) + \rho_l \quad (5.17)$$

where  $W_a$  and  $W_l$  are weight of sample in air and water, respectively. The  $\rho_a$  and  $\rho_l$  are the density of air ( $0.0012 \text{ g/cm}^3$ ) and liquid, respectively. For the accuracy of measurement, the water temperature is considered to determine the water density. The results of density measurement are shown in Table 5.1.

Table 5. 1 Density of samples with  $Ga = 0, 4, \text{ and } 8$ .

Sample	Density (measurement)	Density (calculation)	Density percentage (%)
Ga = 0	4.7656 $\text{gr/cm}^3$	4.8256 $\text{gr/cm}^3$	98.75
Ga = 4	5.0122 $\text{gr/cm}^3$	5.0659 $\text{gr/cm}^3$	98.94
Ga = 8	4.9572 $\text{gr/cm}^3$	5.3059 $\text{gr/cm}^3$	93.42

The compact samples in disc shape were first used to measure the thermal conductivity. After finishing the thermal transport properties measurement, those samples were cut into rectangular shape to do the electrical transport measurements. The cutting process was done using the wire saw machine. The cutting results are shown in the figure below.

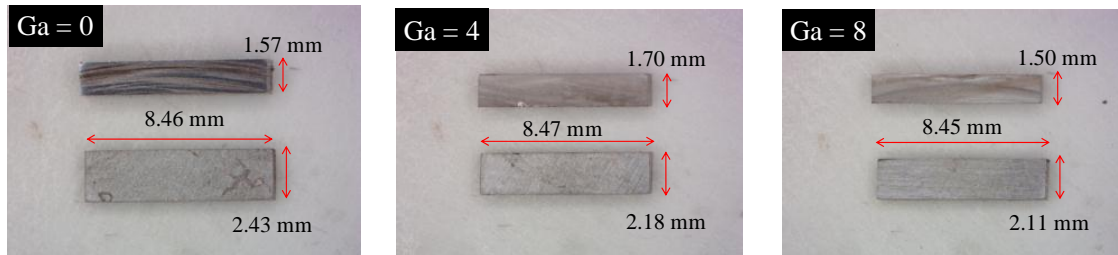
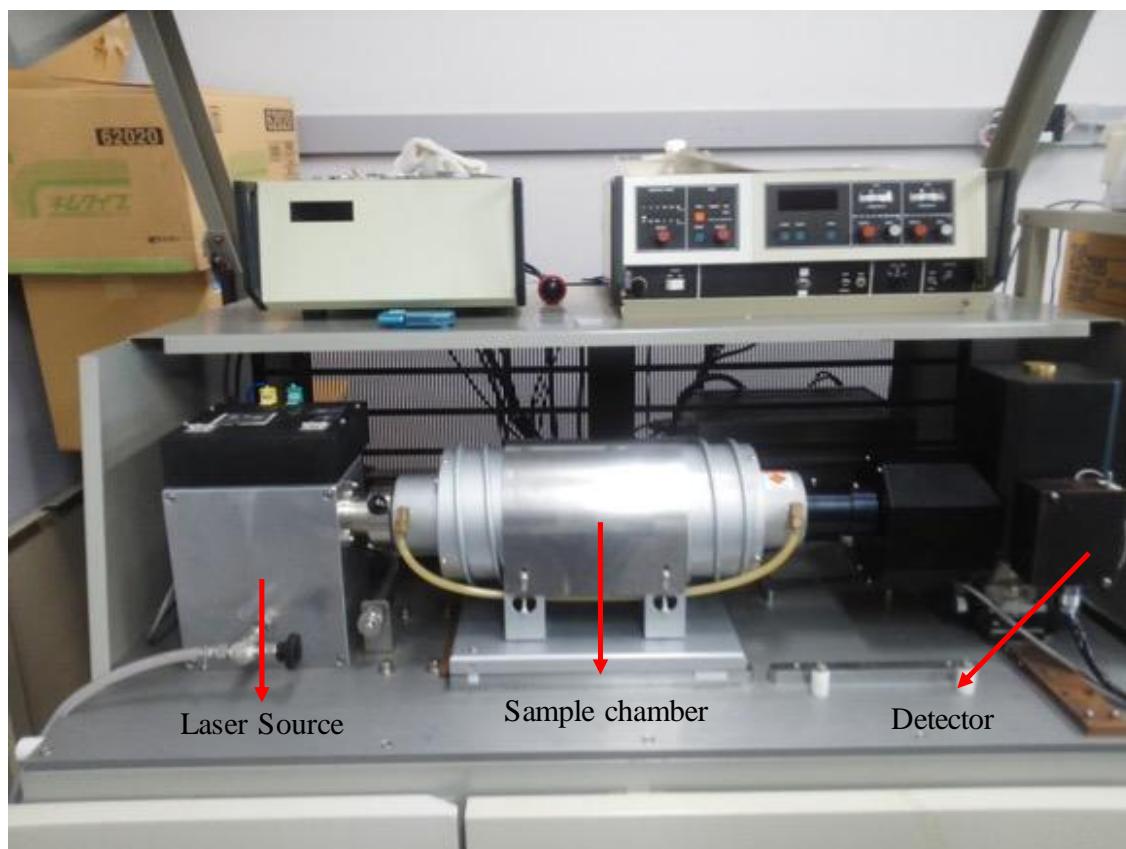


Figure 5. 8 The prepared samples for electrical transport measurement.

#### 5.4.2.1 Thermal Transport Measurement

The thermal conductivity was measured by Laser Flash method. The Ulvac Rico TC-7000 apparatus as shown in Figure 5.9 was used in this experiment. A laser pulse is applied to uniformly heat up one side of a disk-shaped sample and the time-dependent temperature rise is monitored by detector at the other side of sample. The conduction of heat is assumed to be one-dimensional in which there is no lateral heat loss. Therefore,

the sample thickness should be much smaller than the sample diameter. In order to ensure all the laser energy is absorbed and emitted by the sample, both of sample surfaces are coated by the graphite spray. [117-119]



*Figure 5. 9 The Ulvac Rico TC-7000 Laser Flash apparatus*

Before blackening the sample surface by graphite spray, the thermocouples (Pt and Pt-R13) were attached using the silica paste. Those thermocouples were joined by welding technique and then flattened by pressing machine for easy attaching process (see Figure 5.10). The sample is ready to be installed at the sample chamber of laser flash apparatus (Figure 5.11). The Pt wire of sample should be connected to the same Pt wire of apparatus and the same case for Pt-R13 wire.

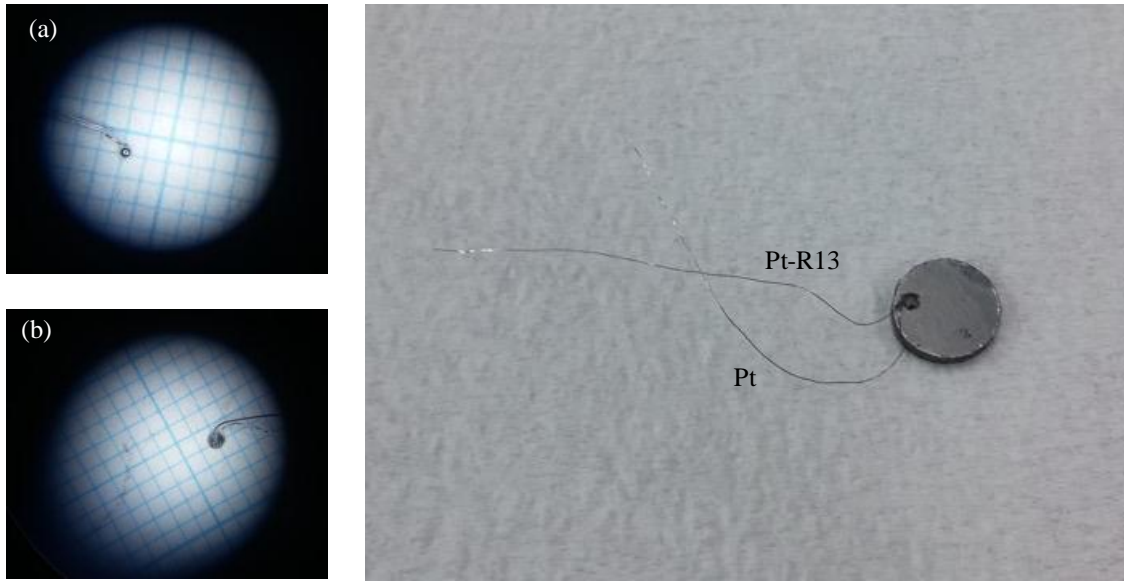


Figure 5. 10. (a) Welding result at one end of the thermocouples (b) The flattening of tip by pressing machine for easy attaching process (c) The thermocouples were attached at the edge of sample and then the sample surfaces were coated by graphite spray.

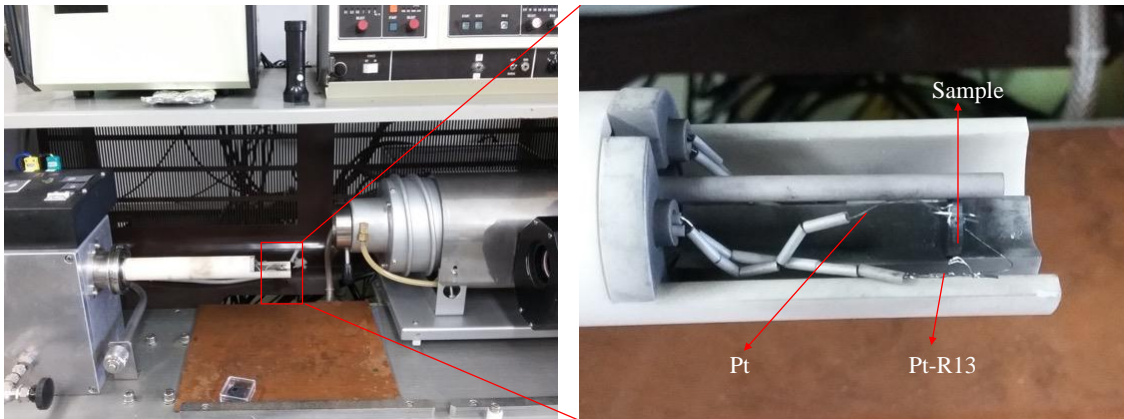


Figure 5. 11 The sample is installed at the sample chamber by connecting the Pt and Pt-R13 thermocouples of sample to the Pt and Pt-R13 of apparatus, respectively.

The thermal conductivity is calculated from the following equation [119]

$$\kappa = D_T \rho C_p \quad (5.19)$$

where  $D_T$  is the thermal diffusivity and  $C_p$  is the constant pressure heat capacity. The thermal diffusivity is given by

$$D_T = \frac{1.38r_t^2}{\pi^2 T_{1/2}} \quad (5.20)$$

where  $r_t$  is the sample thickness and  $T_{1/2}$  is the time required for the temperature to reach the half-maximum after irradiation with heat pulse. The typical curve of time-dependent temperature rise is shown in the figure below

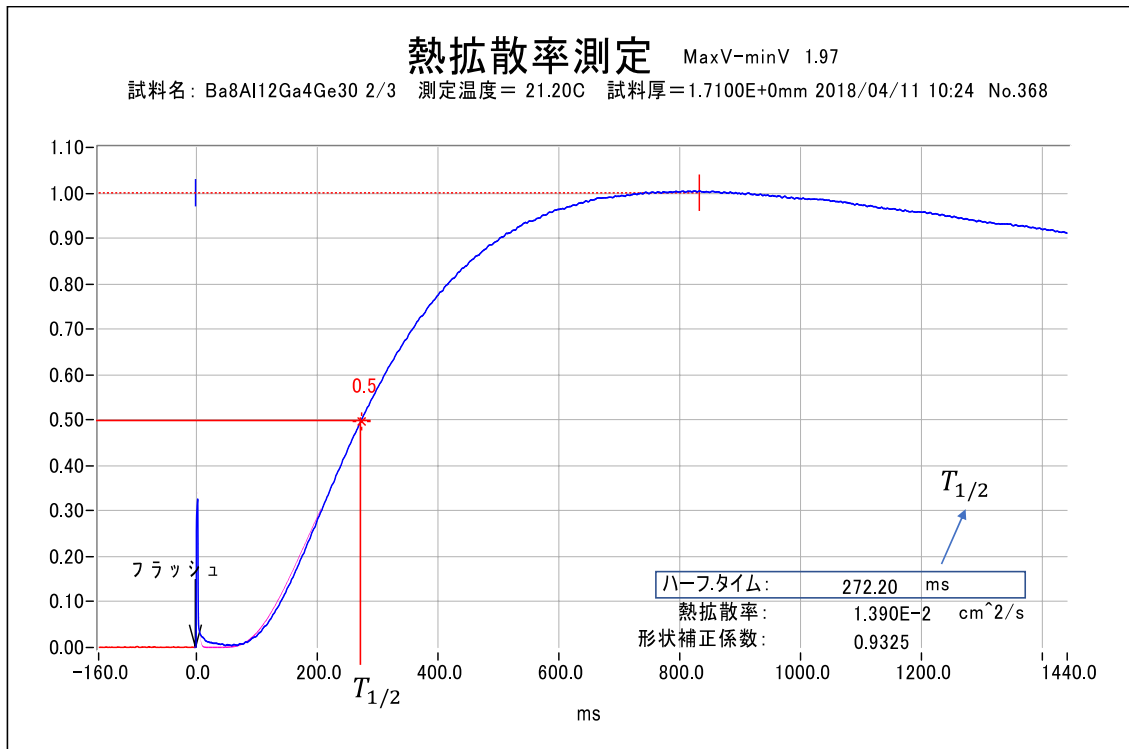


Figure 5. 12 The typical curve of time-dependent temperature rise on the back side of the sample after irradiation with heat pulse.

The constant pressure heat capacity  $C_p$  is calculated from the following equation

$$C_p = \frac{Q}{W_a \theta_m^T} \quad (5.21)$$

where  $Q$ ,  $W_a$ , and  $\theta_m^T$  are the absorption heat quantity, sample weight, and maximum value temperature rise, respectively.

### 5.4.2.2 Electrical Transport Measurement

For high-temperature measurement, the Seebeck coefficient and electrical resistivity were measured using *ZEM-3*. The principle of electrical transport measurement using *ZEM-3* is the same as the PPMS method. The heat is applied from the upper electrode and the temperature difference is set at the lower part. The temperatures were detected by the thermocouples at the center of sample bar with distance between probes  $L$ . The sample was connected to the Ni-electrode of apparatus in vertical position as shown in Figure 5.13. The samples were measured from room temperature to 943 K.

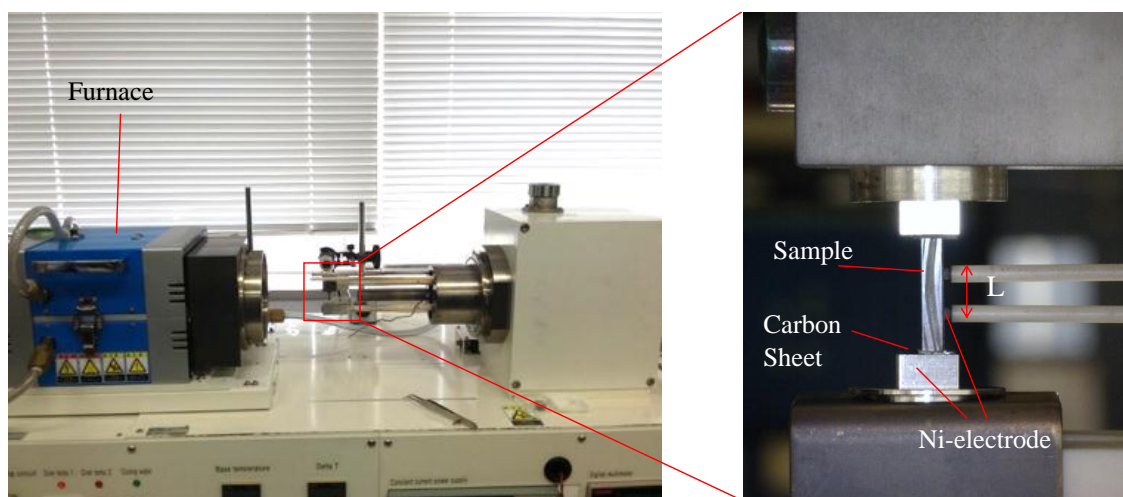


Figure 5. 13 Ulvac Riko *ZEM-3* Apparatus. The magnified figure is the set sample in vertical position which connected to the Ni-electrodes at the lower, upper, and along horizontal axis (thermocouples).

## 5.5 Results and Discussion

### 5.5.1 Low-Temperature

The thermoelectric properties as a function of temperature are shown in Figure 5.14. The negative sign in Seebeck coefficient corresponds to the electron as the majority of charge carriers in materials. This means that  $\text{Ba}_8\text{Al}_{16-x}\text{Ga}_x\text{Ge}_{30}$  ( $x = 0, 4, 8$ ) compounds is the n-type thermoelectric. By considering the absolute value of Seebeck coefficient, sample with  $\text{Ga} = 8$  has the largest Seebeck coefficient of  $43 \mu\text{V/K}$ . Also,  $\text{Ga} = 8$  exhibits larger value of electrical resistivity compared to the other two samples.

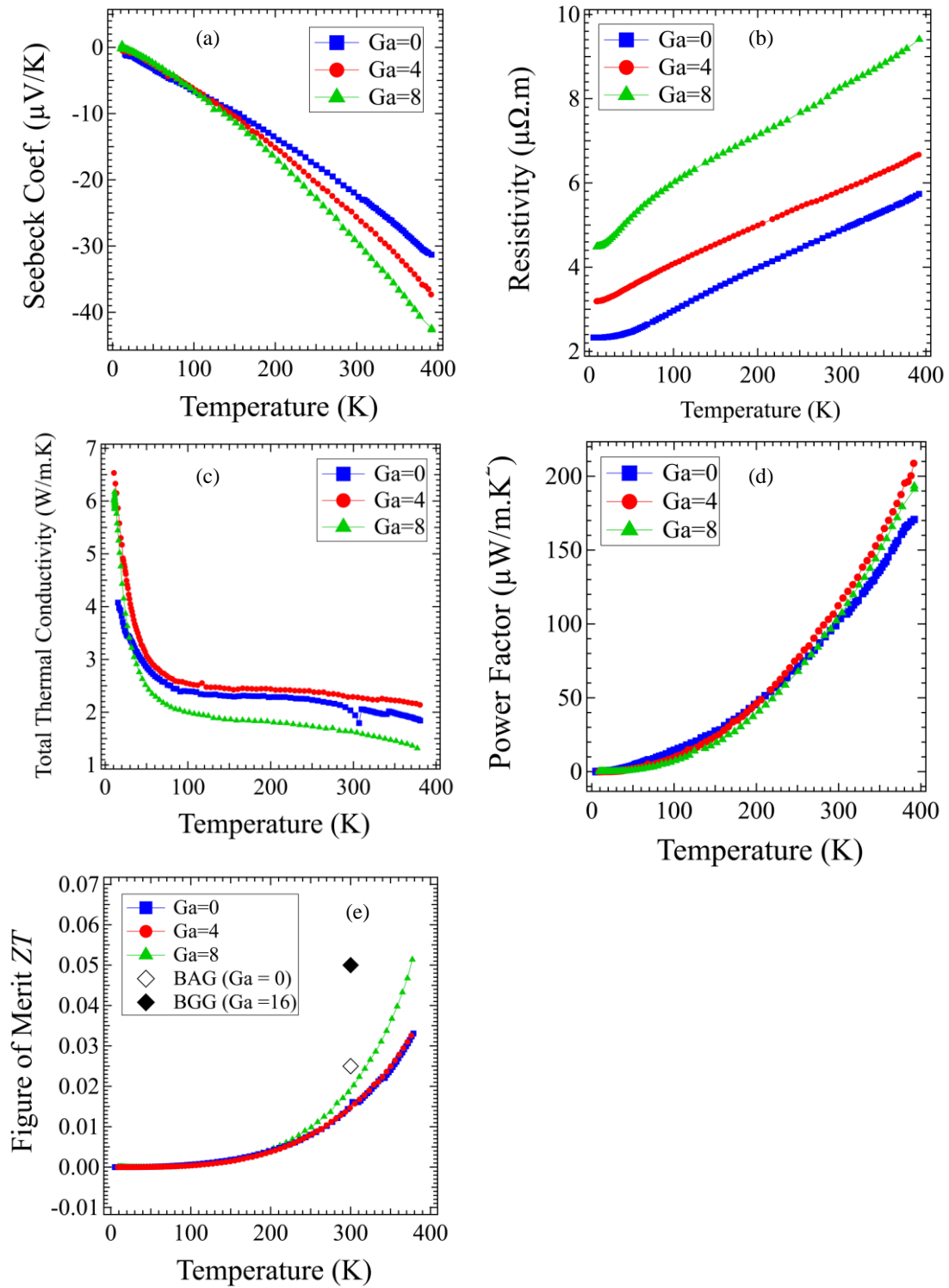


Figure 5. 14 The experimental thermoelectric properties of  $Ba_8Al_{16-x}Ga_xGe_{30}$  ( $x = 0, 4, 8$ ) as a function of temperature: (a) Seebeck coefficient, (b) electrical resistivity, (c) total thermal conductivity, (d) power factor, and (e) Figure of merit  $ZT$  and compared with the references [18, 68].

The thermal conductivity is lowest for the Ga = 8. The calculated figure of merit using the Eq. 1.11 shows the Ga = 8 to be the highest one. Since the total contribution of electrical properties described in the term of power factor ( $S^2/\rho$ ) is the highest at Ga = 4 sample, it can be concluded that the origin of high  $ZT$  in Ga = 8 is originated from the low thermal conductivity. However, the obtained  $ZT$  value of  $Ba_8Al_{16}Ge_{30}$  is much lower than the reference at the same temperature.

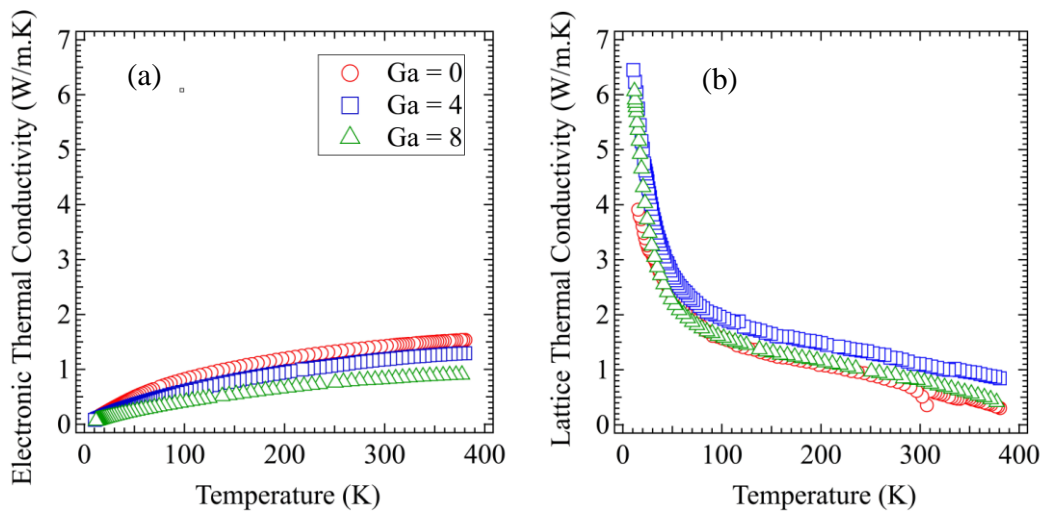


Figure 5.15 (a) The electronic and (b) lattice thermal conductivity as a function of temperature.

To determine the dominant contribution of thermal conductivity, the total thermal conductivity is subtracted by the electronic thermal conductivity. Then, the contribution of lattice is obtained (see Section 5.3). The calculated results are shown in Figure 5.15. If compared to the lattice contribution in Ga = 8, it is clearly shown that main contribution to lowering the thermal conductivity is originated from the electronic thermal conductivity. This low contribution in thermal transferred by electron is caused by high resistivity of Ga = 8. More Gallium doping will reduce the electron mobility.

## 5.5.2 High-Temperature

The thermoelectric properties as a function of temperature are shown in Figure 5.16. By considering the absolute value of Seebeck coefficient, sample with Ga = 4 and Ga = 8 have similar Seebeck coefficient value in which approximately 55% larger than the Ga = 0 sample. Ga = 4 exhibits larger value of electrical resistivity compared to the other two samples where Ga = 8 has middle position. Below ~600 K, the doping effect is not clearly seen. The thermal conductivity of Ga = 4 sample below ~600 K is shown as the lowest one. However, the value of thermal conductivity of Ga = 4 and Ga = 8 are only slightly different above 600 K. From the room temperature to the highest temperature point, the Ga = 0 increases about 73.3%, while for the Ga = 4 and Ga = 8 increase approximately 27.2% and 18.5%, respectively. Thus, by adding the Ga contents, reduce the dependency of temperature variations. Compared to the results by Uemura, *et al.*, [18] the thermal conductivity of Ga = 0 has different tendency. This result shows the increasing of thermal conductivity with increasing temperature, while the reference is independent of temperature variations. Both electrical and thermal properties contribute in the same level to increase the  $ZT$ . This can be clearly seen from Figures 5.16(c) and 5.16(d) with slightly higher  $ZT$  in Ga = 8 sample. The  $ZT$  is improved almost twice compared to the non-doped sample.

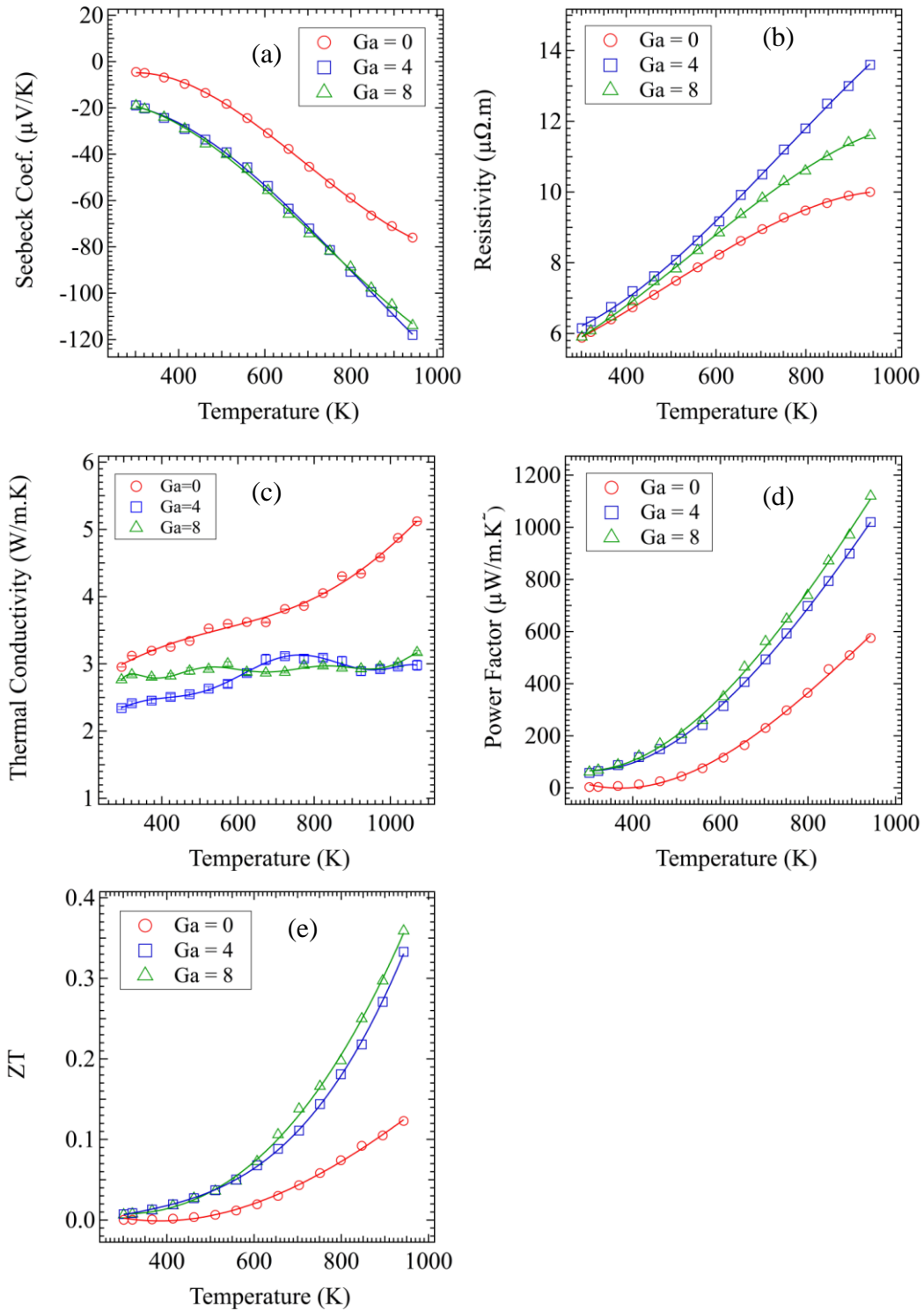


Figure 5. 16 The experimental thermoelectric properties of  $Ba_8Al_{16-x}Ga_xGe_{30}$  ( $x = 0, 4, 8$ ) as a function of temperature: (a) Seebeck coefficient, (b) electrical resistivity, (c) total thermal conductivity, (d) power factor, and (f) Figure of merit ZT and compared with the references [18, 68].

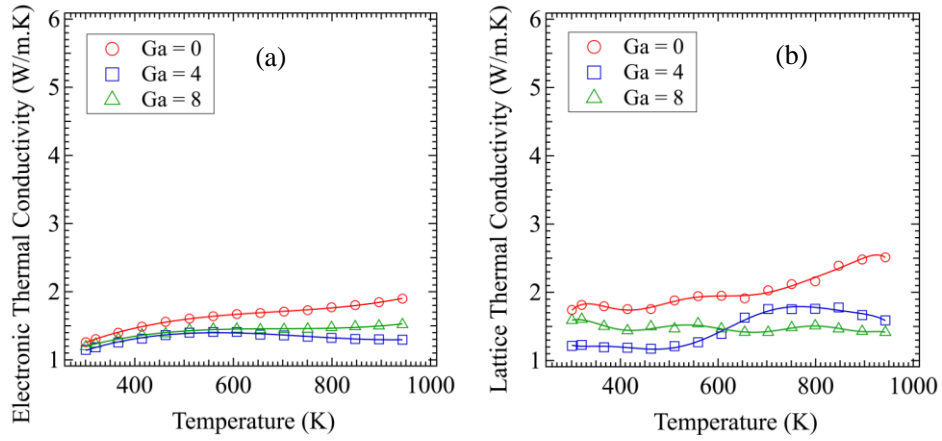


Figure 5.17 (a) The electronic and (b) lattice thermal conductivity of  $Ba_8Al_{16-x}Ga_xGe_{30}$  ( $x = 0, 4, 8$ ) as a function of temperature.

Figure 5.17 shows the electron and lattice contribution to the thermal conductivity. Since  $Ga = 4$  exhibits larger value for electrical resistivity, the electronic contribution in thermal conductivity is lower at  $Ga = 4$ . The low thermal conductivity in  $Ga = 8$  sample at higher temperature is originated from the contribution of lattice.

## Conclusion

The type I clathrate structure was confirmed in all sample  $\text{Ba}_8\text{Al}_{16-x}\text{Ga}_x\text{Ge}_{30}$  ( $x = 0, 2, 4, 6,$  and  $8$ ) by XRD. Rietveld refinement results show that the substitution of Al by Ga leads to reduce the lattice constant. The Ge occupancies are not affected by increasing the Ga ratio and dominantly occupied the  $16i$  and  $24k$  sites by 70%. The Al and Ga are occupied more at  $6c$  site. At low temperature, the ADPs and off-centered displacements are similar in both of  $\text{Ba}_8\text{Al}_{16}\text{Ge}_{30}$  and  $\text{Ba}_8\text{Al}_8\text{Ga}_8\text{Ge}_{30}$ . At high temperature, the ADPs of  $\text{Ba}_8\text{Al}_8\text{Ga}_8\text{Ge}_{30}$  is larger than that of  $\text{Ba}_8\text{Al}_{16}\text{Ge}_{30}$ , whereas, the off-centered displacement of  $\text{Ba}_8\text{Al}_8\text{Ga}_8\text{Ge}_{30}$  is smaller than that of  $\text{Ba}_8\text{Al}_{16}\text{Ge}_{30}$ . The distribution of Ba2 guest atom for  $\text{Ba}_8\text{Al}_{16}\text{Ge}_{30}$  and  $\text{Ba}_8\text{Al}_8\text{Ga}_8\text{Ge}_{30}$  is located at the  $24k$  site and the distribution size enlarges with increasing temperature. At 900 K, the Ba2 distribution of  $\text{Ba}_8\text{Al}_8\text{Ga}_8\text{Ge}_{30}$  grows wider along the  $y$  direction than that of  $\text{Ba}_8\text{Al}_{16}\text{Ge}_{30}$ . The Ga substitutions for Al suppress the thermal conductivity. The  $ZT$  is improved almost three times compared to the  $\text{Ba}_8\text{Al}_{16}\text{Ge}_{30}$  sample.

# List of Figures

Figure 1. 1 Schematic of Seebeck effect in (a) close circuit and (b) open circuit made of two different metal A and B. ....	2
Figure 1. 2 Schematic of Peltier effect in a close circuit made of two different metal A and B. ....	3
Figure 1. 3 Schematic of (a) thermoelectric generator (TEG) and (b) thermoelectric cooler (TEC). ....	5
Figure 1. 4 Maximum efficiency for TEG [Godart]. ....	9
Figure 1. 5 Summary of best ZT values for some typical classes of n-type thermoelectric materials as a function of temperature [13-23]. ....	10
Figure 1. 6 Crystal structure of the type-I clathrate. The guest atoms are shown as pink and dark red atoms at 6d (G2) and 2a (G1) position, respectively. The light blue, dark blue, and black atoms are the host structure atoms (A/B) at 6c, 16i, and 24k position, respectively. ....	12
Figure 1. 7 Atomic Coordination in the type-I clathrate .....	13
Figure 1. 8 Schematic illustration of the anharmonic potential for guest atom in tetrakaidecahedron cage, with 24k off-center position [54]. ....	15
Figure 1. 9 Anisotropic condition for guest atom in tetrakaidecahedron cage. ....	15
Figure 1. 10 Summary of lattice thermal conductivity data [30, 48, 50, 53] below 300 K with n and p denote the n- and p-type of clathrates, respectively. While norm corresponds to the solid-state synthesis and Czo denotes the Czochralski synthesis method. The dash line is the data of SiO <sub>2</sub> glass and the black line indicates the inverse temperature dependence characteristic in which Umklapp scattering is dominant. ....	16
Figure 1. 11 Summary of power factor data as function of charge carrier concentration for several Ba <sub>8</sub> TM <sub>x</sub> A <sub>y</sub> Ge <sub>46-x-y</sub> systems, where TM = group 11 and 12 elements, A = Al, Ga, In [37]. ....	17

Figure 2. 1 The illustration of arc melting furnace. ....	20
Figure 2. 2 (a) Inside the sample chamber which consists of copper hearth and electrode. (b) raw materials brought by the single desiccator. (c) The button shape of ingot as a result of arc melting process. ....	20
Figure 2. 3 Schematic diagram of SPS apparatus .....	21
Figure 2. 4 (a) Dry-sieving with screen of 45 $\mu\text{m}$ ; (b) The graphite die wrapping by graphite felt graphite felt to keep the temperature homogeneity; (c) The sintered sample covered by graphite foils.....	22
Figure 2. 5 Geometrical illustration of Bragg's Law. The green solid circles denote the lattice points. The diffraction maximum appears when the path difference $2\Delta$ , which is equal to $2dhklsin\theta$ , add to a multiple of the incident wavelength. ....	23
Figure 2. 6 X-ray diffraction pattern of $\text{Ba}_8\text{Al}_{16}\text{Ge}_{30}$ . The peaks are indexed according to the Pm-3n space.....	24
Figure 2. 7 XRD pattern of the $\text{Ba}_8\text{Al}_{16-x}\text{Ga}_x\text{Ge}_{30}$ (BAGG) samples with the labeled peaks of the impurity peaks. The flowers, stars, and pointing down triangles are Ge, $\text{Al}_2\text{BaO}_4$ , and Al peaks, respectively. ....	25
Figure 3. 1 Illustration of Super High-Resolution Powder Diffractometer (SuperHRPD) with resolution of $\Delta d/d=0.03\%$ [26].....	28
Figure 3. 2 X-ray diffraction pattern of $\text{Ba}_8\text{Al}_{16}\text{Ge}_{30}$ . The peak indexing is based on the Pm-3n space group.....	29
Figure 3. 3 (a) The 6d model) and (b)24k model using for the refinement of neutron diffraction data.....	30
Figure 3. 4 (a) Neutron diffraction patterns as function of d spacing at various temperature (b) Bragg peak positions shifted to the higher d spacing as temperature increases.....	31
Figure 3. 5 Rietveld refinement result for neutron diffraction data of $\text{Ba}_8\text{Al}_{16}\text{Ge}_{30}$ at 300 K refined using the 6d model. Red cross (+ symbols) and light blue line correspond to the observed and calculated intensity, respectively. The dark blue line denotes the difference between calculated and observed intensities. The short vertical green line indicates the Bragg reflection positions.....	32
Figure 3. 6 (a) Neutron diffraction patterns as function of d spacing at various temperature (b) 321 reflection of $\text{Ba}_8\text{Al}_{14}\text{Ga}_2\text{Ge}_{30}$ shifted to the higher d spacing as temperature increases.....	34

Figure 3. 7 Rietveld refinement result for neutron diffraction data of  $Ba_8Al_{14}Ga_2Ge_{30}$  at 300 K refined using the 6d model. Red cross (+ symbols) and light blue line correspond to the observed and calculated intensity, respectively. The dark blue line denotes the difference between calculated and observed intensities. The short vertical green line indicates the Bragg reflection positions. The black and pink arrows denote the impurities peaks of Al and Ge, respectively.....35

Figure 3. 8 (a) Neutron diffraction patterns as function of d spacing at various temperature (b) 321 reflection of  $Ba_8Al_{12}Ga_4Ge_{30}$  shifted to the higher d spacing as temperature increases. ....37

Figure 3. 9 Rietveld refinement result for neutron diffraction data of  $Ba_8Al_{12}Ga_4Ge_{30}$  at 300 K refined using the 6d model. Red cross (+ symbols) and light blue line correspond to the observed and calculated intensity, respectively. The dark blue line denotes the difference between calculated and observed intensities. The short vertical green line indicates the Bragg reflection positions. The black and pink arrows denote the impurities peaks of Al and Ge, respectively.....38

Figure 3. 10 Rietveld refinement result for neutron diffraction data of  $Ba_8Al_{10}Ga_6Ge_{30}$  at 300 K refined using the 6d model. Red cross (+ symbols) and light blue line correspond to the observed and calculated intensity, respectively. The dark blue line denotes the difference between calculated and observed intensities. The short vertical green line indicates the Bragg reflection positions. The black and pink arrows denote the impurities peaks of Al and Ge, respectively.....40

Figure 3. 11 (a) Neutron diffraction patterns as function of d spacing at various temperature (b) Bragg peak positions shifted to the higher d spacing as temperature increases. ....42

Figure 3. 12 Rietveld refinement result for neutron diffraction data of  $Ba_8Al_8Ga_8Ge_{30}$  at 300 K refined using the 6d model. Red cross (+ symbols) and light blue line correspond to the observed and calculated intensity, respectively. The dark blue line denotes the difference between calculated and observed intensities. The short vertical green line indicates the Bragg reflection positions. ....43

Figure 3. 13 The x dependences of (a) lattice constant, (b), (c), and (d) Ga, Al, and Ge occupancy from Rietveld refinement at room temperature. The red circle, blue square, green triangle pointing up correspond to the 6c, 16i, and 24k site, respectively. ....47

Figure 3. 14 The temperature dependences of (a) lattice constant, (b), (c), (d), (e), atomic displacement parameters (ADPs) from 6d and 24k model, and (f) off-centered displacement parameters for sample with x = 0 and x = 8. ....49

Figure 4. 1 Scattering amplitude density distribution of unit cell $Ba_8Al_{16}Ge_{30}$ obtained from MEM with isosurface level at $3.0 \text{ fm}/\text{\AA}^3$ . The magnified figure is Ba2 guest atom. The x, y, and z are defined as the local axis for the magnified Ba2 atom. ....	53
Figure 4. 2 The selected density distribution of Ba2 guest atom $Ba_8Al_{16}Ge_{30}$ . The x, y, and z are defined as the local axis for the Ba2 atom. To the right, the density distribution parallel to the y axis and half-cut parallel to x axis.....	54
Figure 4. 3 The nuclear density distribution of unit cell $Ba_8Al_8Ga_8Ge_{30}$ obtained from MEM with isosurface level at $4.3 \text{ fm}/\text{\AA}^3$ . The x, y, and z are defined as the local axis for the magnified Ba2 atom. ....	55
Figure 4. 4 The evolution of Ba2 density distribution $Ba_8Al_8Ga_8Ge_{30}$ . The x, y, and z are defined as the local axis for the Ba2 atom. First and the second row are the density distribution parallel to the y axis and half cut parallel to x axis, respectively.....	56
Figure 5. 1 Illustration of the relationship between the thermoelectric properties and carrier concentration [58].....	61
Figure 5. 2 Illustration of the benefit lowering the lattice thermal conductivity to improve Figure of merit ZT [58]. ....	61
Figure 5. 3 Wire Electric Discharge Machine (EDM).....	62
Figure 5. 4 The cutting results using Wire EDM for samples with Ga = 0,4, and 8. ....	63
Figure 5. 5 Physical Properties Measurement System (PPMS) instrument.....	64
Figure 5. 6 Thermal Transport Option (TTO) puck with a 10.82 mm in length $Ba_8Al_{16}Ge_{30}$ sample. ....	64
Figure 5. 7 The density determination kit of METTLER TOLEDO balance. [116] ....	65
Figure 5. 8 The prepared samples for electrical transport measurement. ....	66
Figure 5. 9 The Ulvac Rico TC-7000 Laser Flash apparatus .....	67
Figure 5. 10. (a) Welding result at one end of the thermocouples (b) The flattening of tip by pressing machine for easy attaching process (c) The thermocouples were attached at the edge of sample and then the sample surfaces were coated by graphite spray.....	68
Figure 5. 11 The sample is installed at the sample chamber by connecting the Pt and Pt-R13 thermocouples of sample to the Pt and Pt-R13 of apparatus, respectively. ....	68

Figure 5. 12 The typical curve of time-dependent temperature rise on the back side of the sample after irradiation with heat pulse.....	69
Figure 5. 13 Ulvac Riko ZEM-3 Apparatus. The magnified figure is the set sample in vertical position which connected to the Ni-electrodes at the lower, upper, and along horizontal axis (thermocouples). .....	70
Figure 5. 14 The experimental thermoelectric properties of $Ba_8Al_{16-x}Ga_xGe_{30}$ ( $x = 0, 4, 8$ ) as a function of temperature: (a) Seebeck coefficient, (b) electrical resistivity, (c) total thermal conductivity, (d) power factor, and (f) Figure of merit ZT and compared with the references [18, 68]. .....	71
Figure 5. 15 (a) The electronic and (b) lattice thermal conductivity as a function of temperature. ....	72
Figure 5. 16 The experimental thermoelectric properties of $Ba_8Al_{16-x}Ga_xGe_{30}$ ( $x = 0, 4, 8$ ) as a function of temperature: (a) Seebeck coefficient, (b) electrical resistivity, (c) total thermal conductivity, (d) power factor, and (f) Figure of merit ZT and compared with the references [18, 68]. .....	74
Figure 5. 17 (a) The electronic and (b) lattice thermal conductivity of $Ba_8Al_{16-x}Ga_xGe_{30}$ ( $x = 0, 4, 8$ ) as a function of temperature. ....	75

# List of Tables

Table 3. 1 The site occupancies factors of host atoms.....	32
Table 3. 2 Crystallographic information of $Ba_8Al_{16}Ge_{30}$ at the selected temperature points. The atomic coordinates in the refinements: Ba1 2a (0,0,0), Ba2 6d (1/4,1/2,0) or 24k (x,1/2,z), Al1/Ge1 6c (1/4,0,1/2), Al2/Ge2 16i (x, x, x), and Al3/Ge3 24k (0,y,z).	33
Table 3. 3 The site occupancies factors of host atoms for $Ba_8Al_{14}Ga_2Ge_{30}$ sample.....	35
Table 3. 4 Crystallographic information of $Ba_8Al_{14}Ga_2Ge_{30}$ at the selected temperature points. The atomic coordinates in the refinements: Ba1 2a (0,0,0), Ba2 6d (1/4,1/2,0) or 24k (x,1/2,z), Al1/Ge1 6c (1/4,0,1/2), Al2/Ge2 16i (x, x, x), and Al3/Ge3 24k (0,y,z).	36
Table 3. 5 The site occupancies factors of host atoms for $Ba_8Al_{12}Ga_4Ge_{30}$ sample.....	38
Table 3. 6 Crystallographic information of $Ba_8Al_{12}Ga_4Ge_{30}$ at the selected temperature points. The atomic coordinates in the refinements: Ba1 2a (0,0,0), Ba2 6d (1/4,1/2,0) or 24k (x,1/2,z), Al1/Ge1 6c (1/4,0,1/2), Al2/Ge2 16i (x, x, x), and Al3/Ge3 24k (0,y,z).	39
Table 3. 7 The site occupancies factors of host atoms for $Ba_8Al_{10}Ga_6Ge_{30}$ sample.....	40
Table 3. 8 Crystallographic information of $Ba_8Al_{12}Ga_4Ge_{30}$ at 300 K. The atomic coordinates in the refinements: Ba1 2a (0,0,0), Ba2 6d (1/4,1/2,0) or 24k (x,1/2,z), Al1/Ge1 6c (1/4,0,1/2), Al2/Ge2 16i (x, x, x), and Al3/Ge3 24k (0,y,z).....	41
Table 3. 9 The site occupancies factors of host atoms for $Ba_8Al_8Ga_8Ge_{30}$ sample.....	43
Table 3. 10 Crystallographic information of $Ba_8Al_8Ga_8Ge_{30}$ at the selected temperature points. The atomic coordinates in the refinements: Ba1 2a (0,0,0), Ba2 6d (1/4,1/2,0) or 24k (x,1/2,z), Al1/Ge1 6c (1/4,0,1/2), Al2/Ge2 16i (x, x, x), and Al3/Ge3 24k (0,y,z).	44
Table 3. 11 Selected crystallographic information for $Ba_8Al_{16-x}Ga_xGe_{30}$ obtained from Rietveld refinement of neutron powder diffraction data. The atomic coordinates in the refinements: Ba1 2a (0,0,0), Ba2 6d (1/4,1/2,0) or 24k (x,1/2,z), Al1/Ge1 6c (1/4,0,1/2), Al2/Ge2 16i (x, x, x), and Al3/Ge3 24k (0,y,z).	45
Table 3. 12 Site occupancies of aluminum for $Ba_8Al_{16}Ge_{30}$ .....	46
Table 3. 13 Site occupancies of Aluminum and Gallium for $Ba_8Al_{16-x}Ga_xGe_{30}$ .....	48
Table 5. 1 Density of samples with Ga = 0,4, and 8.....	66

# Bibliography

- [1] Seebeck, T.J. (1822). Magnetic polarization of metal and minerals. *Abhandlungen der Deutschen Akademie der Wissenschaften zu Berlin*, 265, 1822-1823.
- [2] Maciá, E. (2015). *Thermoelectric materials: advances and applications*. Pan Stanford: Singapore.
- [3] Goldsmid, H. J. (2010). *Introduction to thermoelectricity* (Vol. 121). Berlin: Springer.
- [4] Rowe, D. M. (2006). General principle and basic considerations. In Rowe, D. M. (Ed.), *Thermoelectrics handbook: macro to nano* (pp. 1-1 to 1-13). Boca Raton, FL: CRC press.
- [5] Peltier, J.C. (1834). Nouvelles experience sur la caloricité des courans électrique. *Ann. Chim. Phys*, 56(371), 371-386.
- [6] Ioffe, A.F. (1957). *Semiconductor thermoelements and thermoelectric cooling*. London: Infosearch.
- [7] Thomson, W. (1882). *Mathematical and Physical Papers*, Cambridge, Vol 1, p. 558, Vol 2, p. 306.
- [8] Altenkirch, E. (1909). Über den nutzeffekt der Thermosäule. *Phys. Z.*, 10, 560.
- [9] Altenkirch, E. (1911). Electrochemical refrigeration and reversible heating. *Phys. Z.*, 12, 920.
- [10] Godart, C., Gonçalves, A. P., Lopes, E. B., & Villeroy, B. (2009). Role of structures on thermal conductivity in thermoelectric materials. In *Properties and Applications of Thermoelectric Materials* (pp. 19-49). Springer, Dordrecht.
- [11] Han, C., Li, Z., & Dou, S. (2014). Recent progress in thermoelectric materials. *Chinese science bulletin*, 59(18), 2073-2091.

- [12] Vining, C. B. (2009). An inconvenient truth about thermoelectrics. *Nature materials*, 8(2), 83-85.
- [13] Goldsmid, H. J., & Douglas, R. W. (1954). The use of semiconductors in thermoelectric refrigeration. *British Journal of Applied Physics*, 5(11), 386-390.
- [14] Hu, L., Wu, H., Zhu, T., Fu, C., He, J., Ying, P., & Zhao, X. (2015). Tuning Multiscale Microstructures to Enhance Thermoelectric Performance of n-Type Bismuth-Telluride-Based Solid Solutions. *Advanced Energy Materials*, 5(17), 1500411.
- [15] Pei, Y., Lensch-Falk, J., Toberer, E. S., Medlin, D. L., & Snyder, G. J. (2011). High thermoelectric performance in PbTe due to large nanoscale Ag<sub>2</sub>Te precipitates and La doping. *Advanced Functional Materials*, 21(2), 241-249.
- [16] Hsu, K. F., Loo, S., Guo, F., Chen, W., Dyck, J. S., Uher, C., ... & Kanatzidis, M. G. (2004). Cubic AgPb<sub>m</sub>SbTe<sub>2+m</sub>: bulk thermoelectric materials with high figure of merit. *Science*, 303(5659), 818-821.
- [17] Shi, X., Yang, J., Salvador, J. R., Chi, M., Cho, J. Y., Wang, H., ... & Chen, L. (2011). Multiple-filled skutterudites: high thermoelectric figure of merit through separately optimizing electrical and thermal transports. *Journal of the American Chemical Society*, 133(20), 7837-7846.
- [18] Saramat, A., Svensson, G., Palmqvist, A. E. C., Stiewe, C., Müller, E., Platzek, D., ... & Stucky, G. D. (2006). Large thermoelectric figure of merit at high temperature in Czochralski-grown clathrate Ba<sub>8</sub>Ga<sub>16</sub>Ge<sub>30</sub>. *Journal of Applied Physics*, 99(2), 023708.
- [19] Liu, W., Tan, X., Yin, K., Liu, H., Tang, X., Shi, J., ... & Uher, C. (2012). Convergence of conduction bands as a means of enhancing thermoelectric performance of n-type Mg<sub>2</sub>Si<sub>1-x</sub>Sn<sub>x</sub> solid solutions. *Physical review letters*, 108(16), 166601.
- [20] Liu, W., Kim, H. S., Chen, S., Jie, Q., Lv, B., Yao, M., ... & Ren, Z. (2015). n-type thermoelectric material Mg<sub>2</sub>Sn<sub>0.75</sub>Ge<sub>0.25</sub> for high power generation. *Proceedings of the National Academy of Sciences*, 112(11), 3269-3274.
- [21] Yu, B., Zebarjadi, M., Wang, H., Lukas, K., Wang, H., Wang, D., ... & Ren, Z. (2012). Enhancement of thermoelectric properties by modulation-doping in silicon germanium alloy nanocomposites. *Nano letters*, 12(4), 2077-2082.
- [22] Liu, Y., Xie, H., Fu, C., Snyder, G. J., Zhao, X., & Zhu, T. (2015). Demonstration of a phonon-glass electron-crystal strategy in (Hf, Zr)NiSn half-Heusler thermoelectric materials by alloying. *Journal of Materials Chemistry*

A, 3(45), 22716-22722.

- [23] Liu, Y., Xie, H., Fu, C., Snyder, G. J., Zhao, X., & Zhu, T. (2015). Demonstration of a phonon-glass electron-crystal strategy in (Hf, Zr)NiSn half-Heusler thermoelectric materials by alloying. *Journal of Materials Chemistry A*, 3(45), 22716-22722.
- [24] Davy, H. (1811). VIII. On a combination of oxymuriatic gas and oxygene gas. *Philosophical Transactions of the Royal society of London*, 101, 155-162.
- [25] Cros, C., Pouchard, M., & Hagenmuller, P. (1970). Sur une nouvelle famille de clathrates minéraux isotypes des hydrates de gaz et de liquides. Interprétation des résultats obtenus. *Journal of Solid State Chemistry*, 2(4), 570-581.
- [26] Slack, G.A., (1995). New materials and performance limits for thermoelectric cooling. In Rowe, D. M. (Ed.), *CRC Handbook of Thermoelectrics* (pp. 407-440). Boca Raton, FL: CRC press.
- [27] Nolas, G., Cohn, J. L., Slack, G. A., & Schujman, S. B. (1998). Semiconducting Ge clathrates: Promising candidates for thermoelectric applications. *Applied Physics Letters*, 73(2), 178-180.
- [28] Fukuoka, H., Kiyoto, J., & Yamanaka, S. (2003). Superconductivity of Metal Deficient Silicon Clathrate Compounds,  $Ba_{8-x}Si_{46}$  ( $0 < x \leq 1.4$ ). *Inorganic chemistry*, 42(9), 2933-2937.
- [29] Imai, M., Nishida, K., Kimura, T., & Yamada, K. (2002). Synthesis of a Si-clathrate compound,  $Sr_8Ga_xSi_{46-x}$ , and its electrical resistivity measurements. *Journal of alloys and compounds*, 335(1-2), 270-276.
- [30] Sales, B. C., Chakoumakos, B. C., Jin, R., Thompson, J. R., & Mandrus, D. (2001). Structural, magnetic, thermal, and transport properties of  $X_8Ga_{16}Ge_{30}$  (X= E u, S r, B a) single crystals. *Physical Review B*, 63(24), 245113.
- [31] Paschen, S., Carrillo-Cabrera, W., Bentien, A., Tran, V. H., Baenitz, M., Grin, Y., & Steglich, F. (2001). Structural, transport, magnetic, and thermal properties of  $Eu_8Ga_{16}Ge_{30}$ . *Physical Review B*, 64(21), 214404.
- [32] Dong, J., & Sankey, O. F. (1999). Theoretical study of two expanded phases of crystalline germanium: clathrate-I and clathrate-II. *Journal of Physics: Condensed Matter*, 11(32), 6129.
- [33] Nolas, G. S., Cohn, J. L., Dyck, J. S., Uher, C., & Yang, J. (2002). Transport properties of polycrystalline type-I Sn clathrates. *Physical Review B*, 65(16), 165201.
- [34] Hermann, R. P., Schweika, W., Leupold, O., Ruffer, R., Nolas, G. S.,

- Grandjean, F., & Long, G. J. (2005). Neutron and nuclear inelastic scattering study of the Einstein oscillators in Ba-, Sr-, and Eu-filled germanium clathrates. *Physical Review B*, 72(17), 174301.
- [35] Christensen, M., Lock, N., Overgaard, J., & Iversen, B. B. (2006). Crystal structures of thermoelectric n-and p-type Ba<sub>8</sub>Ga<sub>16</sub>Ge<sub>30</sub> studied by single crystal, multitemperature, neutron diffraction, conventional X-ray diffraction and resonant synchrotron X-ray diffraction. *Journal of the American Chemical Society*, 128(49), 15657-15665.
- [36] Toberer, E. S., Christensen, M., Iversen, B. B., & Snyder, G. J. (2008). High temperature thermoelectric efficiency in Ba<sub>8</sub>Ga<sub>16</sub>Ge<sub>30</sub>. *Physical Review B*, 77(7), 075203
- [37] Christensen, M., Johnsen, S., & Iversen, B. B. (2010). Thermoelectric clathrates of type I. *Dalton transactions*, 39(4), 978-992.
- [38] Rogl, P. (2006). Formation and crystal chemistry of clathrates. In Rowe, D. M. (Ed.), *Thermoelectrics handbook: macro to nano* (pp. 32.1- 32-16). Boca Raton, FL: CRC press.
- [39] Dolyniuk, J. A., Owens-Baird, B., Wang, J., Zaikina, J. V., & Kovnir, K. (2016). Clathrate thermoelectrics. *Materials Science and Engineering: R: Reports*, 108, 1-46.
- [40] Kovnir, K. A., & Shevelkov, A. V. (2004). Semiconducting clathrates: synthesis, structure and properties. *Russian chemical reviews*, 73(9), 923-938.
- [41] Kauzlarich, S. M., Brown, S. R., & Snyder, G. J. (2007). Zintl phases for thermoelectric devices. *Dalton Transactions*, (21), 2099-2107.
- [42] Shevelkov, A. V., & Kovnir, K. (2010). Zintl clathrates. In *Zintl Phases* (pp. 97-142). Springer, Berlin, Heidelberg.
- [43] Paschen, S., Pacheco, V., Bentien, A., Sanchez, A., Carrillo-Cabrera, W., Baenitz, M., ... & Steglich, F. (2003). Are type-I clathrates Zintl phases and 'phonon glasses and electron single crystals'?. *Physica B: Condensed Matter*, 328(1-2), 39-43.
- [44] Sales, B. C., Mandrus, D., Chakoumakos, B. C., Keppens, V., & Thompson, J. R. (1997). Filled skutterudite antimonides: Electron crystals and phonon glasses. *Physical Review B*, 56(23), 15081.
- [45] Rull-Bravo, M., Moure, A., Fernandez, J. F., & Martin-Gonzalez, M. (2015). Skutterudites as thermoelectric materials: revisited. *Rsc Advances*, 5(52), 41653-41667.

- [46] Caplin, A. D., Grüner, G., & Dunlop, J. B. (1973). Al 10 V: An Einstein Solid. *Physical Review Letters*, 30(22), 1138.
- [47] Tse, J. S., & White, M. A. (1988). Origin of glassy crystalline behavior in the thermal properties of clathrate hydrates: a thermal conductivity study of tetrahydrofuran hydrate. *The Journal of Physical Chemistry*, 92(17), 5006-5011.
- [48] Cohn, J. L., Nolas, G. S., Fessatidis, V., Metcalf, T. H., & Slack, G. A. (1999). Glasslike heat conduction in high-mobility crystalline semiconductors. *Physical Review Letters*, 82(4), 779.
- [49] Terumasa Tadano, Yoshihiro Gohda, and Shinji Tsuneyuki. Impact of Rattlers on Thermal Conductivity of a Thermoelectric Clathrate: A First-Principles Study. *Phys. Rev. Lett.*, 114:095501, 2015.
- [50] Avila, M. A., Suekuni, K., Umeo, K., Fukuoka, H., Yamanaka, S., & Takabatake, T. (2006). Glasslike versus crystalline thermal conductivity in carrier-tuned  $\text{Ba}_8\text{Ga}_{16}\text{X}_{30}$  clathrates (X= Ge, Sn). *Physical Review B*, 74(12), 125109.
- [51] Suekuni, K., Avila, M. A., Umeo, K., & Takabatake, T. (2007). Cage-size control of guest vibration and thermal conductivity in  $\text{Sr}_8\text{Ga}_{16}\text{Si}_{30-x}\text{Ge}_x$ . *Physical Review B*, 75(19), 195210.
- [52] Tanaka, T., Onimaru, T., Suekuni, K., Mano, S., Fukuoka, H., Yamanaka, S., & Takabatake, T. (2010). Interplay between thermoelectric and structural properties of type-I clathrate  $\text{K}_8\text{Ga}_8\text{Sn}_{38}$  single crystals. *Physical Review B*, 81(16), 165110.
- [53] Christensen, M., & Iversen, B. B. (2007). Host structure engineering in thermoelectric clathrates. *Chemistry of Materials*, 19(20), 4896-4905.
- [54] Avila, M. A., Suekuni, K., Umeo, K., Fukuoka, H., Yamanaka, S., & Takabatake, T. (2008).  $\text{Ba}_8\text{Ga}_{16}\text{Sn}_{30}$  with type-I clathrate structure: Drastic suppression of heat conduction. *Applied Physics Letters*, 92(4), 041901.
- [55] Nakayama, T., & Kanashita, E. (2008). Interacting dipoles in type-I clathrates: Why glass-like though crystalline?. *EPL (Europhysics Letters)*, 84(6), 66001.
- [56] Chakoumakos, B. C., Sales, B. C., Mandrus, D. G., & Nolas, G. S. (2000). Structural disorder and thermal conductivity of the semiconducting clathrate  $\text{Sr}_8\text{Ga}_{16}\text{Ge}_{30}$ . *Journal of alloys and compounds*, 296(1-2), 80-86.
- [57] Takabatake, T., Suekuni, K., Nakayama, T., & Kanashita, E. (2014). Phonon-

- glass electron-crystal thermoelectric clathrates: Experiments and theory. *Reviews of Modern Physics*, 86(2), 669.
- [58] Snyder, G. J., & Toberer, E. S. (2011). Complex thermoelectric materials. In *Materials for Sustainable Energy: A Collection of Peer-Reviewed Research and Review Articles from Nature Publishing Group* (pp. 101-110).
- [59] Yang, J., Xi, L., Qiu, W., Wu, L., Shi, X., Chen, L., ... & Singh, D. J. (2016). On the tuning of electrical and thermal transport in thermoelectrics: an integrated theory–experiment perspective. *npj Computational Materials*, 2, 15015.
- [60] Shi, X., Yang, J., Bai, S., Yang, J., Wang, H., Chi, M., ... & Wong-Ng, W. (2010). On the design of high-efficiency thermoelectric clathrates through a systematic cross-substitution of framework elements. *Advanced Functional Materials*, 20(5), 755-763.
- [61] Anno, H., Hokazono, M., Kawamura, M., & Matsubara, K. (2003, August). Effect of transition element substitution on thermoelectric properties of semiconductor clathrate compounds. In *Thermoelectrics, 2003 Twenty-Second International Conference on-ICT* (pp. 121-126). IEEE.
- [62] Anno, H., Hokazono, M., Takakura, H., & Matsubara, K. (2005, June). Thermoelectric properties of  $\text{Ba}_x\text{Au}_{1-x}\text{Ge}_{46-x}$  clathrate compounds. In *Thermoelectrics, 2005. ICT 2005. 24th International Conference on* (pp. 102-105). IEEE.
- [63] Jones, J. A., Bowman, B., & Lefrank, P. A. (1998). Electric furnace steelmaking. In Fruehan, R. J. (Ed.), *The Making, Shaping and Treating of Steel* (pp. 525-527). Pittsburgh: The AISE Steel Foundation.
- [64] Omori, M. (2000). Sintering, consolidation, reaction and crystal growth by the spark plasma system (SPS). *Materials Science and Engineering: A*, 287(2), 183-188.
- [65] Guillon, O., Gonzalez-Julian, J., Dargatz, B., Kessel, T., Schierning, G., Räthel, J., & Herrmann, M. (2014). Field-assisted sintering technology/spark plasma sintering: mechanisms, materials, and technology developments. *Advanced Engineering Materials*, 16(7), 830-849.
- [66] Chen, W., Anselmi-Tamburini, U., Garay, J. E., Groza, J. R., & Munir, Z. A. (2005). Fundamental investigations on the spark plasma sintering/synthesis process: I. Effect of dc pulsing on reactivity. *Materials Science and*

*Engineering: A*, 394(1-2), 132-138.

- [67] Chen, F., Yang, S., Wu, J., Galaviz Perez, J. A., Shen, Q., Schoenung, J. M., & Zhang, L. (2015). Spark plasma sintering and densification mechanisms of conductive ceramics under coupled thermal/electric fields. *Journal of the American Ceramic Society*, 98(3), 732-740.
- [68] Uemura, T., Akai, K., Koga, K., Tanaka, T., Kurisu, H., Yamamoto, S., & Matsuura, M. (2008). Electronic structure and thermoelectric properties of clathrate compounds  $Ba_8Al_xGe_{46-x}$ . *Journal of Applied Physics*, 104(1), 013702.
- [69] Tokita, M. (1999). Development of large-size ceramic/metal bulk FGM fabricated by spark plasma sintering. In *Materials science forum* (Vol. 308, pp. 83-88). Trans Tech Publications.
- [70] Pecharsky, V., & Zavalij, P. (2008). *Fundamentals of powder diffraction and structural characterization of materials* (pp. 133-149). Berlin: Springer.
- [71] Jenkins, R., & Snyder, R. L. (1996). *Introduction to X-ray powder diffractometry* (pp. 47-95). Canada: John Wiley & Sons.
- [72] Waseda, Y., Matsubara, E., & Shinoda, K. (2011). *X-ray diffraction crystallography: introduction, examples and solved problems* (pp. 67-76, 107-114). Berlin: Springer.
- [73] Bragg, W. H., & WL Bragg, B. A. (1913). The reflection of X-rays by crystals. *Proc. R. Soc. Lond. A*, 88(605), 428-438.
- [74] Price, D. L., & Skold, K. (1986). Introduction to Neutron Scattering. In *Methods in Experimental Physics* (Vol. 23, pp. 1-97). Academic Press.
- [75] Furrer, A., & Strassle, T. (2009). *Neutron scattering in condensed matter physics*. Singapore: World Scientific Publishing Company.
- [76] Feigin, L. A., Svergun, D. I., & Taylor, G. W. (1987). Principles of the theory of X-ray and neutron scattering. In *Structure Analysis by Small-Angle X-Ray and Neutron Scattering* (pp. 3-24). Springer, Boston, MA.
- [77] Chatterji, T. (Ed.). (2005). *Neutron scattering from magnetic materials*. Gulf Professional Publishing.
- [78] Dianoux, A.-J., Lander, G. (2003). *Neutron Data Booklet (Second Edition)*.

Grenoble: Institut Laue-Langevin.

- [79] Torii, S., Yonemura, M., Yulius Surya Panca Putra, T., Zhang, J., Miao, P., Muroya, T., ... & Noda, Y. (2011). Super High Resolution Powder Diffractometer at J-PARC. *Journal of the Physical Society of Japan*, 80(Suppl. B), SB020.
- [80] Maekawa, F., Harada, M., Oikawa, K., Teshigawara, M., Kai, T., Meigo, S. I., ... & Kato, T. (2010). First neutron production utilizing J-PARC pulsed spallation neutron source JSNS and neutronic performance demonstrated. *Nuclear Instruments and Methods in Physics Research Section A: Accelerators, Spectrometers, Detectors and Associated Equipment*, 620(2-3), 159-165.
- [81] Reichelt, J. M. A., & Rodgers, A. L. (1966). Neutron diffraction by time-of-flight. *Nuclear Instruments and Methods*, 45(2), 245-249.
- [82] Sasaki, Y., Kishimoto, K., Koyanagi, T., Asada, H., & Akai, K. (2009). Synthesis and thermoelectric properties of type-VIII germanium clathrates  $\text{Sr}_8\text{Al}_x\text{Ga}_y\text{Ge}_{46-x-y}$ . *Journal of Applied Physics*, 105(7), 073702.
- [83] Kishimoto, K., Ikeda, N., Akai, K., & Koyanagi, T. (2008). Synthesis and thermoelectric properties of silicon clathrates  $\text{Sr}_8\text{Al}_x\text{Ga}_{16-x}\text{Si}_{30}$  with the type-I and type-VIII structures. *Applied physics express*, 1(3), 031201.
- [84] Oishi, R., Yonemura, M., Nishimaki, Y., Torii, S., Hoshikawa, A., Ishigaki, T., Morishima, T., & Kamiyama, T. (2009). Rietveld analysis software for J-PARC. *Nuclear Instruments and Methods in Physics Research Section A: Accelerators, Spectrometers, Detectors and Associated Equipment*, 600(1), 94-96.
- [85] Zhang, J., Kiyonagi, R., Yonemura, M., Ishikawa Y., & Kamiyama, T. (2014). Z-MEM, Textbook of Z-code Powder Diffraction Data Analysis School, Tokyo, March 25–26.
- [86] Ishikawa Y., Yonemura, M., & Kamiyama, T. (2014). Z-3D, Textbook of Z-code Powder Diffraction Data Analysis School, Tokyo, March 25–26.
- [87] Loewenstein, W. (1954). The distribution of aluminum in the tetrahedra of silicates and aluminates. *Am Mineral*, 39, 92-96.
- [88] Blake, N. P., Bryan, D., Lattner, S., Møllnitz, L., Stucky, G. D., & Metiu, H. (2001). Structure and stability of the clathrates  $\text{Ba}_8\text{Ga}_{16}\text{Ge}_{30}$ ,  $\text{Sr}_8\text{Ga}_{16}\text{Ge}_{30}$ ,

Ba<sub>8</sub>Ga<sub>16</sub>Si<sub>30</sub>, and Ba<sub>8</sub>In<sub>16</sub>Sn<sub>30</sub>. *The Journal of Chemical Physics*, 114(22), 10063-10074.

- [89] von der Linden, W., Dose, V., Fisher, R. & Preuss, R., eds (1998), *Maximum Entropy and Bayesian Methods*, Kluwer Academic Publishers, Dordrecht.
- [90] Gull, S. F., & Daniell, G. J. (1978). Image reconstruction from incomplete and noisy data. *Nature*, 272(5655), 686.
- [91] Benti, A., Iversen, B. B., Bryan, J. D., Stucky, G. D., Palmqvist, A. E. C., Schultz, A. J., & Henning, R. W. (2002). Maximum entropy method analysis of thermal motion and disorder in thermoelectric clathrate Ba<sub>8</sub>Ga<sub>16</sub>Si<sub>30</sub>. *Journal of applied physics*, 91(9), 5694-5699.
- [92] Christensen, S., Avila, M. A., Suekuni, K., Piltz, R., Takabatake, T., & Christensen, M. (2013). Combined X-ray and neutron diffraction study of vacancies and disorder in the dimorphic clathrate Ba<sub>8</sub>Ga<sub>16</sub>Sn<sub>30</sub> of type I and VIII. *Dalton Transactions*, 42(41), 14766-14775.
- [93] Kato, Y., Hori, S., Saito, T., Suzuki, K., Hirayama, M., Mitsui, A., ... & Kanno, R. (2016). High-power all-solid-state batteries using sulfide superionic conductors. *Nature Energy*, 1(4), 16030.
- [94] Hori, S., Taminato, S., Suzuki, K., Hirayama, M., Kato, Y., & Kanno, R. (2015). Structure–property relationships in lithium superionic conductors having a Li<sub>10</sub>GeP<sub>2</sub>S<sub>12</sub>-type structure. *Acta Crystallographica Section B*, 71(6), 727-736.
- [95] Collins, D. M. (1982). Electron density images from imperfect data by iterative entropy maximization. *Nature*, 298(5869), 49-51.
- [96] Sakata, M., & Sato, M. (1990). Accurate structure analysis by the maximum-entropy method. *Acta Crystallographica Section A*, 46(4), 263-270.
- [97] Sakata, M., Uno, T., Takata, M., & Howard, C. J. (1993). Maximum-entropy-method analysis of neutron diffraction data. *Journal of applied crystallography*, 26(2), 159-165.
- [98] Iversen, B. B., Nielsen, S. K., & Larsen, F. K. (1995). Reciprocal-and direct-space determination of the temperature dependence of thermal vibrations in magnesium: A neutron diffraction study. *Philosophical Magazine A*, 72(5), 1357-1380.
- [99] Takata, M., Umeda, B., Nishibori, E., Sakata, M., Saito, Y., Ohno, M., & Shinohara, H. (1995). Confirmation by X-ray diffraction of the endohedral

nature of the metallofullerene Y@ C82. *Nature*, 377(6544), 46.

- [100] De Vries, R. Y., Briels, W. J., & Feil, D. (1996). Critical analysis of non-nuclear electron-density maxima and the maximum entropy method. *Physical review letters*, 77(9), 1719.
- [101] Palatinus, L., & Smaalen, S. V. (2002). The generalized F constraint in the maximum-entropy method—a study on simulated data. *Acta Crystallographica Section A: Foundations of Crystallography*, 58(6), 559-567.
- [102] Jaynes, E. T. (1957). Information theory and statistical mechanics. *Physical review*, 106(4), 620.
- [103] Ishikawa, Y., Zhang, J., Kiyonagi, R., Yonemura, M., Matsukawa, T., Hoshikawa, A., ... & Kamiyama, T. (2018). Z-MEM, Maximum Entropy Method software for electron/nuclear density distribution in Z-Code. *Physica B: Condensed Matter*.
- [104] Palatinus, L. (2003). *Maximum Entropy Method in Superspace Crystallography* (Doctoral dissertation). Retrieved from <https://epub.uni-bayreuth.de/id/eprint/961>
- [107] Chaikin, P. M. (1990). An Introduction to Thermopower for those who might want to use it to study Organic Conductors and Superconductors. In *Organic Superconductivity* (pp. 101-115). Springer, Boston, MA.
- [108] Kittel, C. *Introduction to Solid State Physics*. 8th ed2005: Wiley.
- [109] Tritt, T. M. (2011). Thermoelectric phenomena, materials, and applications. *Annual review of materials research*, 41, 433-448.
- [110] Kim, H. S., Gibbs, Z. M., Tang, Y., Wang, H., & Snyder, G. J. (2015). Characterization of Lorenz number with Seebeck coefficient measurement. *APL materials*, 3(4), 041506.
- [111] Klemens, P. G. (1969). Theory of the thermal conductivity of solids. *Thermal conductivity*. New York: Academic Press.
- [112] Newton, T. R., Melkote, S. N., Watkins, T. R., Trejo, R. M., & Reister, L. (2009). Investigation of the effect of process parameters on the formation and characteristics of recast layer in wire-EDM of Inconel 718. *Materials Science and Engineering: A*, 513, 208-215.
- [113] Quantum Design. (2002). *Physical Property Measurement System: Thermal Transport Option User's Manual*. Retrieved from

[https://www.mrl.ucsb.edu/sites/default/files/mrl\\_docs/instruments/PPMSTTO\\_manualB0.pdf](https://www.mrl.ucsb.edu/sites/default/files/mrl_docs/instruments/PPMSTTO_manualB0.pdf)

- [114] Singh, Y. (2013). Electrical resistivity measurements: a review. In *International journal of modern physics: Conference series* (Vol. 22, pp. 745-756). World Scientific Publishing Company.
- [115] Mettler-Toledo AG, Laboratory & Weighing Technologies. (2002). *Operating Instruction Density Kit*. Retrieved from [https://www.mt.com/dam/mt\\_ext\\_files/Editorial/Generic/4/XS\\_density-kit\\_0x000010083f72cdbe400075b3\\_files/xp-xs-density-analy-ba-11780508b.pdf](https://www.mt.com/dam/mt_ext_files/Editorial/Generic/4/XS_density-kit_0x000010083f72cdbe400075b3_files/xp-xs-density-analy-ba-11780508b.pdf)
- [116] Density Determination Kit of Mettler Toledo Balance [Digital image]. (2018). Retrieved from <https://assets.fishersci.com/TFS-Assets/CCG/product-images/F181762~p.eps-650.jpg>
- [117] Borup, K. A., De Boor, J., Wang, H., Drymiotis, F., Gascoin, F., Shi, X., ... & Snyder, G. J. (2015). Measuring thermoelectric transport properties of materials. *Energy & Environmental Science*, 8(2), 423-435.
- [118] Zhao, D., Qian, X., Gu, X., Jajja, S. A., & Yang, R. (2016). Measurement techniques for thermal conductivity and interfacial thermal conductance of bulk and thin film materials. *Journal of Electronic Packaging*, 138(4), 040802.
- [119] Parker, W. J., Jenkins, R. J., Butler, C. P., & Abbott, G. L. (1961). Flash method of determining thermal diffusivity, heat capacity, and thermal conductivity. *Journal of applied physics*, 32(9), 1679-1684.

# Acknowledgement

I would like to thank my supervisor Prof. Takashi Kamiyama and also Dr. Horoyuki Takeya for their patient guidance, great support, encouragement and kind advice throughout my PhD research studies.

I would like to thank my parents for their encouragements and support.

I would also like to thank Dr. Yoshihisa Ishikawa, Dr. Shuki Torii, Dr. Sanghyun Lee, and Dr. Masato Hagihara for their patient guidance and great support. I am indebted to them for their help.

I also thank Dr. Yoshiki Takagiwa, Dr. Shintaro Adachi, Namba Kaoru and Masahiro Shioya for their valuable assistance during my experiments. I thank all my colleagues, Tan Zhijian, Nur Ika Puji Ayu, Wu Peng, and Seungyub Song for providing me help during my experiment in BL08.

I would like to express my gratitude to Japan Ministry of Education, Culture, Sports, Science and Technology (MEXT) for the scholarship which supports my stay in Japan. Also, I thank SOKENDAI and S-type project BL08 for supporting my experiment.

I would like to thank my best friends: Leni Azyus Fitri, Emy Mulyani, Mutiara Wide, and Ira Susanti for their encouragement.

Widya Rika Puspita